Facoltà di Scienze e Tecnologie

Dipartimento di Chimica

UNIVERSITÀ DEGLI STUDI DI MILANO

PhD in Chemistry XXXI cycle

New Semiclassical Theories for Vibrational Spectroscopy

Supervisor: Prof. Michele CEOTTO
Accepted on the recommendation of: Prof. Nandini Ananth and Prof. David Coker

Candidate:

Giovanni Di Liberto

Matr. n. R11225

Academic year 2018-2019

Abstract

The main goal of this doctoral work was to develop theoretical advances of the semiclassical theory applied to molecular spectroscopy. In particular, the attention was centered at the coherent states based Time Averaging Semiclassical Initial Value Representation (TA-SCIVR) approximation to the vibrational spectral density. This approach is a solid way to access accurate vibrational spectra of molecular systems at a quantum approximate level. Nevertheless, it is affected by some criticalities as numerical issues and the so-called curse of dimensionality problem. Both represent an important stumbling block for the exploitation of the methodology towards molecules of increasing dimensions and complexity, preventing its application to general problems in the vibrational spectroscopy field. In my doctoral work we tried to face both issues, taming the numerical issues of the spectral density by introducing analytic and numerical approximations, and later developing with the group the Divide and Conquer Semiclassical dynamics (DC-SCIVR), a method which exploits the standard semiclassical formalism, but it works in reduced dimensional subspaces, with the aim of overcoming the curse of dimensionality. The advances first have been tested on simple molecules and then they have been employed to study spectroscopic relevant molecules. Main results show that it is possible to recover vibrational spectra even of those molecules affected by significant numerical issues, as well as high-dimensional ones, retaining the same accuracy of TA-SCIVR. In this thesis I first present some basics of the Semiclassical theory, with focus on vibrational spectroscopy, and then are shown the advances proposed, with applications on some relevant molecular systems in vibrational spectroscopy as supramolecular systems made by clusters of water and protonated glycine dimer, or high-dimensional molecules as benzene and C_{60}.

To all those who have supported and believed in me

List of publications

Publications directly related to this work

Results shown in this document are reported in details in:

- "Protonated Glycine Supramolecular Systems: the need for quantum dynamics" F. Gabas, G. Di Liberto, R. Conte, M. Ceotto, *Chem. Sci.* 9, 7894 (2018).
- "Divide-and-conquer semiclassical molecular dynamics: An application to water clusters" G. Di Liberto, R. Conte, M. Ceotto, *J. Chem. Phys.* **148**, 104302 (2018).
- "Divide and conquer semiclassical molecular dynamics: A practical method for spectroscopic calculations of high dimensional molecular systems" G. Di Liberto, R. Conte, M. Ceotto, *J. Chem. Phys.* **148** , 014307 (2018).
- "Semiclassical Divide-and-Conquer Method for Spectroscopic Calculations of High Dimensional Molecular Systems" M. Ceotto, G. Di Liberto, and R. Conte *Phys. Rev. Lett.* **119**, 010401 (2017).
- "The importance of the pre-exponential factor in semiclassical molecular dynamics" G. Di Liberto and M. Ceotto, *J. Chem. Phys.* **145**, 144107 (2016).

Other Publications submitted during the doctorate

- "A quantum mechanical insight into SN2 reactions: Semiclassical initial value representation calculations of vibrational features of the Cl−· · · CH3Cl pre-reaction complex with the VENUS suite of codes" X. Ma, G. Di Liberto, R. Conte, W.L. Hase, and M. Ceotto *J. Chem. Phys.* **149**, 164113 (2018).
- "Atomistic Explanation for Interlayer Charge Transfer in Metal–Semiconductor Nanocomposites: The Case of Silver and Anatase" G. Di Liberto, V. Pifferi, L. Lo Presti, M. Ceotto, and L. Falciola, *J. Phys. Chem. Lett.* **8**, 5372 (2017).

- "A close look at the structure of the TiO2-APTES interface in hybrid nanomaterials and its degradation pathway: an experimental and theoretical study" D. Meroni, L. Lo Presti, G. Di Liberto, M. Ceotto, R. G. Acres, K. L. Prince, R. Bellani, G. Soliveri and Silvia Ardizzone, *J. Phys. Chem. C* **121**, 430 (2016).

Other Publications submitted before the doctorate

- "Impregnation versus bulk synthesis: How the synthetic route affects the photocatalytic efficiency of Nb/Ta: N codoped TiO2 nanomaterials" L. Rimoldi, C. Ambrosi, G. Di Liberto, L. Lo Presti, M. Ceotto, C. Oliva, D. Meroni, S. Cappelli, G. Cappelletti, G. Soliveri, and S. Ardizzone *J. Phys. Chem. C* **119**, 24104 (2015).
- "Unraveling the cooperative mechanism of visible-light absorption in bulk N, Nb codoped TiO2 powders of nanomaterials" C. Marchiori, G. Di Liberto, G. Soliveri, L. Loconte, L. Lo Presti, D. Meroni, M. Ceotto, C. Oliva, S. Cappelli, G. Cappelletti, C. Aieta, and S. Ardizzone, *J. Phys. Chem. C* **118**, 24152 (2014).

Contents

Chapter 1

Molecular Dynamics, from the beginning to nowadays

The deep understanding at the atomistic level of processes involving molecular systems has gained increasing attention in the last decades, with the aim of providing a better physical interpretation, reliable predictions and to complement and explain experimental results. With the help of calculators, the numerical integration of atoms' equations of motion become possible, leading to the era of molecular dynamics. The dimensions of systems under examination increased with the years, going parallel with the improvement in the computational power, that nowadays allows to simulate even systems with thousands of atoms.

Pioneering simulations in this sense were reported by Rahman in 1964 and Vherle in 1967 by simulating liquid Argon (864 atoms in a cubic box), moving under a Lennard-Jones potential.[1, 2]

Molecular dynamics today is largely widespread and it is used to simulate nanomaterials,[3, 4, 5] big proteins,[6, 7] DNA sequences,[8, 9] and to design drugs by optimizing the interaction with target sites. Generally, in the simulation of such high dimensional systems the atoms are moved by solving classical Newton's equations, *i.e.* atoms are treated as classical objects.

Despite the potentiality of this approach in terms of applications to several cases of study, spreading from a bunch of degrees freedom to thousands, classical mechanics misses several aspects that in principle can be not negligible, arising from quantum effects. It is noteworthy that this shortcoming is not a weakness of classical simulations but it is just an intrinsic limitation of the theory; simply because it is not written to account for them. In atomistic simulations of nuclei, quantum effects can become relevant[10] and classical mechanics can provide insights and a sound of physics interpretation, but not a complete one. Thus, a different formalism is necessary to provide an undisputed interpretation, that in the limit of negligible quantum effects has to resemble classical mechanics results.

Nuclear quantum effects can be accounted by only exploiting a proper quantum formalism, that instead of solving Newton equations of motions, relies on solving the Schrödinger equation. Now, in this framework the Hamiltonian of the system is fully quantum mechanical, and can be resolved by means of different methods, such as grids, and perturbative approaches to name a few.[11, 12, 13, 14] Within quantum mechanical formalism every kind of quantum effect is in principle accounted. However, very often a stumbling block is again around the corner. In this case, there are no limitations in the theory (excluding relativistic effects), but practical ones, due the computational demand. A quantum mechanical simulation usually implies costs several order of magnitude higher than a classical one, that often exponentially increase with the system's dimensionality, leading to the exponential scaling problem also called curse of dimensionality. Because of it, exact quantum dynamics simulations are nowadays limited

to few bunches of degrees of freedom.[14]

The exponential scaling problem poses the need of alternative strategies able from one side to grasp quantum mechanical effects in molecular dynamics, and from the other one to overcome, or at least reduce, the high computational demand. A possible solution to such limitations comes from Feynman's path integral formulation of quantum

mechanics,[15] which is the basis of several methods. One of them is Semiclassical theory (SCIVR) developed by Miller and Heller.[16, 17, 18, 19] In this PhD thesis, the focus was placed on Semiclassical theory, while more details about other methods and their outstanding results can be found in the Literature.[20, 21, 22, 23, 24]

Semiclassical dynamics attempts to reproduce qualitatively and quantitatively quantum effects with the cost of (many) classical simulations. Differently from pure quantum simulations it only requires the evolution of classical trajectories which are less demanding to be computed than quantum wavepackets. It relies on Feynman's path integral formulation of quantum mechanics,[15] where the quantum propagator is approximated by a collection of classical paths, and quantum effects come from the fluctuations around them as well as their overlap.[25]

Several scientists devoted their research toward the progress of semiclassical theory, making it nowadays a practical route to study molecular systems.[26, 27, 28, 29, 30, 31, 32, 33, 34, 35, 36, 37, 38, 39, 40, 41, 42, 43, 44, 45] Today it is widespread, and many works are published every year in different fields of chemistry, and physics, making semiclassical dynamics one the most promising methods to provide a clear, undisputed and insightful physical interpretations of atomistic processes.

In this PhD thesis semiclassical theory is exploited for spectroscopic calculations of tailored models and real molecular systems. In particular, two criticalities of the semiclassical approximation to the quantum propagator are faced, with the aim of making semiclassical calculations doable for systems of high dimensionality and complexity.

Chapter 2

Introduction to Path Integral

Within the standard formulation of quantum mechanics the state of a system under the Hamiltonian $\hat{H}$ is fully described by the solution $|\psi\rangle$ of the Schrodinger equation

$$i\hbar\frac{\partial|\psi\rangle}{\partial t} = \hat{H}|\psi\rangle\,. \tag{2.0.1}$$

If we express the state in the coordinate representation, we can it write as

$$\psi(\mathbf{q},t) = \left\langle \mathbf{q}\middle| e^{-\frac{i}{\hbar}\widehat{H}t}\middle|\,\psi(\mathbf{q},0)\right\rangle, \tag{2.0.2}$$

where $\psi(\mathbf{q},0)$ is given by the initial conditions of Eq. (2.0.1). By adding an identity relation $I = \int d\mathbf{q}'\left|\mathbf{q}'\right\rangle\left\langle\mathbf{q}'\right|$ the previous equation can be written in the new basis $|\mathbf{q}'\rangle$ as

$$\psi(\mathbf{q},t) = \int \left\langle \mathbf{q}\middle| e^{-\frac{i}{\hbar}\widehat{H}t}\middle|\,\mathbf{q}'\right\rangle \psi(\mathbf{q}',0)\,d\mathbf{q}' \tag{2.0.3}$$

The matrix elements $\left\langle \mathbf{q}\middle| e^{-\frac{i}{\hbar}\widehat{H}t}\middle|\,\mathbf{q}'\right\rangle$ describe the probability for going from $|\mathbf{q}'\rangle$ to $|\mathbf{q}\rangle$ at time t and their knowledge coincides to solving Eq. (2.0.1).

The basic idea of Feynman path integral formulation is to find an exact expression of the quantum propagator $\left\langle \boldsymbol{q}\middle| e^{-\frac{i}{\hbar}\widehat{H}t}\middle|\,\mathbf{q}'\right\rangle$ in terms of "paths" which link $\mathbf{q}'$ with $\mathbf{q}$. To start off we look at the shape assumed by the propagator in the case of a free particle, *i.e.* an

Hamiltonian under a constant potential V_0. In this particular case, the Hamiltonian has only a kinetic contribution

$$\hat{H} = \frac{\hat{p}^2}{2m} + V_0. \tag{2.0.4}$$

By substituting the Hamiltonian expression into the quantum propagator, we obtain

$$\left\langle \mathbf{q} \middle| e^{-\frac{i}{\hbar}\widehat{H}t} \middle| \mathbf{q}' \right\rangle = \left\langle \mathbf{q} \middle| e^{-\frac{i}{\hbar}\frac{\hat{p}^2}{2m}t} \middle| \mathbf{q}' \right\rangle e^{-\frac{i}{\hbar}V_0 t}, \tag{2.0.5}$$

where the potential contribution can be moved out the overlap since it is a constant. The quantity inside the brackets can be solved the momenta basis $I = \int d\mathbf{p} \left|\mathbf{p}\right\rangle \left\langle \mathbf{p}\right|$, in this way we can write the previous equation in a more suitable way

$$\int\int d\mathbf{p} d\mathbf{p}' \left\langle \mathbf{q} \middle| \mathbf{p} \right\rangle \left\langle \mathbf{p} \middle| e^{-\frac{i}{\hbar}\frac{\hat{p}^2}{2m}t} \middle| \mathbf{p}' \right\rangle \left\langle \mathbf{p}' \middle| \mathbf{q}' \right\rangle, \tag{2.0.6}$$

$\left\langle \mathbf{q} \middle| \mathbf{p} \right\rangle = \frac{1}{\sqrt{(2\pi\hbar)^F}} e^{\frac{i}{\hbar}\mathbf{pq}}$, $\left\langle \mathbf{p}' \middle| \mathbf{q}' \right\rangle = \frac{1}{\sqrt{(2\pi\hbar)^F}} e^{-\frac{i}{\hbar}\mathbf{p}'\mathbf{q}'}$, and $\left\langle \mathbf{p} \middle| e^{-\frac{i}{\hbar}\frac{\hat{p}^2}{2m}t} \middle| \mathbf{p}' \right\rangle = \left\langle \mathbf{p} \middle| \mathbf{p}' \right\rangle e^{-\frac{i}{\hbar}\frac{\mathbf{p}'^2}{2m}t}$.
As an overall result, the quantum propagator for the free particle will be

$$\left\langle \mathbf{q} \middle| e^{-\frac{i}{\hbar}\frac{\hat{p}^2}{2m}t} \middle| \mathbf{q}' \right\rangle e^{-\frac{i}{\hbar}V_0 t} = e^{-\frac{i}{\hbar}V_0 t} \int\int d\mathbf{p} d\mathbf{p}' \frac{1}{\sqrt{(2\pi\hbar)^F}} e^{\frac{i}{\hbar}\mathbf{pq}} \left\langle \mathbf{p} \middle| \mathbf{p}' \right\rangle e^{-\frac{i}{\hbar}\frac{\mathbf{p}'^2}{2m}t} \frac{1}{\sqrt{(2\pi\hbar)^F}} e^{-\frac{i}{\hbar}\mathbf{p}'\mathbf{q}'}$$

$$= \frac{1}{(2\pi\hbar)^F} e^{-\frac{i}{\hbar}V_0 t} \int d\mathbf{p} e^{-\frac{i}{\hbar}\left[\frac{\mathbf{p}^2}{2m} - \mathbf{p}(\mathbf{q}-\mathbf{q}')\right]}. \tag{2.0.7}$$

Now the integral is reduced to be a simple Gaussian integral leading to

$$\left\langle \mathbf{q} \middle| e^{-\frac{i}{\hbar}\frac{\hat{p}^2}{2m}t} \middle| \mathbf{q}' \right\rangle e^{-\frac{i}{\hbar}V_0 t} = \sqrt{\left(\frac{m}{2\pi i\hbar t}\right)^F} e^{\frac{i}{\hbar}\left[\frac{m}{2t}(\mathbf{q}-\mathbf{q}')^2 - V_0 t\right]}. \tag{2.0.8}$$

Eq. (2.0.8) is the expression of the quantum propagator for the free-particle system. Unfortunately, Eq. (2.0.8) can not be generalized to a general potential V; nevertheless can be used as a starting point.

For a generic Hamiltonian with a non-constant potential, the whole quantum propaga-

tor can be subdivided into N time slices

$$e^{-\frac{i}{\hbar}\widehat{H}t} = e^{-\frac{i}{\hbar}\widehat{H}\Delta t}e^{-\frac{i}{\hbar}\widehat{H}\Delta t}...e^{-\frac{i}{\hbar}\widehat{H}\Delta t}e^{-\frac{i}{\hbar}\widehat{H}\Delta t}, \tag{2.0.9}$$

where $\Delta t = \frac{t}{N}$. If now we call $\mathbf{q}_0 = \mathbf{q}'$ and $\mathbf{q}_N = \mathbf{q}$ one can write the quantum propagator as

$$\left\langle \mathbf{q}_N \middle| e^{-\frac{i}{\hbar}\widehat{H}t} \middle| \mathbf{q}_0 \right\rangle = \int d\mathbf{q}_1 d\mathbf{q}_2 ... d\mathbf{q}_N$$

$$\left\langle \mathbf{q}_N \middle| e^{-\frac{i}{\hbar}\widehat{H}\Delta t} \middle| \mathbf{q}_{N-1} \right\rangle \left\langle \mathbf{q}_{N-1} \middle| e^{-\frac{i}{\hbar}\widehat{H}\Delta t} \middle| \mathbf{q}_{N-2} \right\rangle ... \left\langle \mathbf{q}_1 \middle| e^{-\frac{i}{\hbar}\widehat{H}\Delta t} \middle| \mathbf{q}_0 \right\rangle, \tag{2.0.10}$$

where we have added N identity relations. For each time slice $\left\langle \mathbf{q}_i \middle| e^{-\frac{i}{\hbar}\widehat{H}\Delta t} \middle| \mathbf{q}_{i-1} \right\rangle$ by expliciting the Hamiltonian we have $\left\langle \mathbf{q}_N \middle| e^{-\frac{i}{\hbar}\left(\frac{p^2}{2m}+V\right)\Delta t} \middle| \mathbf{q}_{N-1} \right\rangle$. Now in the limit of a infinitesimal time slice, one can reasonably assume that

$$\left\langle \mathbf{q}_N \middle| e^{-\frac{i}{\hbar}\left(\frac{\hat{p}^2}{2m}+\hat{V}\right)\Delta t} \middle| \mathbf{q}_{N-1} \right\rangle = \sqrt{\left(\frac{m}{2\pi i\hbar\Delta t}\right)^F} e^{\frac{i}{\hbar}\left[\frac{m}{2\Delta t}(\mathbf{q}-\mathbf{q}')^2 - \left(\frac{V(\mathbf{q}_N)+V(\mathbf{q}_{N-1})}{2}\right)\Delta t\right]}, \tag{2.0.11}$$

because the potential will be slowly variant. By expliciting every slice, the expression of the quantum propagator will be

$$\left\langle \mathbf{q}_N \middle| e^{-\frac{i}{\hbar}\widehat{H}t} \middle| \mathbf{q}_0 \right\rangle = \left(\sqrt{\frac{m}{2\pi i\hbar\Delta t}}\right)^{3N}$$

$$\int e^{\frac{i}{\hbar}\left[\frac{m}{2\Delta t}\sum_{i=1}^{N}(\mathbf{q}_i-\mathbf{q}_{i-1})^2\right]} e^{-\frac{i}{\hbar}\Delta t\left[\frac{1}{2}(V(\mathbf{q}_N)+V(\mathbf{q}_0))+\sum_{i=1}^{N}V(\mathbf{q}_i)\right]} \prod_{i=1}^{N} d\mathbf{q}_i. \tag{2.0.12}$$

This apparently very complicate expression, in the limit of $N \to \infty$ or $\Delta t \to dt$ becomes easier because

$$e^{\frac{i}{\hbar}\left[\frac{m}{2\Delta t}\sum_{i=1}^{N}(\mathbf{q}_i-\mathbf{q}_{i-1})^2\right]} = e^{\frac{i}{\hbar}\left[\frac{m}{2}\int\left(\frac{d\mathbf{q}}{dt}\right)^2 dt\right]} \tag{2.0.13}$$

and

$$e^{-\frac{i}{\hbar}\left[\int dt V(\mathbf{q})\right]} = e^{-\frac{i}{\hbar}\Delta t\left[\frac{1}{2}(V(\mathbf{q}_N)+V(\mathbf{q}_0))+\sum_{i=1}^{N}V(\mathbf{q}_i)\right]}, \tag{2.0.14}$$

thus

$$\left\langle \mathbf{q}_N \middle| e^{-\frac{i}{\hbar}\widehat{H}t} \middle| \mathbf{q}_0 \right\rangle = \sqrt{\left(\frac{m}{2\pi i\hbar t}\right)^F} \int \wp\left[\mathbf{q}_t\right] e^{\frac{i}{\hbar}S_t(\mathbf{q}_N,\mathbf{q}_0)}. \tag{2.0.15}$$

Eq. (2.0.15) can be interpreted as a summation over all possible paths connecting the initial point $\mathbf{q}_0$ and the final one $\mathbf{q}_t = \mathbf{q}_N$, where each path is weighted by an oscillating term depending by its action. Although Eq. (2.0.15) is exact in principle, it is very tough to be put into practice because of the huge amount of required paths to be taken into account to numerically converge the equation, since the weighting function is usually strongly oscillating.

Chapter 3

Semiclassical approximation to the quantum propagator

The semiclassical approximation to the quantum propagator can be obtained by expanding the action along classical paths in Eq. (2.0.15). In such a way, the first terms different from the zero-th order ones are the second order variations of the action, since the first order is equal to zero because of the Hamilton's principle.

$$\left\langle \mathbf{q}_t \left| e^{-\frac{i}{\hbar}\widehat{H}t} \right| \mathbf{q}_0 \right\rangle \sim \sqrt{\left(\frac{m}{2\pi i\hbar t}\right)^F} \int \wp\left[\boldsymbol{q}_t\right] e^{\frac{i}{\hbar}\left[S_t^{Cl}(\boldsymbol{q}_t,\mathbf{q}_0)+\frac{1}{2}\frac{\delta^2 S_t^{Cl}(\mathbf{q}_t,\mathbf{q}_0)}{\delta \mathbf{q}_t^2}\delta\mathbf{q}_t^2\right]} \tag{3.0.1}$$

The second order fluctuations of the action can be written in terms of the eigenvalues (λ_n) of the Jacobi force field operator.[25] Now, by the following change of variables, $\prod_n dq_n = \prod_n a_n \left(\frac{\lambda_n^0}{2\pi i\hbar}\right)^{\frac{1}{2}}$ Eq. (3.0.1) can be analytically integrated, since now the integrand assumes a Gaussian shape.

$$\left\langle \mathbf{q}_t \left| e^{-\frac{i}{\hbar}\widehat{H}t} \right| \mathbf{q}_0 \right\rangle \sim \sqrt{\frac{m}{2\pi i\hbar t}} \sum_{Cl\,paths} \int \prod_n da_n e^{\frac{i}{\hbar}\left[S_t^{Cl}(\mathbf{q}_t,\mathbf{q}_0)+\frac{1}{2}\sum_n \lambda_n \left|a_n\right|^2\right]} \left(\frac{\lambda_n^0}{2\pi i\hbar}\right)^{\frac{F}{2}} \tag{3.0.2}$$

We observe that the zero-th order contribution can be moved out the integral, and inside the integral only the second order terms are remaining. The previous equation becomes

$$\left\langle \mathbf{q}_t \left| e^{-\frac{i}{\hbar}\widehat{H}t} \right| \mathbf{q}_0 \right\rangle \sim \sqrt{\frac{1}{2\pi i\hbar}} \sum_{Cl\,paths} e^{\frac{i}{\hbar}S^{Cl}(\mathbf{q}_t,\mathbf{q}_0)} \left\{ det\left(\mathbf{M}\right)\right\}^{\frac{1}{2}}. \tag{3.0.3}$$

In this version of the propagator, called Van Vleck propagator,[46] the zero-th order terms contribute with oscillations depending on the action of each path, that in the semiclassical approximation is a classical one. The second order terms which describe the quantum fluctuations around the classical paths are accounted into a pre-exponential factor $C_t\left(\mathbf{q}_t,\mathbf{q}_0\right) = \left\{ det\left(\mathbf{M}\right)\right\}^{\frac{1}{2}}$. The pre-exponential factor depends on the determinant of the monodromy matrix, which means a dependency from the second derivative of the action since $\mathbf{M} = -\frac{\partial^2 S}{\partial \mathbf{q}_t \partial \mathbf{q}_0}$. In the previous section we have showed that the second order fluctuations of the action can undergo a change of sign, and such change has a peculiar physical meaning, *i.e.* the trajectory finds a caustic point. Passing from it, the determinant of the monodromy matrix has to change sign, and to highlight this feature, we can write the pre-exponential factor as

$$C_t\left(\mathbf{q}_t,\mathbf{q}_0\right) = \left\{ det\left(-\frac{\partial^2 S}{\partial \mathbf{q}_t \partial \mathbf{q}_0}\right)\right\}^{\frac{1}{2}} = \left| det\left(-\frac{\partial^2 S}{\partial \mathbf{q}_t \partial \mathbf{q}_0}\right)\right|^{\frac{1}{2}} e^{-\frac{1}{2}\pi\nu}, \tag{3.0.4}$$

where we have separated the contribution of the modulos of the pre-exponential from a function $e^{-\frac{1}{2}\pi\nu}$ that accounts from the sign, since the index ν, called Morse or Maslov index, assumes only integer values leading to $e^{-\frac{1}{2}\pi\nu} = \pm 1$. Now, we can better understand what happens to the pre-exponential factor, because from one side the Morse index accounts for the change of sign, while on the other, the modulus goes to infinity. When a classical trajectory has a very chaotic behavior, a caustic point is very easily to happen, and consequently the trajectory becomes "unstable" or very hard to be numerically managed. A further drawback of the Van Vleck propagator lies into the so-called "root search problem" which means that, since it depends from initial and final coordinates $(\mathbf{q}_0, \mathbf{q}_t)$,

one has to evolve trajectories from initial conditions $\mathbf{q}_0$, and after has to look only for those ending at time t at the final coordinates $\mathbf{q}_t$. This latter problem was overcome by the development of Miller's Initial Value Representation of the semiclassical propagator, while the first issue was deeply investigated in the past by Semiclassical pioneeres, a small contribution within this topic is also presented below in the text.

3.1 Initial Value Representation of the quantum propagator

In the past years W.H. Miller pioneered the Initial Value Representation (SCIVR) of the quantum propagator,[47, 48] and it allowed later to make semiclassical able to deal with molecular systems. In SCIVR, the root search problem is substituted by a cheaper and computationally easier integral over the initial conditions. In particular, starting from the Van Vleck propagator

$$\left\langle \psi_2 \middle| e^{-\frac{i}{\hbar}\widehat{H}t} \middle| \psi_1 \right\rangle \sim \int\int d\mathbf{q}_0 d\mathbf{q}_t \left\langle \psi_2 \middle| \mathbf{q}_t \right\rangle \left\langle \mathbf{q}_t \middle| e^{-\frac{i}{\hbar}\widehat{H}t} \middle| \mathbf{q}_0 \right\rangle \left\langle \mathbf{q}_0 \middle| \psi_1 \right\rangle. \tag{3.1.1}$$

the pre-exponential factor $C_t\left(\mathbf{q}_t, \mathbf{q}_0\right) = \left\{ det\left(-\frac{\partial^2 S}{\partial \mathbf{q}_t \partial \mathbf{q}_0}\right)\right\}^{\frac{1}{2}}$ of the Van Vleck can be written as $C_t\left(\mathbf{q}_t, \mathbf{q}_0\right) = \left\{ det\left(\frac{\partial \mathbf{q}_t}{\partial \mathbf{p}_0}\right)\right\}^{-\frac{1}{2}}$. Now, if one wants to depend only from initial conditions has to move from $(\mathbf{q}_0, \mathbf{q}_t)$ to $(\mathbf{q}_0, \mathbf{p}_0)$. To do that, the integral over the final coordinates $\mathbf{q}_t$ has to be replaced by an integral over $\mathbf{p}_0$.

$$\sum_{Cl\, paths} \int d\mathbf{q}_t = \int d\mathbf{p}_0 \left| \frac{\partial \mathbf{q}_t\left(\mathbf{q}_0, \mathbf{p}_0\right)}{\partial \mathbf{p}_0} \right| \tag{3.1.2}$$

The initial value representation of the propagator in Eq. (3.1.1) will be

$$\left\langle \psi_2 \middle| e^{-\frac{i}{\hbar}\widehat{H}t} \middle| \psi_1 \right\rangle \sim \sqrt{\frac{1}{2\pi i\hbar}} \int\int d\mathbf{q}_0 d\mathbf{p}_0 \left\langle \psi_2 \middle| \mathbf{q}_t \right\rangle \left\langle \mathbf{q}_0 \middle| \psi_1 \right\rangle \left| \frac{\partial \mathbf{q}_t\left(\mathbf{q}_0, \mathbf{p}_0\right)}{\partial \mathbf{p}_0} \right|^{\frac{1}{2}} e^{\frac{i}{\hbar} S^{Cl}\left(\mathbf{q}_0, \mathbf{p}_0\right)} e^{-\frac{1}{2}\pi\nu}. \tag{3.1.3}$$

Finally, the initial value representation time evolution operator will be

$$e^{-\frac{i}{\hbar}\widehat{H}t}=\sqrt{\left(\frac{1}{2\pi i\hbar}\right)^{F}}\int\int d\mathbf{q}_0 d\mathbf{p}_0\left|\frac{\partial\mathbf{q}_t\left(\mathbf{q}_0,\mathbf{p}_0\right)}{\partial\mathbf{p}_t}\right|^{\frac{1}{2}}e^{\frac{i}{\hbar}S^{Cl}(\mathbf{q}_0,\mathbf{p}_0)}e^{-\frac{1}{2}\pi\nu}\left|\mathbf{q}_t\right\rangle\left\langle\mathbf{q}_0\right|. \tag{3.1.4}$$

In Eq. (3.1.4) the integral is performed along initial conditions, thus it can be numerically implemented by using Monte Carlo techniques in which, different initial conditions are sampled in the phase space.

3.2 Coherent state representation of the semiclassical propagator

Starting from the 80es, E.J. Heller pioneered an extremely flexible and efficient representation of the semiclassical wavefunction.[49, 32, 50] In the coordinate representation the wavefunction presents a bound contribution made by a Gaussian shape, and a free-particle one.

$$\left\langle\mathbf{q}\middle|\mathbf{p}_t\mathbf{q}_t\right\rangle=\left(\frac{det\left(\mathbf{\Gamma}\right)}{\pi}\right)^{\frac{1}{4}}e^{-\frac{1}{2}(\mathbf{q}-\mathbf{q}_t)\mathbf{\Gamma}(\mathbf{q}-\mathbf{q}_t)^T+\frac{i}{\hbar}\mathbf{p}_t(\mathbf{q}-\mathbf{q}_t)^T} \tag{3.2.1}$$

If the $\boldsymbol{\Gamma}$ matrix, is chosen to be constant in time, the wavefunction is now defined as a coherent state with the property that at each time t, the eigenvalues of the position and momentum operators are the classical position $\mathbf{q}_t$ and momentum $\mathbf{p}_t$, *i.e.* within this picture, the wavefunction follows the classical trajectory. In this new coherent state dressed representation the semiclassical propagator assumes the Heller-Herman-Kluk-Kay form,[51, 27, 28, 29, 52] where now the wavefunction is is written in terms of coherent states.

$$e^{-\frac{i}{\hbar}Ht}=\left(\frac{1}{2\pi\hbar}\right)^{F}\iint d\mathbf{p}_0 d\mathbf{q}_0 C_t\left(\mathbf{p}_0,\mathbf{q}_0\right)e^{\frac{i}{\hbar}S_t(\mathbf{p}_0,\mathbf{q}_0)}\left|\mathbf{p}_t,\mathbf{q}_t\right\rangle\left\langle\mathbf{p}_0,\mathbf{q}_0\right| \tag{3.2.2}$$

In this representation the pre-exponential factor is computed as

$$C_t\left(\mathbf{q}_0,\mathbf{p}_0\right)=\sqrt{\det\left[\frac{1}{2}\left(\mathbf{M}_{qq}+\frac{1}{\gamma}\mathbf{M}_{pp}\gamma+\frac{i}{\hbar\boldsymbol{\gamma}}\mathbf{M}_{pq}+\frac{\hbar}{i}\mathbf{M}_{qp}\boldsymbol{\gamma}\right)\right]} \tag{3.2.3}$$

where $\mathbf{M}_{qq}$, $\mathbf{M}_{qp}$, $\mathbf{M}_{pq}$, $\mathbf{M}_{pp}$ are the elements of the Monodromy (or stability) matrix.

$$\mathbf{M}=\begin{pmatrix}\mathbf{M}_{pp} & \mathbf{M}_{pq}\\ \mathbf{M}_{qp} & \mathbf{M}_{qq}\end{pmatrix}=\begin{pmatrix}\partial\mathbf{p}_t/\partial\mathbf{p}_0 & \partial\mathbf{p}_t/\partial\mathbf{q}_0\\ \partial\mathbf{q}_t/\partial\mathbf{p}_0 & \partial\mathbf{q}_t/\partial\mathbf{q}_0\end{pmatrix} \tag{3.2.4}$$

A general matrix element $\left\langle\psi_f\middle|e^{-\frac{i}{\hbar}\widehat{H}t}\middle|\psi_i\right\rangle$ is expressed as

$$\left\langle\psi_f\middle|e^{-\frac{i}{\hbar}\widehat{H}t}\middle|\psi_i\right\rangle=\left(\frac{1}{2\pi\hbar}\right)^F\iint d\mathbf{p}_0d\mathbf{q}_0C_t\left(\mathbf{p}_0,\mathbf{q}_0\right)e^{\frac{i}{\hbar}S_t(\mathbf{p}_0,\mathbf{q}_0)}\left\langle\psi_f\middle|\mathbf{p}_t,\mathbf{q}_t\right\rangle\left\langle\mathbf{p}_0,\mathbf{q}_0\middle|\psi_i\right\rangle, \tag{3.2.5}$$

where the initial and final wavefunctions are coherent states $\left|\psi_i\right\rangle=\left|\mathbf{p}_i\mathbf{q}_i\right\rangle$ and $\left|\psi_f\right\rangle=\left|\mathbf{p}_f\mathbf{q}_f\right\rangle$. The coherent state overlap of Eq. (3.2.5) can be computed by taking advantage of the coordinate representation of coherent states, *i.e.*

$$\left\langle\psi_f\middle|\mathbf{p}_t\mathbf{q}_t\right\rangle=\int d\mathbf{q}\left\langle\psi_f\middle|\mathbf{q}\right\rangle\left\langle\mathbf{q}\middle|\mathbf{p}_t\mathbf{q}_t\right\rangle \tag{3.2.6}$$

Now, by substituting Eq. (3.2.1) into the latter integral, the coherent state integral results into

$$\left\langle\psi_j\middle|\mathbf{p}_k,\mathbf{q}_k\right\rangle=$$

$$exp\left[-\frac{1}{4}\left(\mathbf{q}_j-\mathbf{q}_k\right)\boldsymbol{\Gamma}\left(\mathbf{q}_j-\mathbf{q}_k\right)^T-\frac{1}{4\hbar}\left(\mathbf{p}_j-\mathbf{p}_k\right)\frac{1}{\boldsymbol{\Gamma}}\left(\mathbf{p}_j-\mathbf{p}_k\right)^T+\frac{i}{2\hbar}\left(\mathbf{p}_j+\mathbf{p}_k\right)\left(\mathbf{q}_j-\mathbf{q}_k\right)\right]. \tag{3.2.7}$$

It was showed that the Herman-Kluk is an alternative formulation of Miller-Van Vleck propagator; it is associated to a change of basis, from the coordinate one to the coherent states one. In section (11.1) of Appendix we show a derivation that was originally proposed by Miller.[53] Other derivations can be found in the Literature.[54]

The most delicate part of Eq. (3.2.2) is the pre-exponential factor of Eq. (3.2.3) since, when a trajectory becomes more and more chaotic, the modulus of monodromy matrix elements increases till reaching the numerical precision of the computational machine making numerically divergent the pre-exponential factor and the propagator itself. In order to avoid this undesirable inconvenience several ways was proposed to avoid such failure in the calculation of the propagator. The first one, was proposed by Kay,[28] and consists into looking at the modulus of the pre-exponential factor, where D_t is a threshold parameter.

$$\left| C_t \left(\mathbf{q}_0, \mathbf{p}_0 \right) \right| \geq D_t \tag{3.2.8}$$

If the condition reported in Eq. (3.2.8) is satisfied, the chaotic behavior is considered excessive and the trajectory is rejected, avoiding the numerical blow up of the propagator. An alternative way to check the stability of a classical trajectory was proposed by Wang, Manolopoulos and Miller.[55] They proposed to look at the condition reported in Eq. (3.2.9), where ε is a threshold value.

$$\left| \left| det \left(M^T M \right) \right| - 1 \right| \geq \varepsilon \tag{3.2.9}$$

It was recently shown that both strategies are roughly equivalent in terms of rejected trajectories, and it can be a problem for highly chaotic potentials, *i.e.* with a rejection ratio higher than 90%.

Going back to Eq. (3.2.4), the monodromy matrix has a very important physical meaning, since it is strongly related to the Liouville theorem. In particular, the conservation of the classical phase-space volume

$$d\mathbf{p}_t d\mathbf{q}_t = d\mathbf{p}_0 d\mathbf{q}_0 det \left(\mathbf{M} \right) \tag{3.2.10}$$

is a direct consequence of the following property

$$det\left(\mathbf{M}\right) = 1 \ \forall t \tag{3.2.11}$$

Chapter 4

Semiclassical dynamics for molecular spectroscopy

4.1 Semiclassical formulation of vibrational spectral density

In the Born-Oppenheimer approximation nuclei move on Potential Energy Surfaces. Each value is the electronic energy at fixed nuclei configuration. For small molecules high level pre-fitted PES are available,[56, 57, 58, 59, 60] while for high-dimensional systems electronic energies are provided by ab-anitio methods. Moreover, very accurate models and methods have been developed in recent years to allow quantum evaluations of electronic energies for systems embedded by a sorrounding as a solvent or a matrix.[61, 62, 63]

Now, given a potential energy surface (PES) computed at a certain level, and given a reference state $\left|\chi\right\rangle$, the spectral density or equivalently the power spectrum, is given by the Fourier transform of the autocorrelation function[64, 65]

$$I\left(E\right) \equiv \frac{1}{2\pi\hbar}\int_{-\infty}^{+\infty}\left\langle\chi\left|e^{-i\hat{H}t/\hbar}\right|\chi\right\rangle e^{iEt/\hbar}dt. \tag{4.1.1}$$

The major contribution to the peaks' intensity will be centered around the energy shell of the reference state. For chemical systems, a good choice for the reference state is a coherent state with energy evaluated within the harmonic approximation.[66, 67, 68] In

this spirit, $\left|\chi\right\rangle$ can be defined as

$$\left|\chi\right\rangle = \left|\mathbf{q}_{eq}\mathbf{p}_{eq}\right\rangle \tag{4.1.2}$$

where $\mathbf{q}_{eq}$ is the coordinates vector at the equilibrium geometry, while $\mathbf{p}_{eq}$ is the momenta vector, *i.e.* $p_{i,eq} = \sqrt{\frac{\hbar}{m}\omega_i}$ where ω_i is the harmonic frequency of the i-th degree of freedom. By substituting the Heller-Herman-Kluk-Kay propagator of Eq. (3.2.2) into (4.1.1), we obtain the working formula for the semiclassical spectra density.

$$I\left(E\right) = \left(\frac{1}{2\pi\hbar}\right)^{F+1} \int_{-\infty}^{+\infty} e^{iEt/\hbar} dt \iint d\mathbf{p}_0 d\mathbf{q}_0 C_t\left(\mathbf{p}_0, \mathbf{q}_0\right) e^{\frac{i}{\hbar}S_t(\mathbf{p}_0,\mathbf{q}_0)} \left\langle \chi \middle| \mathbf{p}_t, \mathbf{q}_t \right\rangle \left\langle \mathbf{p}_0, \mathbf{q}_0 \middle| \chi \right\rangle \tag{4.1.3}$$

Eq. (4.1.3) is very slowly convergent with the number of classical trajectories, making it not suitable for chemical systems with more than few degrees of freedom. It is due to the high oscillating behavior of the integrand.[69, 70] To overcome this issue, different filtering procedures were proposed in the past years, in order to reduce the number of required trajectories to converge Eq. (4.1.3). The most relevant one are the Filinov filter proposed by Huang, Manolopoulos and Miller,[55] and the Time-Averaging filter proposed by Kaledin and Miller.[64, 65] In particular, the latter one has been showed to be very accurate for small-sized chemical systems requiring roughly a thousand of classical trajectories for each degree of freedom to converge.[68, 71, 72, 73, 65]

4.2 Time Averaging Filter

The basic idea of the time averaging filter is to rewrite Eq. (4.1.3) to have a less oscillating integrand, resulting into a much smaller number of trajectories required for converging the phase space integration of equation . The original derivation was provided by Kaledin and Miller,[64] where they also showed its potentiality by performing accurate vibrational spectra of several molecular systems up to nine degrees of freedom. The final

working formula of the spectral density is

$$I(E) = \left(\frac{1}{2\pi\hbar}\right)^F \iint d\mathbf{p}(0)\, d\mathbf{q}(0)\, \frac{1}{2\pi\hbar T} \left| \int_0^T e^{\frac{i}{\hbar}[S_t(\mathbf{p}(0),\mathbf{q}(0))+Et+\varphi_t]} \langle \chi | \mathbf{p}(t)\, \mathbf{q}(t) \rangle\, dt \right|^2 . \tag{4.2.1}$$

More details about the derivation can be found in Section (11.2). The Time Averaging filter is exact for harmonic oscillators, while for real potential energy profiles they suggested to employ the so-called separable-approximation, where the pre-exponetial factor is approximated to be $C_t(\mathbf{p}_0, \mathbf{q}_0) \sim e^{\frac{i}{\hbar}\varphi_t}$, where $\varphi_t = phase\left[C_t(\mathbf{p}_0, \mathbf{q}_0)\right]$.

Although an approximation is introduced, the time-averaging formulation leads to accurate vibrational spectra of small and medium sized molecular systems, with an accuracy of 20-30 wavenumbers with respect to exact levels.[74, 73, 72, 71]

4.3 The Multiple Coherent State approach

The Time Averaging filter has been proved to be a very powerful tool to reduce the number of required trajectories to converge the quantum propagator. However, still roughly a thousand of classical trajectories for each degree of freedom are necessary, thus preventing the exploitation of the formalism for ab-initio purposes, where few or even one classical trajectories are affordable. To overcome this issue, Ceotto proposed a tailored reference state, making a single trajectory enough for accurate spectra and allowing the exploitation of coherent state semiclassical calculations for ab-initio purposes.[75, 66, 67, 68, 76]

This "multiple coherent state" approach, as already mentioned, allows to recover accurate vibrational spectra from a handful or even one classical trajectory. The main idea is to run trajectories with selected initial conditions that lead to the highest contribution into Eq. (4.2.1). As an overall result, few trajectories are enough to recover accurate peaks. Such an approach put into practice the exploitation of semiclassical theory into on-the-fly (or direct) dynamics.[77]

To understand why few or even one classical trajectories are sufficient to reproduce most of spectral contribution, which should arise from thousand paths, we have to spend some words about the coherent state overlap reported in Eq (3.2.7).

In the semiclassical spectral density are present two different overlaps, one involving the reference state and the initial one, the second instead the wavepacket evolved at time t and the reference state. To explicit their form we can work in the coordinate representation, since coherent states presents the very familiar form reported in Eq. (3.2.1). The overlaps can be calculated taking advantage of the following equations

$$\left\langle \chi \middle| \mathbf{p}_t, \mathbf{q}_t \right\rangle = \int d\mathbf{x} \left\langle \chi \middle| \mathbf{x} \right\rangle \left\langle \mathbf{x} \middle| \mathbf{p}_t, \mathbf{q}_t \right\rangle = \int d\mathbf{x} \left\langle \mathbf{x} \middle| \chi \right\rangle^* \left\langle \mathbf{x} \middle| \mathbf{p}_t, \mathbf{q}_t \right\rangle$$

$$\left\langle \mathbf{p}_0, \mathbf{q}_0 \middle| \chi \right\rangle = \int d\mathbf{x} \left\langle \mathbf{p}_0, \mathbf{q}_0 \middle| \mathbf{x} \right\rangle \left\langle \mathbf{x} \middle| \chi \right\rangle = \int d\mathbf{x} \left\langle \mathbf{x} \middle| \mathbf{p}_0, \mathbf{q}_0 \right\rangle^* \left\langle \mathbf{x} \middle| \chi \right\rangle.$$

After some algebraic passages the coherent state overlap of Eq. (4.1.3) is

$$\left\langle \chi \middle| \mathbf{p}_t, \mathbf{q}_t \right\rangle \left\langle \mathbf{p}_0, \mathbf{q}_0 \middle| \chi \right\rangle =$$

$$e^{-\frac{\gamma}{4}(\mathbf{q}_t - \mathbf{q}_{eq})^2 - \frac{\gamma}{4}(\mathbf{q}_0 - \mathbf{q}_{eq})^2 - \frac{1}{4\gamma}(\mathbf{p}_t - \mathbf{p}_{eq})^2 - \frac{1}{4\gamma}(\mathbf{q}_0 - \mathbf{p}_{eq})^2}$$

$$\times\, e^{-i\left[\frac{1}{2}(\mathbf{p}_t\mathbf{q}_t - \mathbf{p}_0\mathbf{q}_0) + \frac{\mathbf{p}_{eq}}{2}(\mathbf{q}_t - \mathbf{q}_0) - \frac{\mathbf{q}_{eq}}{2}(\mathbf{p}_t - \mathbf{p}_0)\right]} \tag{4.3.1}$$

As we have reported in Eq. (4.1.2), in the SCVIR framework $|\chi\rangle$ is chosen according to an harmonic fashion. Now, if we consider a trajectory starting from $(\mathbf{p}_0, \mathbf{q}_0) = (\mathbf{p}_{eq}, \mathbf{q}_{eq})$, it will have an high superimposition with $|\chi\rangle$, resulting into an high contribution to the phase space integral enhancing the overlap statistics. Conversely, classical trajectories starting from energy shells far away from the reference state, will contribute less. We can know understand why instead of running thousand classical trajectories with randomly initial conditions, it is sufficient to select only few or even one of them. The classical trajectory starting from $(\mathbf{p}_{eq}, \mathbf{q}_{eq})$ is called "central trajectory" and is the classical version of the eigenstate associated to the harmonic Zero Point Energy of the system,

thus called eigentrajectory. The other classical trajectories resemble vibrationally excited eigenstates by increasing their initial kinetic energy. In this way a trajectory having $\mathbf{p}_0 = \left(\sqrt{\omega_1}, \sqrt{\omega_2}, ..., 3\sqrt{\omega_i}, ..., \sqrt{\omega_{N_{vib}}}\right)$ will strongly contribute to the spectroscopic excitation of $i-th$ degree of freedom. In summary, the spectral density of a system made by N_{vib} degrees of freedom can be accurately recovered by running $N_{vib}+1$ classical trajectories instead of approximately $10^3 \cdot N_{vib}$. This simplification is not costless, since the high energy excitations (high energetic overtones) could be off the mark, since the few considered classical trajectories are far in energy from them, while instead this issue is prevented in a fully converged calculation. However, in vibrational spectroscopy usually the most important signals concern fundamental and first overtone excitations. Despite the strong decrease in computational demand, the unambiguous assignment of the excitations present in a spectroscopic signal can be very hard, especially when the dimensionality of the system increases, and signals start to superimpose or to hamper each other. This consequence of the curse of dimensionality problem was overcome by Ceotto by extending the multiple coherent state approach, showing that a reference state of this form

$$\left|\chi\right\rangle = \prod_{i=1}^{N_{vib}} \left[\left|q_{eq}^i, p_{eq}^i\right\rangle + \varepsilon^i \left|q_{eq}^i, -p_{eq}^i\right\rangle\right] \tag{4.3.2}$$

allows in principle to select one by one all the possible excitations. It is evident that in this way a very crowded heap of signals can be resolved by assigning one by one. The excitations are selected modulating the value of $\boldsymbol{\varepsilon}$; for instance by choosing each value equal to 1, then Zero Point Energy can be recovered (ZPE), while setting $\varepsilon_j = -1$ the fundamental excitation of $j-th$ degree of freedom can be obtained, and so on.

MC-SCIVR was exploited for several applications in the past, allowing to recover accurate vibrational spectra of small molecular systems both in gas and condensed phase. Furthermore, it has been shown to be able to detect strong quantum effects like Zero Point Energy, quantum resonances, quantum anharmonicities, and deep tunneling splitting. However, it exploits huge troubles with chaotic trajectories, since the pre-exponential

can blow up. Furthermore, the method runs out of steam when the system's dimensionality overcomes 20-25 because of the curse of dimensionality. These were the topic of this PhD thesis and are discussed in details below in the text.

Chapter 5

The importance of the pre-exponential factor

As we have reported in the previous sections, the pre-exponential factor is the semi-classical quantity stricly connected with the quantum fluctuations. It comes clear that its correct evalutation is mandatory to account for quantum effects. As we have touched on above at the end of Section (3.2), the numerical calculation of Eq. (3.2.3) can undergo severe numerical issue when trajectories get chaotic. More in details, during the classical dynamics of a system it usually happens that the Monodromy matrix elements assume high values leading to high value of the modulos of the pre-exponential factor. It is not in principle a problem, but only a practical one when we calculate it numerically, and numbers get close to the numerical precision of the calculator. In this evenience, the estimates start to be affected by huge errors, and even the quantities overcome the numerical precision, leading to a numerical divergence. This issue prevents the recovery of spectroscopic signal from Eq. (4.2.1) and has to be avoided by rejecting the classical trajectory. The rejection of classical trajectories can be problematic when the computational demand is high or even when the rejection ratio (the number of rejected trajectories over the total number) is estremely high, because it becomes very hard to converge Eq. (4.2.1). Above in the text we have introduced two different rejection criteria, the first one developed by Kay, and second one by Wang, Manolopoulos and Miller. In the first case, we only look

if the pre-exponential factor becomes huge during the dynamics and if it overcomes a "safe" threshold value, the trajectory is rejected. In the second case instead, we look at the conservation of unity of $det\left(\mathbf{M}^T\mathbf{M}\right)$. Such described rejection criteria ensure the numerical stability of the pre-exponential factor and in general of the semiclassical integrand; however they do not prevent the rejection event, and if the ratio is extremely high a lot of computational time is required to converge the integral. Unfortunately "chaotic" systems, are not few, either in models or even in real molecules.

In the past years various pre-exponential factor numerical approximations were developed in order to fully avoid the rejection event or even to tame the chaotic behaviour of the trajectories, preventing their rejection. Many of them rely on the different, but equivalent to Eq. (3.2.3), Log-Derivative formulation of the pre-exponential factor.[78]

5.1 A "poor" person pre-exponential factor

A very simple but efficient for on-the-fly purposes pre-exponential factor approximation was proposed in 2011 motivated by the fact that (i) it should be exact for harmonic systems, (ii) it should not be sensitive to the choice of the coherent states width parameter $\boldsymbol{\Gamma}$, (iii) it should be local in the potential, (iv) it should retain the normalization of the pre-exponential factor, (v) and it should be computationally less demanding. All these points are addressed if the following "poor person" approximation of Eq. (4.1.3) is employed.[79]

$$I\left(E\right)=\left(\frac{1}{2\pi\hbar}\right)^{F+1}\int_{-\infty}^{+\infty}e^{iEt/\hbar}dtC_t\left(\mathbf{p}_{eq},\mathbf{q}_{eq}\right)\iint d\mathbf{p}_0d\mathbf{q}_0e^{\frac{i}{\hbar}S_t(\mathbf{p}_0,\mathbf{q}_0)}\left\langle\chi\middle|\mathbf{p}_t,\mathbf{q}_t\right\rangle\left\langle\mathbf{p}_0,\mathbf{q}_0\middle|\chi\right\rangle \tag{5.1.1}$$

In this approximation the pre-exponential factor is considered a function of time constant in the phase-space integral. $C_t\left(\mathbf{p}_{eq},\mathbf{q}_{eq}\right)$ is the pre-exponential factor of the central trajectory, *i.e.* the trajectory having as initial conditions the equilibrium configuration $\mathbf{q}_{eq}$, and momenta following an harmonic fashion $\mathbf{p}_{eq}$. This choice can be justified by assum-

ing that such a trajectory will be highly relevant in the semiclassical integrand. Within the poor-person approximation, rejection events are prevented since the pre-exponential factor is evaluated along only one trajectory, and it is used for all the remaining. It comes clear, that if the pre-exponential factor of the central trajectory undergoes numerical issues, the accuracy and reliability of the approximation should be comprimized. Assuming not relevant this inconvenience, this approximation is very suitable for on-the-fly calculations, where the evaluation of the hessian matrix, and so of the monodromy matrix, can be extremely demanding.

5.2 The adiabatic approximation

This approximation developed in Miller group assumes the monodromy matrix elements to be adiabatic with respect to each other.[80, 81] First of all, we rewrite Eq. (3.2.3) in terms of two auxiliary variables $\mathbf{Q}_t$ and $\mathbf{P}_t$ defined as

$$\begin{cases} \mathbf{Q}_t = & \mathbf{M}_{qq} - i\hbar\mathbf{M}_{qp}\gamma \\ \mathbf{P}_t = & \mathbf{M}_{pq} - i\hbar\mathbf{M}_{pp}\gamma. \end{cases} \tag{5.2.1}$$

Then we can write the pre-exponential factor as

$$C_t\left(\mathbf{q}_0, \mathbf{p}_0\right) = \sqrt{\det\left[\frac{1}{2}\left(\mathbf{Q}_t + \frac{i}{\hbar\gamma}\mathbf{P}_t\right)\right]}. \tag{5.2.2}$$

Now, it is noteworthy to observe that not only $\mathbf{P}_t$ is the time-derivative of $\mathbf{Q}_t$, both are also coupled *via* Newton's type equations

$$\begin{cases} \mathbf{P}_t = \dot{\mathbf{Q}}_t \\ \dot{\mathbf{P}}_t = -\mathbf{K}_t\mathbf{Q}_t. \end{cases} \tag{5.2.3}$$

The second equality of Eq. (5.2.3) can be obtained by applying a further time-derivative

of $\mathbf{P}_t$ indeed

$$\dot{\mathbf{P}}_t = \frac{\partial \dot{\mathbf{p}}_t}{\partial \mathbf{q}_0} - i\hbar \frac{\partial \dot{\mathbf{p}}_t}{\partial \mathbf{p}_0}\gamma, \tag{5.2.4}$$

and by taking advantage of Newton's equations, *i.e.* $\dot{\mathbf{p}}_t = -\mathbf{K}_t\mathbf{q}_t$ we obtain

$$\dot{\mathbf{P}}_t = -\mathbf{K}_t \left[\frac{\partial \mathbf{q}_t}{\partial \mathbf{q}_0} - i\hbar \frac{\partial \mathbf{q}_t}{\partial \mathbf{p}_0}\gamma\right] = -\mathbf{K}_t\mathbf{Q}_t. \tag{5.2.5}$$

Now, if we assume that the unitary matrix $\mathbf{U}$ that diagonalizes the Hessian matrix, diagonalizes also $\mathbf{Q}_t$ and $\mathbf{P}_t$

$$\begin{cases} \tilde{\mathbf{K}}_t = \boldsymbol{U}\mathbf{K}_t\mathbf{U}^T \\ \tilde{\mathbf{Q}}_t = \boldsymbol{U}\mathbf{Q}_t\mathbf{U}^T \\ \tilde{\mathbf{P}}_t = \boldsymbol{U}\mathbf{P}_t\mathbf{U}^T \end{cases} \tag{5.2.6}$$

we can write the pre-exponential factor only in terms of diagonal elements of $\tilde{\mathbf{Q}}_t$ and $\tilde{\mathbf{P}}_t$

$$C_t\left(\mathbf{q}_0, \mathbf{p}_0\right) \sim \sqrt{\prod_{i=1}^{N_{vib}} \left[\frac{1}{2}\left(\tilde{Q}_t\left(i,i\right) + \frac{i}{\hbar\gamma}\tilde{P}_t\left(i,i\right)\right)\right]}. \tag{5.2.7}$$

Within this approximation, we save lot of computational time since we have to solve only $2 \times N_{vib}$ independent differential equations. Moreover, this approximation is expected to work very well in the case of adiabatic or quasi-adiabatic regimes, while accuracy will be damped with strong intermode couplings. Finally we highlight that the evolution of $\tilde{\mathbf{Q}}_t$ and $\tilde{\mathbf{P}}_t$ is still sensitive to the initial conditions, resulting into numerical instability of the pre-exponential factor reported in Eq. (5.2.7).

5.3 Log-derivative formulation of the pre-exponential factor

We now introduce the Log-Derivative formulation of the pre-exponential factor.[78] In this formulation, it is not necessary to evolve and to check the stability of the monodromy matrix. To start off we take the two auxiliary variables $\mathbf{Q}_t$ and $\mathbf{P}_t$ introduced in the previous section, and since $\mathbf{P}_t$ is the time-derivative of $\mathbf{Q}_t$, we call $\mathbf{R}_t = \frac{\dot{\mathbf{Q}}_t}{\mathbf{Q}_t}$ the Log-

Derivative of $\mathbf{Q}_t$. The pre-exponential factor written in Eq. (5.2.2) can be expressed as a function only of $\mathbf{R}_t$.

$$C_t\left(\mathbf{p}_0,\mathbf{q}_0\right)=\sqrt{\det\left[\frac{1}{2}\left(\mathbf{I}+\frac{i}{\hbar\gamma}\mathbf{R}_t\right)\right]}e^{\frac{1}{2}\int_0^t d\tau Tr(\mathbf{R}_t)}. \tag{5.3.1}$$

Eq. (5.3.1) states that the knowledge of $\mathbf{R}_t$ directly allows the evaluation of the pre-exponential factor without passing from the Monodromy Matrix. To calculate $\mathbf{R}_t$ we evaluate its time-derivative

$$\dot{\mathbf{R}}_t=\frac{\ddot{\mathbf{Q}}_t}{\mathbf{Q}_t}-\left(\frac{\dot{\mathbf{Q}}_t}{\mathbf{Q}_t}\right)^2=-\mathbf{K}_t-\mathbf{R}_t. \tag{5.3.2}$$

$\mathbf{R}_t$ is the solution of a Riccati equation involving the Hessian matrix and having as initial conditions $\mathbf{R}_0=-i\hbar\gamma$. Thus, we have to solve the following first-order differential equation to calculate the pre-exponential factor.

$$\begin{cases}\dot{\mathbf{R}}_t=-\mathbf{K}_t-\mathbf{R}_t.\\ \mathbf{R}_0=-i\hbar\gamma\end{cases} \tag{5.3.3}$$

Unfortunately, for a generical potential Eq. (5.3.2) is not analytically solvable and some approximations or numerical integrations have to performed. Accurate integrators of Eq. (5.3.2) can be found in the Literature.[82] On the opposite, this formulation allow to forget about the evaluation and evolution of the monodromy matrix elements.

5.3.1 Existing approximations

5.3.1.1 The harmonic approximation

A very crude but simple solution of the Riccati equation is obtained if we approximate the potential to be harmonic close to the minimum. Within this approximation we have $\mathbf{K}_t\sim\boldsymbol{\omega}^2$, where $\boldsymbol{\omega}^2$ is the diagonal Hessian matrix around the equilibrium configuration.

The Riccati equation, in this case is analytically solvable, and has a constant solution, derived in the appendix section (11.3). The result is $\mathbf{R}_t = -i\boldsymbol{\omega}$ and the pre-exponential factor becomes

$$C_t^{HO}(\mathbf{p}_0, \mathbf{q}_0) = e^{-\frac{1}{2}\sum_{i=1}^{N_{vib}} \omega_i t}. \tag{5.3.4}$$

In the case of harmonic systems, or eventually by employing the approximation, the pre-exponential factor has always a constant modulos (equal to 1); thus by employing such approximation all issues concerning the rejection of the classical trajectories are prevented. Nevertheless, the accuracy of the approximation is sometimes very low, especially for strongly anharmonic potentials.

5.3.1.2 The Johnson Multichannel Approximation

To make a step further from the harmonic approximation one can assume that for a generic time-dependent hessian matrix, the first derivative $\dot{\mathbf{R}}_t$ is slowly varying, *i.e.* close to an harmonic behaviour. In this picture we have to solve

$$\begin{cases} 0 = -\mathbf{K}_t - \mathbf{R}_t \\ \mathbf{R}_0 = -i\hbar\gamma \end{cases} \tag{5.3.5}$$

that is again analytically solvable. Taking into account the initial conditions, the solution becomes

$$\mathbf{R}_t = -i\hbar\sqrt{\mathbf{K}_t}. \tag{5.3.6}$$

The pre-exponential factor will be

$$C_t^{Johnson}(\mathbf{p}_0, \mathbf{q}_0) = \sqrt{\det\left[\frac{1}{2}\left(\mathbf{I} + \frac{\sqrt{\mathbf{K}_t}}{\gamma}\right)\right]} e^{-\frac{i\hbar}{2}\int_0^t d\tau Tr\left(\sqrt{\mathbf{K}_t}\right)}, \tag{5.3.7}$$

and assuming $\gamma_i \sim \omega_{ii}\, \forall i \epsilon [1, N_{vib}]$, with ω_{ii} square roots of the eigenvalues of the hessian matrix, we obtain a more general but similar expression to Eq. (5.3.4)

$$C_t^{HO}(\mathbf{p}_0, \mathbf{q}_0) \sim e^{-\frac{1}{2}\sum_{i=1}^{N_{vib}} \omega_i(t) t}, \tag{5.3.8}$$

where now the frequencies are dependent from the dynamics.

5.3.2 New analytical and numerical approximations

5.3.2.1 An iterative strategy to improve the harmonic approximation

The presented pre-exponential factor approximations can undergo numerical instability in the case of chaotic trajectories. On an opposite side, the harmonic approximation

prevents such problems, but unfortunately for real molecular system is often inaccurate. One desires to combine both virtues, aiming to have a pre-exponential factor that from one side retains accuracy and from the other is numerically stable. We attempt to address it starting from the harmonic approximation $\mathbf{R}_t = -i\hbar\gamma$. Then we assume that the real Riccati solution is slightly different from the harmonic one, and similarly with it (and with the Johnson's one) its first derivative is equal to zero. Our ansatz is written as

$$\mathbf{R}_t^{(1)} = -i\hbar\gamma + \varepsilon \tag{5.3.9}$$

with $\dot{\mathbf{R}}_t^{(1)} \sim 0$. If we now substitute Eq. (5.3.9) into the Riccati Equation (5.3.2) we obtain

$$0 = (\hbar\gamma)^2 - 2i\hbar\gamma\varepsilon + \varepsilon^2 - \mathbf{K}_t, \tag{5.3.10}$$

and neglecting high order corrections, we obtain

$$\varepsilon = -\frac{i}{2}\left(\frac{\mathbf{K}_t}{\hbar\gamma} - \hbar\gamma\right). \tag{5.3.11}$$

The approximate solution is

$$\mathbf{R}_t^{(1)} = -\frac{i}{2}\left(\frac{\mathbf{K}_t}{\hbar\gamma} + \hbar\gamma\right). \tag{5.3.12}$$

Since hessian and gamma matrices elements are real, the solution will be imaginary for all times. If we now look at the Log-derivative formulation of the pre-exponential factor in Eq. (5.3.1), we note that the exponential part is of the type $e^{i\varphi_t}\ \varphi_t \epsilon \mathbb{R}$, and the pre-exponential part is instead real. Hence, in the separable approximation, the pre-exponential factor will be written as $e^{\frac{1}{2}\int_0^t d\tau Tr\left[\mathbf{R}_t^{(1)}\right]}$ and will not numerically diverge since it is an oscillating term. As a result, in the separable approximation even in the case of chaotic trajectories the numerical instability will be tamed. Such solution was already proposed by Miller.[78] One now can try to improve the accuracy of the solution by formulating a further ansatz with the same assumptions. In this case the solution will we

written as

$$\mathbf{R}_t^{(2)} = \mathbf{R}_t^{(1)} + \varepsilon. \tag{5.3.13}$$

After some algebric passages we obtain that

$$\varepsilon = \frac{i}{4} \frac{\left(\hbar\gamma - \frac{\mathbf{K}_t}{\hbar\gamma}\right)^2}{\left(\hbar\gamma + \frac{\mathbf{K}_t}{\hbar\gamma}\right)} \tag{5.3.14}$$

and then

$$\mathbf{R}_t^{(2)} = -\frac{i}{2}\left(\frac{\mathbf{K}_t}{\hbar\gamma} + \hbar\gamma\right) + \frac{i}{4} \frac{\left(\hbar\gamma - \frac{\mathbf{K}_t}{\hbar\gamma}\right)^2}{\left(\hbar\gamma + \frac{\mathbf{K}_t}{\hbar\gamma}\right)}. \tag{5.3.15}$$

Once again the approximate solution is imaginary and the pre-exponential factor will be $e^{\frac{1}{2}\int_0^t d\tau Tr\left[\mathbf{R}_t^{(2)}\right]}$ with a real pre-exponential part that is simplified in the separable approximation. We note that $\mathbf{R}_t^{(2)}$ can be written in terms of the original $\mathbf{R}_t^{(1)}$ guess as

$$\mathbf{R}_t^{(2)} = \mathbf{R}_t^{(1)} + \frac{1}{2^3} \frac{\left(\hbar\gamma - \frac{\mathbf{K}_t}{\hbar\gamma}\right)^2}{\mathbf{R}_t^{(1)}}. \tag{5.3.16}$$

This iterative tentative to improve the approximation can go further if we write

$$\mathbf{R}_t^{(3)} = \mathbf{R}_t^{(2)} + \varepsilon. \tag{5.3.17}$$

In this case the highest order approximate solution will be written in terms of $\mathbf{R}_t^{(2)}$ and $\mathbf{R}_t^{(1)}$ as

$$\mathbf{R}_t^{(3)} = \mathbf{R}_t^{(2)} - \frac{1}{2^7} \frac{\left(\hbar\gamma - \frac{\mathbf{K}_t}{\hbar\gamma}\right)^4}{\mathbf{R}_t^{(1)2}\mathbf{R}_t^{(1)}}. \tag{5.3.18}$$

Similarly if we go on by writing

$$\mathbf{R}_t^{(4)} = \mathbf{R}_t^{(3)} + \varepsilon, \tag{5.3.19}$$

we obtain

$$\mathbf{R}_t^{(4)} = \mathbf{R}_t^{(3)} + \frac{1}{2^{15}} \frac{\left(\hbar\gamma - \frac{\mathbf{K}_t}{\hbar\gamma}\right)^8}{\mathbf{R}_t^{(1)4}\mathbf{R}_t^{(2)2}\mathbf{R}_t^{(3)2}}. \tag{5.3.20}$$

In this fashion a generic $\mathbf{R}_t^{(n)}$ approximate solution will be described in terms of the lowest order solutions as

$$\mathbf{R}_t^{(n)} = \mathbf{R}_t^{(n-1)} + \frac{(-)^n}{2^{(2^n-1)}} \frac{\left(\hbar\gamma - \frac{\mathbf{K}_t}{\hbar\gamma}\right)^{2^{(n-1)}}}{\prod_{j=0}^{n-2}\left(\mathbf{R}_t^{(n-1-j)}\right)^{2^j}}. \tag{5.3.21}$$

We stress that this procedure is not a proper perturbative strategy since it does not provide the exact solution of Eq. (5.3.2) even for $n \to +\infty$ since at avery iteration the assumpion $\dot{\mathbf{R}}_t^{(n)} \sim 0$ is introduced. The approximate solution will be more accurate than the harmonic one for low values of n, while for higher values it probably will deviate, leading to uncorrect results because of the accumulation of approximations will prevail.

5.3.2.2 Monodromy matrix regularization

All approximations described up to now attempt to provide a pre-exponential factor as accurate as possible and are analytically obtained by approximating somehow the Riccati equation. In this section is instead described a methodology that does not provide an analytical approximation, while attemps to tame the exponential growing of the pre-exponential factor. In other words it relies only on numerical considerations.

More in details one can gain insights about the chaotic behaviour of a trajectory by looking at the eigenvalues of the monodromy matrix

$$\mathbf{M} = \mathbf{U}^{-1}\boldsymbol{\lambda}\mathbf{U}. \tag{5.3.22}$$

To tame the exponential growth of monodromy matrix elements we can campare the modulos of its eigenvalues with a threshold value. If the highest eigenvalue λ_k is higher than the threshold, then we build the "regularized" $\tilde{\boldsymbol{\lambda}}$, $\tilde{\mathbf{U}}^{-1}$, and $\tilde{\mathbf{U}}$ matrices, having set the k-th element, k-th row, and k-th column of $\boldsymbol{\lambda}$, $\mathbf{U}^{-1}$, and $\mathbf{U}$ equal to zero respectively.

$$\tilde{\boldsymbol{\lambda}} = \begin{pmatrix} \dots & & \\ & 0 & \\ & & \dots \end{pmatrix} \quad \tilde{\mathbf{U}}^{-1} = \begin{pmatrix} \dots & \dots & \dots \\ 0 & 0 & 0 \\ \dots & \dots & \dots \end{pmatrix} \quad \tilde{\mathbf{U}} = \begin{pmatrix} \dots & 0 & \dots \\ \dots & 0 & \dots \\ \dots & 0 & \dots \end{pmatrix}. \tag{5.3.23}$$

Now, it is possible to go back and to calculate the regularized monodromy matrix as

$$\tilde{\mathbf{M}} = \tilde{\mathbf{U}}\tilde{\boldsymbol{\lambda}}\tilde{\mathbf{U}}^{-1} \tag{5.3.24}$$

and the pre-exponential factor

$$\tilde{C}_t\left(\mathbf{q}_0, \mathbf{p}_0\right) = \sqrt{\det\left[\frac{1}{2}\left(\tilde{\mathbf{M}}_{\mathbf{qq}} + \frac{1}{\gamma}\tilde{\mathbf{M}}_{\mathbf{pp}}\gamma + \frac{i}{\hbar\boldsymbol{\gamma}}\tilde{\mathbf{M}}_{\mathbf{pq}} + \frac{\hbar}{i}\tilde{\mathbf{M}}_{\mathbf{qp}}\boldsymbol{\gamma}\right)\right]}. \tag{5.3.25}$$

Within this procedure, the exponential growth is tamed, and the chaotic behaviour is quenched. The best way to take advantage of this method is to use a threshold parameter as high as possible, regularizing the minimum times as possible the monodromy matrix, in order to have good spectral densities. In this way the artificial modification of the monodromy matrix will be minimized and the accuracy of spectra won't be affected.

5.4 Numerical Tests

The pre-exponential factor approximations are tested against tailored model potential and real molecular systems. Calculations are performed using TA-SCIVR and standard Herman-Kluk SCIVR when possible from a computational point of view. Model systems are designed in order to introduce a high level of chaos, while molecular systems span from strong inter-mode coupled molecules to extremely chaotic ones. All the tests should provide a quite broad scenario of applicability and accuracy of the proposed approximations.

5.4.1 A) Bi-dimensional Henon-Heiles potential

We start from the bi-dimensional Henon-Heiles potential reported in Eq. (5.4.1)

$$V\left(q_1, q_2\right) = \frac{1}{2}\left(q_1^2 + q_2^2\right) + \lambda x^2 y - \frac{1}{3}\lambda y^3. \tag{5.4.1}$$

The mass and the frequency are unitary (in atomic units scale). We choose the value of λ parameter equal to 0.11803, which is a value already studied in the Literature.[55, 83]

Such a potential is known to describe a chaotic behaviour, and within our purposes it represents a good test for our pre-exponential factor approximations both with standard SCIVR spectral density and with the Time Averaging filter (TA-SCIVR). Starting from SCIVR calculations, we run 10^7 trajectories in order to have converged spectra. The sampling of the trajectories is done according to the Box-Mueller distribution centered at $(\mathbf{p}_{eq}, \mathbf{q}_{eq})$ where $\mathbf{p}_{eq}$ is the square root of the eigenvalues of the Hessian matrix at the equilibrium, and $\mathbf{q}_{eq}$ is the equilibrium geometry (In Eq. (5.4.1) $\mathbf{q}_{eq} = (0, 0)$). Each classical trajectory is 50000 atomic units long. Figure (5.4.1) reports our computed spectra with different pre-exponential factor approximations and in Table (5.1) are reported the corresponding energy levels. Starting by looking at the second and third columns of Table (5.1) we observe that the Herman-Kluk SCIVR calculations with the two rejection criteria of the classical trajectories lead to very accurate and comparable results. Also the number of rejected trajectories is very similar, 28% using Eq. (3.2.9) and 26% using Eq. (3.2.8), where in our calculations we have set $\varepsilon = 10^{-5}$ and $D_t = 10^7$ according with previous works. When the pre-exponential factor is approximated only 10^6 classical trajectories are enough to obtain reliable spectra. The most accurate results are recovered by employing the Monodromy matrix regularization of Eq. (5.3.25), resulting into 28% of classical trajectories "regularized" at least one time. On the other hand, the most crude approximation is the harmonic one, with relevant deviations at high energies. When the pre-exponential factor is calculated using the iterative $\mathbf{R}_t^{(1)}$ approximation (Eq. 5.3.12), the mean absolute error (MAE) with respect to the exact levels is 0.038, that is reduced to 0.013 when the higher order $\mathbf{R}_t^{(2)}$ and $\mathbf{R}_t^{(3)}$ approximations are employed (Eqs. 5.3.16,5.3.18). The Poor person approximation (Eq. 5.1.1) is in this case comparable with $\mathbf{R}_t^{(2)}$ and $\mathbf{R}_t^{(3)}$, showing a MAE equal to 0.015. Finally the Johnson and adiabatic approximations undergo numerical issues with this type of chaotic potential.

In the case of TA-SCIVR calculations we ran only 5000 classical trajectories since roughly 10^3 classical trajectories per degree of freedom are enough for converged spectra.

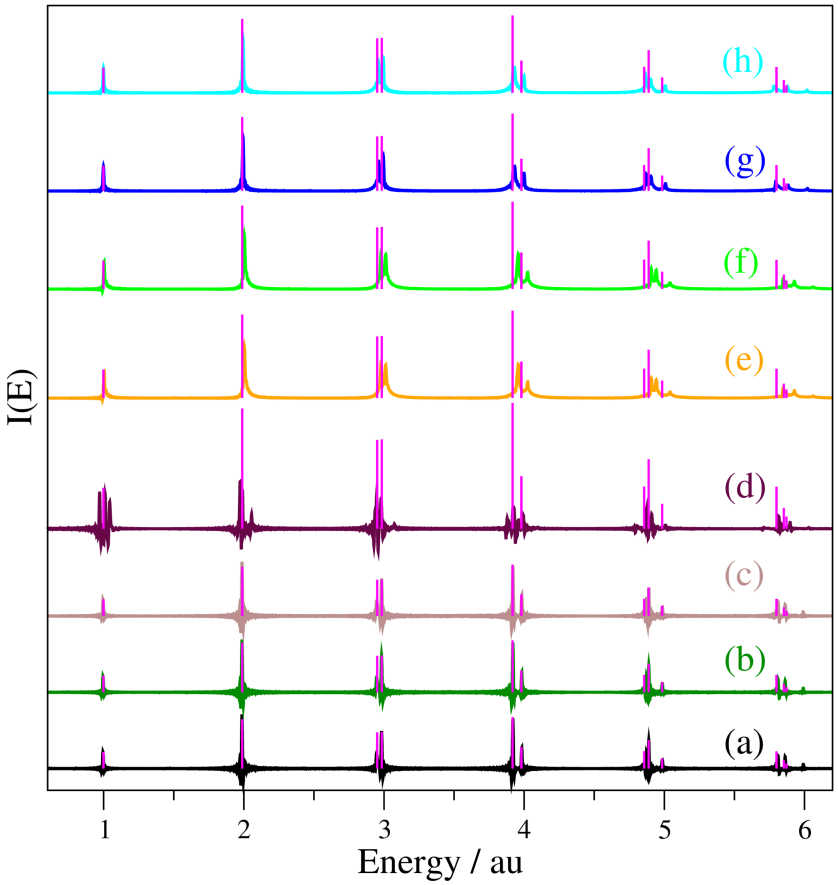

Figure 5.4.1: Energy levels of bidimensional Henon-Heiles potential reported in Eq. (5.4.1). (a) Black continuous lines are for the rejection criterion of Eq. (3.2.9) with $\varepsilon = 10^{-5}$; (b) dark green continuous lines for the rejection method of Kay Eq. 3.2.8; (c) brown for the regularization of the monodromy matrix of Eq. (5.3.25); (d) maroon for the PPs approximation reported in Eq. (5.1.1); (e) orange for the harmonic pre-exponential factor approximation pf Eq. (5.3.4); (f) light green spectrum for the approximation $\mathbf{R}_t^{(1)}$ in Eq. (5.3.12); (g) blue for the pre-exponential factor $\mathbf{R}_t^{(2)}$ in Eq. (5.3.16), and (h) cyan $\mathbf{R}_t^{(3)}$ in Eq. (5.3.18). Exact quantum mechanical values are indicated by the vertical magenta lines with a height which is equal to the square of the overlap between the SC reference state and the exact eigenstate calculated by DVR.[13]

Table 5.1: Power spectrum of the Henon-Heiles potential in Eq. (5.4.1). Energy levels are reported in Atomic units. From left to right: Exact DVR values, SC-IVR values using the rejection criterium $1 - \det \left| \mathbf{M}^T(t)\, \mathbf{M}(t) \right| > 10^{-5}$, SC-IVR calculation using the ad hoc Kay's rejection method of Eq.(3.2.8), SC-IVR calculation using the monodromy matrix regularization (5.3.25), the PPs approximation (5.1.1), the harmonic approximation (5.3.4), $\mathbf{R}_t^{(1)}$ approximation (5.3.12), and our approximations of Eqs. (5.3.16) and (5.3.18). In the last row the Mean Average Errors (MAE) are reported.

	Exact	SCIVR	Kay's method	Regularization	PPs	HO	$\mathbf{R}_t^{(1)}$	$\mathbf{R}_t^{(2)}$	$\mathbf{R}_t^{(3)}$
	0.998	0.995	0.995	0.995	0.971	1.003	1.003	0.998	0.998
	1.989	1.987	1.987	1.987	1.974	2.004	2.004	1.994	1.994
	1.989	1.987	1.987	1.987	1.974	2.004	2.004	1.994	1.994
	2.951	2.947	2.948	2.948	2.948	2.979	2.979	2.962	2.961
	2.984	2.983	2.983	2.983	2.980	3.012	3.012	2.995	2.994
	2.984	2.983	2.983	2.983	2.980	3.012	3.012	2.995	2.994
	3.917	3.92	3.920	3.920	3.920	3.958	3.958	3.931	3.931
	3.918	3.92	3.920	3.920	3.920	3.958	3.958	3.931	3.931
	3.980	3.982	3.982	3.983	3.995	4.025	4.025	4.000	3.999
	3.984	3.982	3.982	3.983	3.995	4.025	4.025	4.000	3.999
	4.856	4.873	4.873	4.874	4.876	4.907	4.907	4.868	4.864
	4.888	4.889	4.889	4.889	4.910	4.942	4.942	4.906	4.903
	4.888	4.889	4.889	4.889	4.910	4.942	4.942	4.906	4.903
	4.985	4.985	4.985	4.986	5.009	5.041	5.041	5.008	5.007
	4.985	4.985	4.985	4.986	5.009	5.041	5.041	5.008	5.007
	5.800	5.812	5.811	5.811	5.818	5.849	5.849	5.795	5.783
	5.800	5.812	5.811	5.811	5.818	5.849	5.849	5.795	5.783
	5.853	5.862	5.862	5.862	5.833	5.863	5.863	5.882	5.878
	5.872	5.878	5.878	5.878	5.898	5.928	5.928	5.882	5.878
MAE		0.004	0.004	0.004	0.015	0.038	0.038	0.013	0.013

Table 5.2: Power spectrum of the Henon-Heiles potential in Eq. (5.4.1). Energy levels are reported in Atomic units. From left to right: Exact DVR values, SC-IVR values using the rejection criterium $1 - \det \left|\mathbf{M}^T(t)\,\mathbf{M}(t)\right| > 10^{-5}$, SC-IVR calculation using the ad hoc Kay's rejection method of Eq.(3.2.8), SC-IVR calculation using the monodromy matrix regularization (5.3.25), the adiabatic approximation (5.2.7), the PPs approximation (5.1.1), the harmonic approximation (5.3.4), $\mathbf{R}_t^{(1)}$ approximation (5.3.12), and our approximations of Eqs. (5.3.16) and (5.3.18). In the last row the Mean Average Errors (MAE) are reported.

	Exact	SC-IVR	Kay's method	Regularization	Adiabatic	PPs	HO	$\mathbf{R}_t^{(1)}$	$\mathbf{R}_t^{(2)}$	$\mathbf{R}_t^{(3)}$
	0.998	0.995	0.995	0.995	0.998	0.965	1.003	1.003	0.997	0.997
	1.989	1.988	1.988	1.988	1.995	1.967	2.004	2.004	1.993	1.993
	1.989	1.988	1.988	1.988	2.012	2.001	2.038	2.038	2.007	2.005
	2.951	2.901	2.901	2.901	2.923	2.913	2.950	2.950	2.917	2.917
	2.984	2.983	2.983	2.982	3.004	2.994	3.031	3.031	2.997	2.996
	2.984	2.983	2.983	2.982	3.004	2.994	3.031	3.031	2.997	2.996
	3.917	3.893	3.893	3.893	3.916	3.907	3.943	3.942	3.911	3.910
	3.918	3.893	3.893	3.893	3.916	3.907	3.943	3.942	3.911	3.910
	3.980	3.975	3.975	3.975	3.997	3.987	4.024	4.023	3.993	3.992
	3.984	3.975	3.975	3.975	3.997	3.987	4.024	4.023	3.993	3.992
	4.856	4.805	4.805	4.805	4.828	4.818	4.854	4.853	4.822	4.821
	4.888	4.886	4.886	4.886	4.909	4.899	4.935	4.934	4.902	4.912
	4.888	4.886	4.886	4.886	4.909	4.899	4.935	4.934	4.902	4.912
	4.985	4.970	4.97	4.97	4.99	4.968	5.005	5.004	4.984	4.984
	4.985	4.970	4.97	4.97	5.003	4.968	5.005	5.004	5.002	5.000
	5.800	5.798	5.798	5.798	5.820	5.810	5.846	5.845	5.811	5.812
	5.800	5.798	5.798	5.798	5.820	5.810	5.846	5.845	5.811	5.812
	5.853	5.859	5.859	5.859	5.835	5.857	5.894	5.893	5.874	5.870
	5.872	5.879	5.879	5.879	5.902	5.892	5.929	5.927	5.896	5.894
MAE		0.011	0.011	0.012	0.017	0.016	0.033	0.032	0.014	0.015

Table (5.2) reports the computed energy levels by employing different pre-exponential approximations, while Figure (5.4.2) shows the computed spectra. We observe that in general we find quite less accurate results with respect to the previous case, according to the fact that in the parent calculations the separable approximation was introduced. Nevertheless, energy levels are still very accurate. In particular, once again when we do not approximate the pre-exponential factor, results are unchanged moving from a rejection criterion to another. When the analytical and numerical pre-exponential factor approximations are employed, the monodromy matrix regularization is still the best one, showing energy levels comparable with those obtained with the standard pre-exponential factor.

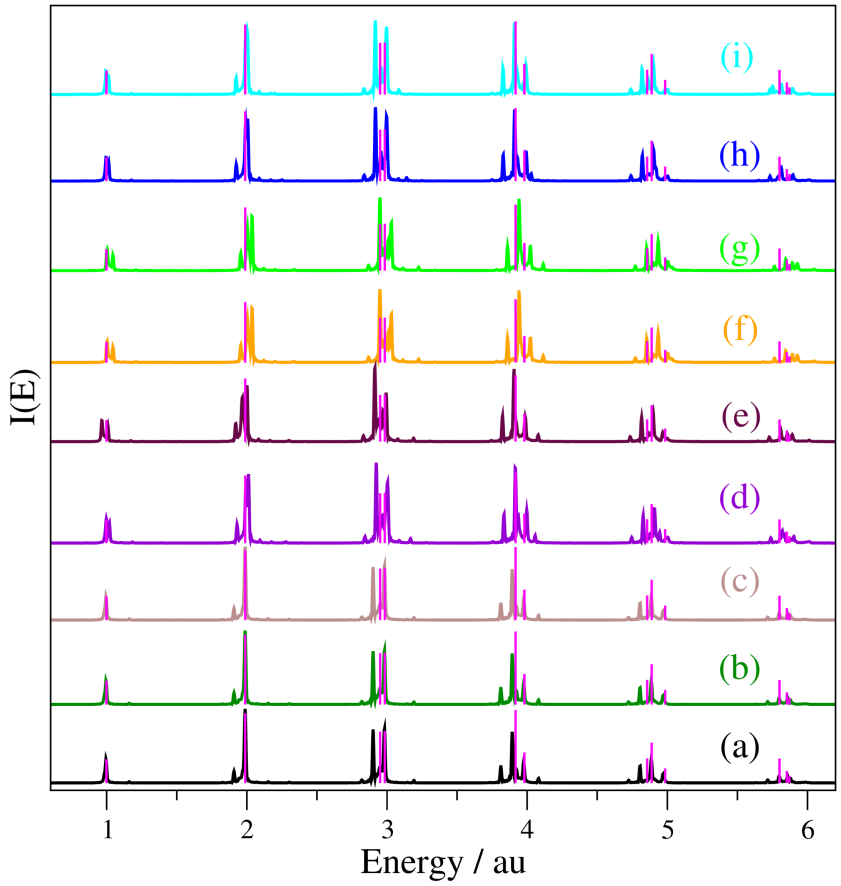

Figure 5.4.2: TA-SCIVR Energy levels of bidimensional Henon-Heiles potential reported in Eq. (5.4.1). (a) Black continuous lines are for the rejection criterion of Eq. (3.2.9) with $\varepsilon = 10^{-5}$; (b) dark green continuous lines for the rejection method of Kay Eq. 3.2.8; (c) brown for the regularization of the monodromy matrix of Eq. (5.3.25); (d) violet for the adiabatic approximation of Eq. (5.2.7); (e) maroon for the PPs approximation reported in Eq. (5.1.1); (f) orange for the harmonic pre-exponential factor approximation of Eq. (5.3.4); (g) light green spectrum for the approximation $\mathbf{R}_t^{(1)}$ in Eq. (5.3.12); (h) blue for the pre-exponential factor $\mathbf{R}_t^{(2)}$ in Eq. (5.3.16), and (i) cyan $\mathbf{R}_t^{(3)}$ in Eq. (5.3.18). Exact quantum mechanical values are indicated by the vertical magenta lines with a height which is equal to the square of the overlap between the SC reference state and the exact eigenstate calculated by DVR.[13]

Table 5.3: Parameters of the potential reported in Eq. (5.4.2).

ω_1/cm^{-1}	ω_2/cm^{-1}	D/au	λ/au	β/au	q_1^{eq}=q_2^{eq}
3000	1700	0.2	10^{-6}	0.02	0.0

In this case, only 12% of trajectories were regularized at least one time. Similarly to the previous case, the harmonic approximation of Eq. (5.3.4) comes to be the less accurate one and it is comparable with the iterative approximation $\mathbf{R}_t^{(1)}$of Eq. (5.3.12), leading to 0.032 of MAE. Results improves when the high order $\mathbf{R}_t^{(2)}$ or $\mathbf{R}_t^{(3)}$approximation are employed, in this case the MAE decreases to 0.014 and 0.015 respectively. Differently from the previous calculations the lower number of classical trajectories probably tames the numerical instability of the adiabatic approximation, that in the case of TA-SCIVR calculations allows to recover a detectable spectral density. The approximation performance is comparable with those of the high order $\mathbf{R}_t^{(2)}$ or $\mathbf{R}_t^{(3)}$, leading to 0.017 MAE. Finally, again in this case, the Johnson approximation undergoes numerical issues, not allowing to obtain a definite signal.

5.4.2 B) Bi-dimensional quartic-like potential

We now look for another bi-dimensional potential made by two Morse oscillators with a quartic-like term. The potential is

$$V(\mathbf{q}) = \sum_{i=1}^{2} D\left[1 - e^{-\alpha_i(q_i - q_i^{eq})}\right]^2 + \lambda\left[\frac{1}{2}\left((q_1 - q_1^{eq})^4 + (q_2 - q_2^{eq})^4\right) + \frac{\beta}{4}(q_1 - q_1^{eq})^2(q_2 - q_2^{eq})^2\right] \quad (5.4.2)$$

and the parameters are reported in Table (5.4.2). The quartic like term introduces a extremely high chaotic regime, as can evinced by looking at the number of rejected classical trajectories reported below. However, the potential at equilibrium configuration $\mathbf{q}_{eq}$ is described by two Morse oscillators, allowing us to employ all the prexponential factor approximations, even those based on iterative perturbations of the harmonic approximation. We run 10^8 classical trajectories in the case of SCIVR calculations, because of the very high value of rejection, which approaches 97% and 96% by using Eqs. (3.2.9) and (3.2.8)

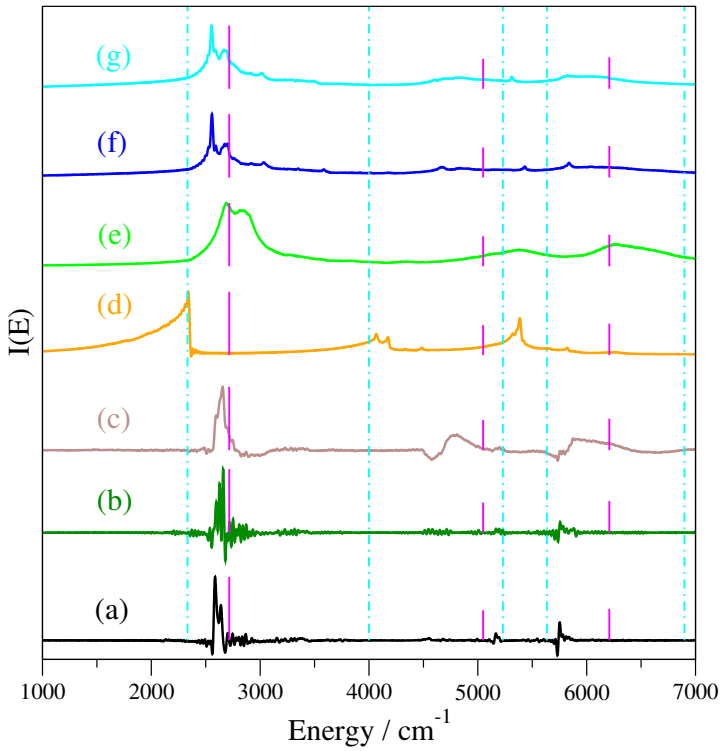

Figure 5.4.3: SCIVR Energy levels of potential reported in Eq. (5.4.2). (a) Black continuous lines are for the rejection criterion of Eq. (3.2.9) with $\varepsilon = 10^{-3}$; (b) dark green continuous lines for the rejection method of Kay Eq. (3.2.8); (c) brown for the regularization of the monodromy matrix of Eq. (5.3.25); (d) orange for the harmonic pre-exponential factor approximation of Eq. (5.3.4); (e) light green spectrum for the approximation $\mathbf{R}_t^{(1)}$ in Eq. (5.3.12); (f) blue for the pre-exponential factor $\mathbf{R}_t^{(2)}$ in Eq. (5.3.16), and (g) cyan $\mathbf{R}_t^{(3)}$ in Eq. (5.3.18). Exact quantum mechanical values are indicated by the vertical magenta lines with a height which is equal to the square of the overlap between the SC reference state and the exact eigenstate calculated by DVR[13]. Vertical cyan dashed dotted lines are centered at uncoupled energy levels, i.e. assuming $\lambda = 0$.

with $\varepsilon = 10^{-3}$ and $D_t = 10^8$. When approximations of the pre-exponential factor are employed, 10^7 classical trajectories are performed. Similarly to the Henon Heiles potential of Eq. (5.4.1), each classical trajectory is 50000 au long and the trajectories are sampled by using a box-muller distribution centered at $(\mathbf{p}_{eq}, \mathbf{q}_{eq})$, where $\mathbf{p}_{eq}$ is the square root of the eigenvalues of the Hessian matrix at the equilibrium. Figure (5.4.3) shows the computed spectra, where we observe that once again results arising from different rejection criteria are comparable and the Monodromy matrix regularization Eq. (5.3.25) (brown line) very well behaves into reproducing the first three energy levels. On the opposide side we find the harmonic approximation, which instead moves toward uncoupled estimates. The

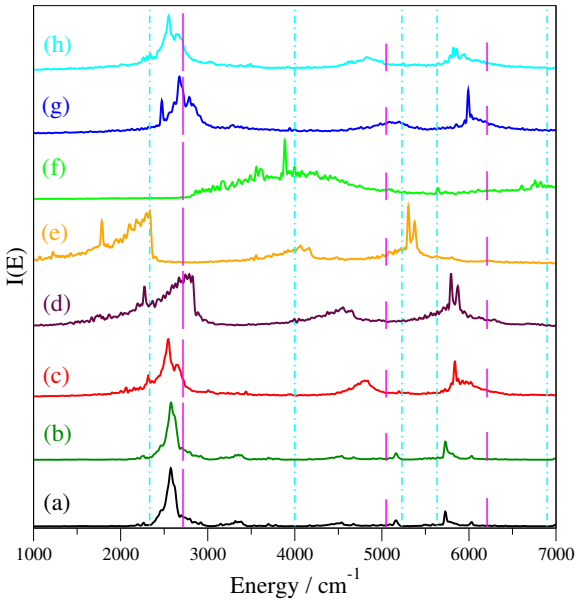

Figure 5.4.4: TA-SCIVR Power spectrum of the potential (5.4.2) with $\lambda = 10^{-6}$ using the time averaged formula. (a) Black line for the rejection criterium $1 - \det\left|\mathbf{M}^T(t)\,\mathbf{M}(t)\right| > 10^{-3}$, (b) dark green line for the Kay's rejection method of Eq. (3.2.8), (c) red line for the Johnson's approximation spectrum, (d) maroon line for the spectrum computed using the PPs approximation, (e) orange line for the HO spectrum, (f) light green line for the $\mathbf{R}_t^{(1)}$ approximation spectrum, (g) blue line for the spectrum computed using Eq.(5.3.16), and (h) cyan line for the spectrum computed using Eq.(5.3.18). The vertical magenta lines represent the exact energy levels with an intensity equals to the square of the overlap between the SC reference state $|\chi\rangle$ and the exact eigenstate calculated by DVR. The vertical cyan dash-dotted lines are the uncoupled Morse potential energy levels.

Johnson, the PP and the adiabatic approximations are instead plagued by the high chaotic regime. When time averaging calculations are employed we need only 80000 classical trajectories for accurate spectra, and 5000 in the case of approximated pre-exponential factors. Fig. (5.4.4) reports the power spectra at different semiclassical pre-exponential factor level of approximation. The (a) spectrum is the original TA-SC-IVR spectrum of Eq.(11.2.12) using $1 - \det\left|\mathbf{M}^T(t)\,\mathbf{M}(t)\right| > 10^{-3}$, while the spectrum (b) is obtained employing the *ad-hoc* method of Kay (3.2.8). The (c) spectrum is obtained using the Johnson's approximation (5.3.8), the (d) spectrum is computed using the PPs approximation (5.1.1), the (e) spectrum the harmonic approximation (11.3.2), the (f) spectrum using $\mathbf{R}_t^{(1)}$ approximation (5.3.12), the (g) spectrum using $\mathbf{R}_t^{(2)}$, and, finally, the (h) spectrum using $\mathbf{R}_t^{(3)}$. The exact values are indicated as vertical magenta lines with intensity equals

to the overlap between the SC reference state $|\chi\rangle$ and the DVR eigenvector, while the uncoupled Morse oscillators values are the vertical dot-dashed cyan lines. The adiabatic approximation and the monodromy matrix regularization couldn't be applied because of the chaotic regime. The time averaged spectra reported in black and dark green lines are quite approximated according with the toughness of the potential. In all cases, only the first three energy levels are recovered and for some approximations, as $\mathbf{R}_t^{(1)}$, the spectrum is too noisy to judge. However, even in the case of an extremely chaotic potential, which can not describe realistic pictures, pre-exponential factor approximations hold, allowing to recover a spectroscopic signal. For this reason we believe in the case of realistic potentials, they can better mimic the exact spectroscopic sequence.

5.4.3 c) H_2O

We now move toward real molecular systems, starting from the water molecule. Despite its low dimensionality it represents a very tough challenge for pre-exponential factor approximations, because of its high anharmonicity. We perform TA-SCIVR calculations by running 8000 trajectories. Each classical trajectory is evolved for 30000 atomic units under the potential energy surface of Bowman *et al*,[56] for which exact vibrational energy levels are available. The trajectories are sampled by using the Husimi distribution centered at $(\mathbf{p}_{eq}, \mathbf{q}_{eq})$ where $\mathbf{p}_{eq}$ is the square root of the eigenvalues of the Hessian matrix at the equilibrium, and $\mathbf{q}_{eq}$ is the equilibrium configuration. Each classical trajectory is propagated up to 30000 atomic units. When the pre-exponential factor is not approximated the chaotic regime leads to an high fraction (56%) of trajectories to be rejected, by employing $\varepsilon = 10^{-5}$. When instead the pre-exponential factor is evaluated by means of the monodromy matrix regularization only 2.1% undergo a correction, suggesting that the chaotic trajectories that are rejected using Eq. (3.2.9) do no affect, but instead contribute to the accuracy of the spectra. The estimated energy levels are reported in Table (5.4), while the symmetry decomposed A_1 and B_2 computed spectra of C_{2v} point group are

Table 5.4: Vibrational energy levels of H_2O. Wavenumbers unit. First column reports the spectroscopic terms, second column reports the exact quantum mechanical values, third column reports the results computed with TA-SCIVR using the rejection criterium $1 - \det\left|\mathbf{M}^T(t)\,\mathbf{M}(t)\right| > 10^{-5}$, fourth column SCIVR calculation using the ad hoc Kay's rejection method of Eq.(3.2.8), and the others with the different pre-exponential factor approximations named as above. In the last row is reported the Mean Absolute Error (MAE) of each column.

State	Exact[56]	SC-IVR	Kay's method	Regularization	Adiabatic	Johnson	PPs	HO	$\mathbf{R}_t^{(1)}$	$\mathbf{R}_t^{(2)}$	$\mathbf{R}_t^{(3)}$
ZPE	4631.6	4636	4640	4639	4592	4612	4604	4784	4704	4616	4612
$A_1\,(1_1)$	1591.2	1584	1580	1583	1556	1564	1616	1620	1576	1564	1564
$A_1\,(1_2)$	3146.1	3132	3132	3133	3124	3092	3196	3196	3124	3098	3096
$A_1\,(2_1)$	3655.4	3672	3680	3681	3596	3604	3752	3756	3724	3620	3606
$B_2\,(3_1)$	3751.1	3764	3760	3761	3808	3708	3730	3848	3808	3706	3707
$A_1\,(1_3)$	4662.5	4650	4628	4627	4564	4596	4723	4726	4648	4507	4652
$A_1\,(1_12_1)$	5230.5	5248	5248	5245	5216	5152	5348	5352	5284	5157	5152
$B_2\,(1_13_1)$	5322.4	5300	5300	5301	5344	5216	5242	5424	5352	5232	5215
$A_1\,(1_22_1)$	6768.9	6764	6768	6770	6688	6666	7005	7008	6804	6678	6655
$B_2\,(1_23_1)$	6858.8	6804	6800	6808	6848	6692	6738	6996	6844	6721	6693
$A_1\,(2_2)$	7202.3	7240	7228	7229	7068	7088	7392	7392	7300	7113	7092
$B_2\,(2_13_1)$	7254.4	7282	7266	7267	7328	7144	7176	7488	7372	7165	7148
$A_1\,(3_2)$	7438.2	7424	7404	7405	7572	7300	7620	7624	7516	7317	7288
$A_1\,(1_12_2)$	8767.5	8768	8772	8773	8702	8600	8603	8976	8832	8608	8596
$B_2\,(1_12_13_1)$	8812.1	8816	8800	8803	8860	8632	8672	9040	8872	8662	8642
$A_1\,(1_13_2)$	8990.4	8924	8920	8916	9004	8970	9108	8890			
MAE		20	22	22	57	90	107	140	53	89	92

reported in Figure (5.4.5). We can observe that the accuracy remains almost unchanged moving from a rejection criterion to another. Furthermore, and most importantly, the monodromy matrix regularization of the pre-exponential factor provides energy levels comparable with the reference ones. Moreover, the adiabatic approximation is quite accurate while the Johnson's one is comparable with the iterative perturbative solutions of Eqs. (5.3.16) and (5.3.18). Surprisingly, moving from $\mathbf{R}_t^{(1)}$ to $\mathbf{R}_t^{(2)}$ an increment of accuracy is not observed problably because of the high level of anharmonicy of the molecule, which is not properly accounted if a further perturbation (with harmonic assumptions) of an already approximate solution of Eq. (5.3.2) is considered. However, all the approximations perform much better than the poor person's and the harmonic ones, whose are expected to show high deviations, simply because they are not designed to be accurate for

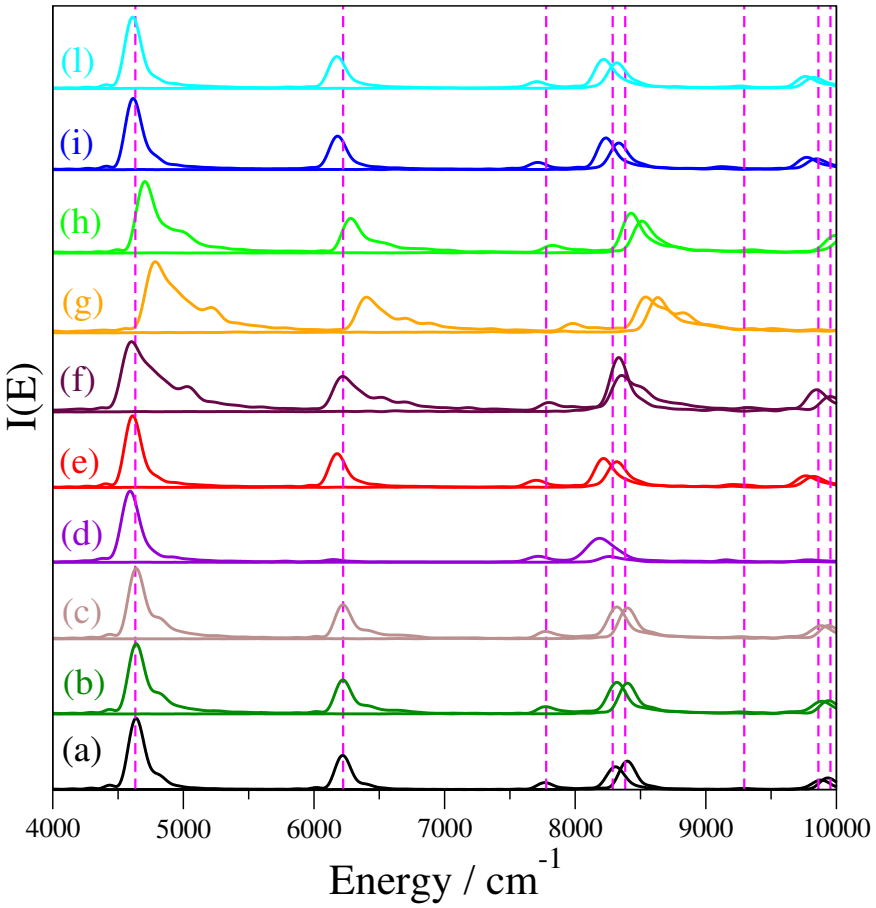

Figure 5.4.5: H_2O spectra. (a) Black line for the separable SC-IVR (11.2.12) spectrum using the rejection criterium $1 - \det \left| \mathbf{M}^T(t)\, \mathbf{M}(t) \right| > 10^{-5}$, (b) using the ad hoc Kay's rejection method of Eq.(3.2.8), (c) brown for the regularization of the monodromy matrix of Eq.(5.3.25), (d) violet line for the adiabatic approximation (5.2.7) spectrum, (e) red line for the Johnson's approximation (5.3.8) spectrum, (f) maroon line for the PPs approximation (5.1.1) spectrum, (g) orange line for the HO (11.3.2) approximation spectrum, (h) green line for the $\mathbf{R}_t^{(1)}$ approximation (5.3.12) spectrum, (i) blue line for the spectrum computed using $\mathbf{R}_t^{(2)}$ in Eq.(5.3.16), and (l) cyan line for the spectrum computed using $\mathbf{R}_t^{(3)}$ in Eq.(5.3.18). The vertical magenta dashed lines represent the quantum energy levels. A_1 and B_2 spectra with the same color for each approximation.

high anharmonic systems. Finally, we point out that the monodromy matrix regularization is even as accurate as the standard TA-SCIVR results.

5.4.4 d) CO_2

After a strong anharmonic system we switch onto a more harmonic but also challenging molecule, because of the presence of strong Fermi resonances. We employ the Potential Energy Surface of Chedin,[84] running 15000 classical trajectories for the phase space integration, both with and without the pre-exponential factor approximations. Each classical trajectory is propagated for 30000 atomic units. For this system, the lower chaotic regime with respect to water can be evinced by looking at the low number of rejected trajectories, equal to 14% and 8% when the Monodromy matrix based criterion of Eq. (3.2.9) and the *ad-hoc* method of Kay of Eq. (3.2.8) are employed. Furthermore, when the classical trajectories are regularized by using Eq. (5.3.25), only 0.6% undergo at least one correction. TA-SCIVR computed frequencies with the different pre-exponential factor approximations are compared with exact energy levels of Vasquez *et al.*[85] Table (5.5) shows our computed estimates compared with exact one. One again we observe that the two rejection methods provide comparable results and the monodromy matrix regularization is as accurate as if one does not approximate the pre-exponential factor. All the other pre-exponential factor approximations provide very accurate estimates for both fundamental and overtone excitations, with the harmonic and the poor person's ones that are the least accurate with MAEs equal to 12.4 and 11.4 wavenumbers, respectively.

5.4.5 e) CH_2O

After two triatomic molecules we increase the dimensionality, moving toward a tetratomic one, formaldehyde. For this system we propagate classical trajectories under the potential energy surface of Martin *et al* for 30000 atomic units.[86] When the pre-exponential fac-

Table 5.5: The same as in Table (5.4) but for CO_2.

State	Exact[85]	SC-IVR	Kay's method	Regularization	Adiabatic	Johnson	PPs	HO	$\mathbf{R}_t^{(1)}$	$\mathbf{R}_t^{(2)}$	$\mathbf{R}_t^{(3)}$
(000)	2536.15	2535	2535	2536	2531	2534	2539	2564	2541	2534	2534
(01^10)	667.47	667	667	665	669	666	673	672	670	666	666
(01^10)	667.47	667	667	666	669	666	673	672	670	666	666
(10^00)	1285.1	1290	1288	1288	1275	1290	1299	1297	1294	1286	1291
(02^20)	1335.95	1333	1332	1332	1335	1334	1350	1351	1341	1334	1334
(02^20)	1335.95	1333	1332	1334	1335	1334	1350	1351	1341	1334	1334
(02^20)	1387.93	1388	1384	1386	1400	1383	1382	1393	1391	1382	1374
(11^10)	1929.56	1930	1928	1928	1923	1933	1947	1940	1940	1931	1931
(11^10)	1929.56	1930	1928	1929	1923	1933	1947	1940	1940	1931	1931
(03^30)	2005.25	1997	2001	2001	2015	2003	2021	2021	2012	2003	2003
(03^30)	2005.25	1997	2001	2001	2015	2003	2021	2021	2012	2003	2003
(03^10)	2078.15	2081	2080	2077	2093	2070	2083	2086	2084	2071	2071
(03^11)	2078.15	2081	2080	2079	2093	2070	2083	2084	2084	2071	2071
(00^01)	2349.38	2356	2355	2354	2347	2356	2371	2373	2359	2356	2354
MAE		3.0	2.7	2.1	6.9	3.8	11.4	12.4	6.3	3.2	3.9

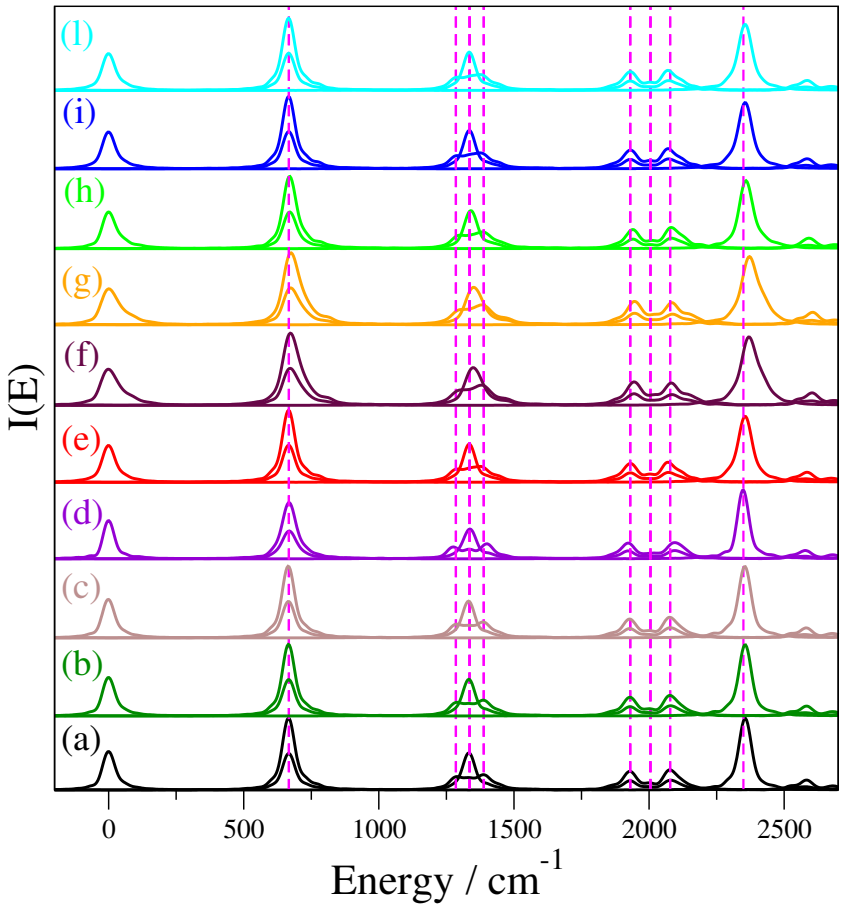

Figure 5.4.6: The same as in Fig.(5.4.5) but for the CO_2 molecule. Each approximation includes the spectra of the A_g, B_{1u}, B_{2u} and B_{3u} irreducible representations of the D_{2h} point group symmetry.

Table 5.6: The same as in Table (5.4) but for the fundamentals of CH_2O.

simmetry	Ex.[87]	SC-IVR	Kay's method	Regularization	Adiabatic	Johnson	PPs	HO	$\mathbf{R}_t^{(1)}$	$\mathbf{R}_t^{(2)}$	$\mathbf{R}_t^{(3)}$
ZPE (A_1)		5774	5774	5780	5744	5744	5932	6112	5819	5744	5744
B_1 (1_1)	1171	1162	1162	1169	1160	1159	1000	1004	1159	1160	1158
B_2 (2_1)	1253	1245	1246	1248	1240	1240	1164	1168	1253	1240	1240
A_1 (3_1)	1509	1509	1506	1513	1501	1509	1573	1575	1516	1509	1506
A_1 (4_1)	1750	1747	1745	1752	1737	1743	1745	1743	1745	1745	1740
A_1 (5_1)	2783	2810	2810	2785	2745	2747	2708	2711	2799	2750	2741
B_2 (6_1)	2842	2850	2846	2836		2801	2862	2741	2846	2807	2800

tor is not approximated we sample 24000 classical trajectories, otherwise 8000. Because of the presence of light atoms, the dynamics is strongly coupled and it results into a very high number of discarted trajectories, 82.5% by using Eq. (3.2.9) with $\varepsilon = 10^{-5}$, and 85.6% employing the method of Kay (Eq. (3.2.8)) with $D_t = 24000$. The complex motion also affects the number of regularized trajectories when one invokes the Monodromy matrix regularization of Eq. (5.3.25); for thys system 20.1% of trajectories undergoes at least one correction. TA-SCIVR results are very accurate both rejecting trajectories with Eq. (3.2.9) or (3.2.8). Nevertheless, when the pre-exponential factor is approximated using the monodromy matrix regularization, the accuracy does not get worse. The other approximations with the exception of the harmonic and PPs are quite accurate, offering Mean Absolute Errors between 20 and 30 wavenumbers. For this system, $\mathbf{R}_t^{(1)}$ performs very well, with an accuracy comparable with the reference one, suggesting that an anharmonic correction to the harmonic pre-exponential factor is beneficial. This evidence can be also deduced by looking at the estimates obtained employing the harmonic or the Poor Person's approximations of the pre-exponential factor. Table (5.6) shows our computed fundamental energy levels while Table (5.7) the overtone excitations. Figure (5.4.7) instead reports the calculated spectra of the irriducible representations of the C_{2v} point group of the molecule.

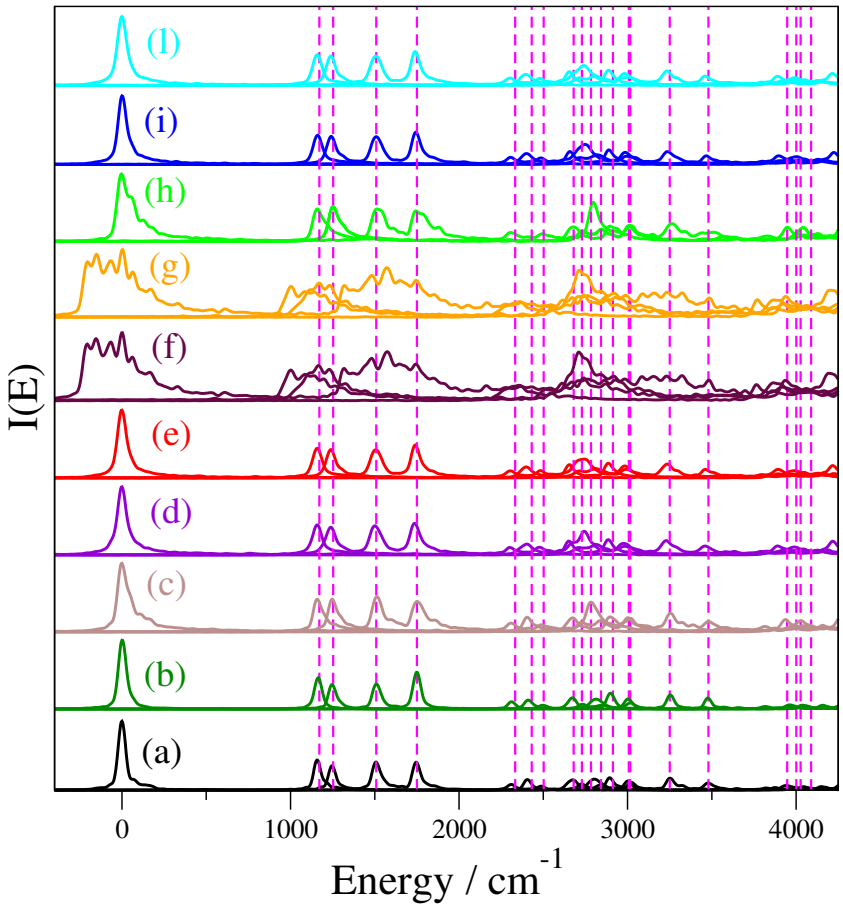

Figure 5.4.7: The same as in Fig.(5.4.5) but for the CH_2O molecule. Each approximation includes the spectra of the A_1, A_2, B_1 and B_2 irreducible representations of the C_{2v} point group symmetry.

Table 5.7: The same as in Table (5.4) but for the overtones of CH_2O. MAE is calculated over all values reported in Tables (5.6) and (5.7).

State	Exact[87]	SC-IVR	Kay's method	Regularization	Adiabatic	Johnson	PPs	HO	$\mathbf{R}_t^{(1)}$	$\mathbf{R}_t^{(2)}$	$\mathbf{R}_t^{(3)}$
$A_1\,(1_2)$	2333	2310	2310	2309	2302	2308	2163	2453	2307	2307	2304
$A_2\,(1_12_1)$	2431	2410	2408	2405	2403	2399	2356	2360	2408	2401	2396
$A_1\,(2_2)$	2502	2497	2494	2489	2477	2486		2712	2495	2486	2480
$B_1\,(1_13_1)$	2680	2672	2670	2675	2654	2656	2736		2679	2658	2654
$B_2\,(2_13_1)$	2729	2731	2730	2728	2800	2719	2762	2761	2734	2723	2716
$B_1\,(1_14_1)$	2913	2898	2896	2896	2886	2887	2871		2896	2888	2889
$B_2\,(2_14_1)$	3007	3002	3002	3002	2976	2986	2946		3010	2989	2983
$A_1\,(3_2)$	3016	3018	3014	3018	2986	2996	3086		3022	2993	3010
$A_1\,(3_14_1)$	3250	3254	3252	3256	3230	3240	3157		3263	3238	3234
$A_1\,(4_2)$	3480	3476	3475	3480	3462	3463	3323		3516	3468	3460
$B_1\,(1_15_1)$	3947	3957	3960	3937	3892	3897	3864	3868	3949	3897	3890
$A_2\,(1_16_1)$	4001	3979	3978	3974	3941	3942	3858	3864	3977	3945	3944
$B_2\,(2_15_1)$	4027	4056	4054	4029	3990	3994	3934	3938	4045	4010	3994
$A_1\,(2_16_1)$	4089	4038	4034	4043	4042	4053	4196		4074	4048	4048
$A_1\,(3_15_1)$	4266	4275	4273	4268	4218	4225	4481	4216	4281	4225	4216
MAE		12.8	13.1	9.9	31.9	25.2	91.1	91.9	12.1	23.4	30.2

5.4.6 f) CH_4

Finally, we now move toward methane molecule, for which an high coupled and choatic bahaviour of the nine vibrational degrees of freedom is expected. For TA-SCIVR calculation we sample 32000 classical trajectories when the pre-exponential factor is not approximated, while otherwise we run 14000 classical trajectories on the Potential Energy Surface of Lee *et al.*[88] Each classical trajectory is propagated for 30000 atomic units. When the pre-exponential factor is not approximated, the chaotic behaviour is enlighted by the very high rejection ratio, reaching 88.8% and 98.8% by employing the Monodromy and Kay criteria, respectively. Figure (5.4.8) shows our computed spectra of the irrducible representations of the T_d point group of the molecule. Table (5.8) instead reports the estimates at different levels of approximation, compared with exact values. Another time, both rejection criteria seem to provide comparable outcomes, and the monodromy matrix regularization comes to be high accurate. The other approximations, with the exception of the Poor Person's and harmonic ones, are very accurate and comparable

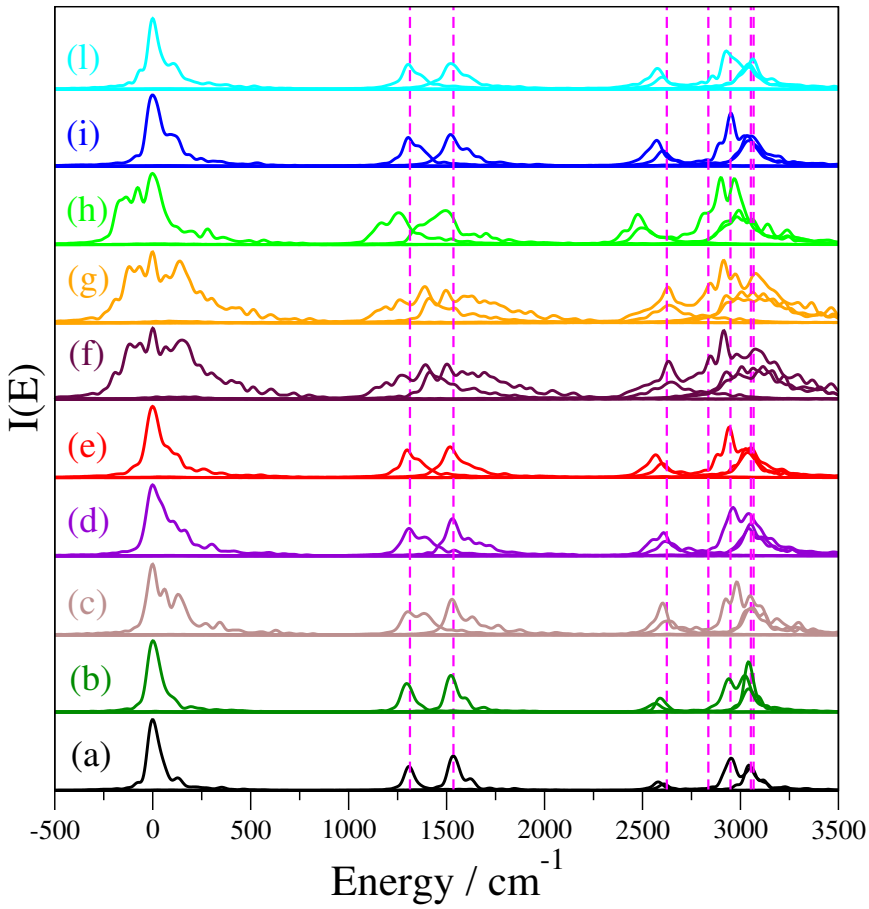

Figure 5.4.8: The same as in Fig.(5.4.5) but for the CH_4 molecule. Each approximation includes the spectra of the A_1, E, and T_2 irreducible representations of the T_d point group of symmetry.

Table 5.8: The same as in Table (5.4) but for CH_4.

State	Exact[58]	SC-IVR	Kay's method	Regularization	Adiabatic	Johnson	PPs	HO	$\mathbf{R}_t^{(1)}$	$\mathbf{R}_t^{(2)}$	$\mathbf{R}_t^{(3)}$
ZPE (A_1)	9707	9708	9708	9704	9669	9657	9846	10124	9941	9659	9652
T_2 (1_1)	1313	1296	1297	1304	1309	1300	1390	1390	1257	1305	1304
E (2_1)	1535	1524	1524	1528	1531	1518	1500	1497	1496	1522	1520
T_2 (1_2)	2624	2596	2593	2636	2616	2601	2646	2636	2497	2605	2600
T_2 ($1_1 2_1$)	2836	2820	2821	2832	1309	2818	2890	2887	2753	2827	2824
T_1 ($1_1 2_1$)	2836	2820	2821	2832	1309	2818	2890	2887	2753	2827	2824
A (3_1)	2949	2942	2942	2982	2963	2944	2914	2916	2936	2951	2928
E (2_2)	3067	3040	3042	3062	3052	3028	3065	3066	2993	3035	3044
T_2 (4_1)	3053	3038	3040	3052	3044	3037	3092	3069	2983	3041	3044
MAE		15.3	16.6	8.7	7.8	18.6	39.8	34.9	68.1	13.0	15.6

between each other, with a slight increasing level of accuracy increasing the iterative level of perturbation of the harmonic approximation.

5.5 Summary

The investigation of tailored bi-dimensional models and real molecular systems with increasing dimensionality provides a quite broad scenario to test the various pre-exponential factor approximations. First of all, we have observed that both rejection criteria provide very accurate and very similar results between each other. Moreover, Despite the scenario spans both from low to high dimensional and from low to extremely high chaotic systems, the different pre-exponential factor approximations seem to provide a sound of similar insights and allow us to draw some conclusions. In particular, the Monodromy matrix regularization, when feasible, is high accurate and very often provides estimates comparable with reference ones. Furthermore, the proposed iterative solutions $\mathbf{R}_t^{(2)}$ and $\mathbf{R}_t^{(3)}$ sometimes show a lower level of accuracy; however they are stable and do not undergo numerical issues, which can affect the Monodromy matrix regularization as the other approximations *e.g.* adiabatic and Johnson ones. In conclusion we suggest them as well as the Monodromy matrix regularization when possible. Despite the choice of the threshold is strongly dependending on the system, as a rule of thumb we have found that a reasonable choice for it can be $10^2 - 10^3$, leading to few regularizations along each trajectory.

Chapter 6

Divide-and-Conquer Semiclassical dynamics

The numerical blowing up of the pre-exponential factor is in general more probable to occur if the dimensionality of the system increases, and the application of standard SCIVR calculations to high dimensional systems is plagued by the increasing of rejection ratios and the consequent demand of available classical trajectories. The development of accurate and reliable pre-exponential factor approximations paves the way to the application of SCIVR to systems with many degrees of freedom, since rejection events can be tamed, and roughly a thousand of classical trajectories per degree of freedom are in principle necessary to obtain a spectroscopic signal. Moreover, if pre-exponential factor approximations are combined with the Multiple Coherent State approach, then ab-initio semiclassical dynamics becomes a reliable way to obtain a spectroscopic signal of systems made by more than few dozens of degrees of freedom, as was recently shown.[76] Nevertheless, Semiclassical method runs out of steam when the systems dimensionality increases to 25-30. To understand the reason behind it we have to go into to the physical interpretation of the autocorrelation function that is semiclassically approximated. The spectral density is calculated as the Fourier transform of $\left\langle \psi_t \middle| \psi_0 \right\rangle$, and the evolved wave-packed has to periodically recross close to the initial conditions to obtain a clear spectroscopic signal. This event is in general less and less probable if the dimensionality of the system increases, since the overlap has to occur at the same time for all the

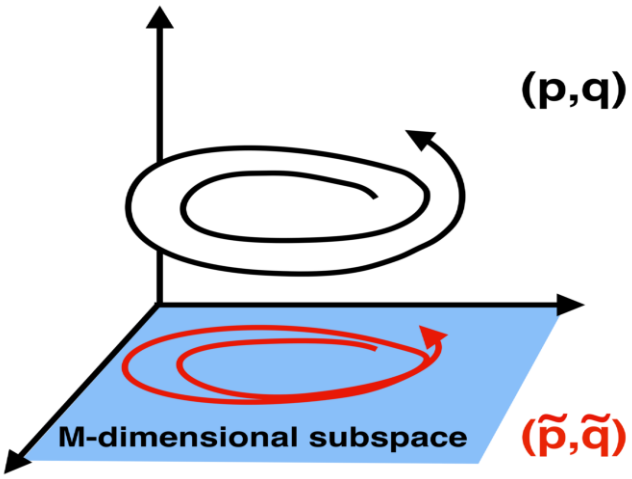

Figure 6.1.1: Pictorial representation of a full-dimensional trajectory (black line) and its projection (red line) onto a M-dimensional subspace.

dimensions. It is the semiclassical manifestation of the curse of dimensionality problem, a general stumbling block for any exact or approximated quantum method. As a direct consequence of it, semiclassical calculations on systems with more than 25-30 degrees of freedom are plagued, while the accuracy and appearing of the spectra are irreparably jeopardized, not allowing to recover a clear spectroscopic signal.

6.1 The idea

A way to overcome the problem is to help the wavepacket to recross close to the initial conditions by projecting it onto a reduced dimensional subspace. A pictorial representation that sketches the idea is reported in Figure (6.1.1), where the black line is the full-dimensional classical trajectory and the red line is its projection into a M-dimensional subspace. The dimensionality is in this way reduced, thus helping the appearing of a clear spectroscopic signal. This is the main idea at the basis of the Divide-and-Conquer semiclassical method that is discussed below in the text.[71] The method allows to recover vibrational spectra of high-dimensional systems as a combination of partial spectra, each one obtained upon projection of the full-dimensional problem onto a certain subspace.

The projection procedure is done only on semiclassical quantities, while the classical trajectory remains full-dimensional, retaining all the interactions between the degrees of freedom. In this way spectral features are hopefully expected to be close to the full-dimensional ones.

6.2 Subspace's spectral density

The Divide-and-Conquer working formula for power spectra can be obtained by working out the usual expression of Kaledin and Miller for a N_{vib} dimensional problem[64, 65]. Similarly to the full-dimensional case, the power spectrum of M-dimensional subspace is

$$\widetilde{I}(E) = \left(\frac{1}{2\pi\hbar}\right)^{M} \iint d\tilde{\mathbf{p}}(0)\, d\tilde{\mathbf{q}}(0)\, \frac{1}{2\pi\hbar T} \left| \int_0^T e^{\frac{i}{\hbar}\left[\tilde{S}_t(\tilde{\mathbf{p}}(0),\tilde{\mathbf{q}}(0))+Et+\tilde{\phi}_t\right]} \langle \tilde{\boldsymbol{\chi}} | \tilde{\mathbf{p}}(t), \tilde{\mathbf{q}}(t)\rangle dt \right|^2 . \tag{6.2.1}$$

We observe that in the case of $M = N_{vib}$ Eq. (6.2.1) regains Eq. (4.2.1). The integral is done now in the reduced M-dimensional $(\tilde{\mathbf{p}}, \tilde{\mathbf{q}})$ phase space, and $(\tilde{\mathbf{p}}, \tilde{\mathbf{q}})$ are the projected position and momenta vectors. $\langle \tilde{\boldsymbol{x}} | \tilde{\mathbf{p}}(t), \tilde{\mathbf{q}}(t)\rangle$ are projected coherent states, $\tilde{\phi}_t$ is the phase of the pre-exponential factor, where only each monodromy matrix block is of the type $\partial \tilde{\boldsymbol{i}}(t) / \partial \tilde{\boldsymbol{j}}(0)$ with $\tilde{\boldsymbol{i}}, \tilde{\boldsymbol{j}}$ that can be $\tilde{\mathbf{p}}$ or $\tilde{\mathbf{q}}$. Finally $\tilde{S}_t(\tilde{\mathbf{p}}(0), \tilde{\mathbf{q}}(0))$ is the projected action functional. To obtain Eq. (6.2.1) from Eq. (4.2.1) we need to find a way to calculate the mentioned projected quantities from the full-dimensional ones. The easiest part are the coherent states since the full-dimensional ones are defined as a direct product of monodimensional terms *i.e.*

$$\left\langle \mathbf{x} \middle| \mathbf{pq} \right\rangle = \left\langle x_1 \middle| p_1 q_1 \right\rangle \left\langle x_2 \middle| p_2 q_2 \right\rangle \ldots \left\langle x_{N_{vib}-1} \middle| p_{N_{vib}-1} q_{N_{vib}-1} \right\rangle \left\langle x_{N_{vib}} \middle| p_{N_{vib}} q_{N_{vib}} \right\rangle . \tag{6.2.2}$$

The M-dimensional coherent state will be

$$\left\langle \tilde{\mathbf{x}} \middle| \tilde{\mathbf{p}}\tilde{\mathbf{q}} \right\rangle = \prod_{i=1}^{M} \left\langle x_i \middle| p_i q_i \right\rangle , \tag{6.2.3}$$

where $\{p_i\}_{i=1,M}$ and $\{q_i\}_{i=1,M}$ are the sets of degrees of freedom enrolled in the subspace. The projection of coherent states does not introduce any approximation since it can be done exactly. On the opposite, when either the pre-exponential factor or the action are projected, an approximation is introduced, since in general they contain interaction terms. The required matrices and vectors can be obtained by a preliminary suitable singular value decomposition (SVD),[89] followed by a subsequent matrix multiplication between the full-dimensional quantity and the projector. We define a displacement matrix $\mathbf{D}$ for the M-dimensional subspace similarly to other works.[89, 74] $\mathbf{D}$ is a $\mathrm{N_{vib}} \times \mathrm{M}$ dimensional matrix and a decomposition of it is $\mathbf{D} = \mathbf{U\Sigma V}$, where Σ is the $\mathrm{M} \times \mathrm{M}$ eigenvalues matrix, $\mathbf{V}$ is $\mathrm{M} \times \mathrm{M}$ and $\mathbf{U}$ is $\mathrm{N_{vib}} \times \mathrm{M}$. The projector Δ is defined as $\Delta = \mathbf{U}\mathbf{U}^T$. Now each projected matrix $\tilde{\mathbf{A}}$ can be obtained as $\tilde{\mathbf{A}} = \mathbf{\Delta A \Delta}$ by retaining the $\mathrm{M} \times \mathrm{M}$ subblock different from zero. Similarly any vector $\tilde{\mathbf{q}}$ will be calculated as $\tilde{\mathbf{q}} = \mathbf{\Delta q}$. The last term to be projected is the action. It is calculated from the Lagrangian functional, that can be projected itself by a proper work out of its kinetic and potential terms.

$$\tilde{S}_t\left(\tilde{\mathbf{p}}\left(0\right), \tilde{\mathbf{q}}\left(0\right)\right) = \int_0^T \left[\frac{1}{2} m \dot{\tilde{\mathbf{q}}}^2\left(t\right) + V_S\left(\tilde{\boldsymbol{q}}\left(t\right)\right)\right] dt \tag{6.2.4}$$

The kinetic part is trivial since it is separable, while in general the expression for $V_S\left(\tilde{\boldsymbol{q}}\left(t\right)\right)$ is unknown. It describes the potential leading to a set of positions and momenta $(\tilde{\mathbf{p}}, \tilde{\mathbf{q}})$ equal to the projection of the full-dimensional trajectory $(\mathbf{p}, \mathbf{q})$. We extract a general expression of $V_S\left(\tilde{\boldsymbol{q}}\left(t\right)\right)$ by defining it as the full-dimensional potential functional, where at each frame, the coordinates belonging to the subspace are left unchanged while the remaining ones are set at the equilibrium. Such potential is

$$V_S\left(\tilde{\mathbf{q}}\left(t\right)\right) \equiv V\left(\tilde{\mathbf{q}}\left(t\right); \mathbf{q}^{eq}_{N_{vib}-M}\left(t\right)\right). \tag{6.2.5}$$

Unfortunately a so-defined potential would not account for interactions of the degrees of freedom with the sorrounding. To regain the correct behavior we can introduce a field

$\lambda(t)$, defined as

$$\lambda(t) = V(\tilde{\mathbf{q}}(t); \mathbf{q}_{N_{vib}-M}(t)) - \left[V\left(\tilde{\mathbf{q}}(t); \mathbf{q}^{eq}_{N_{vib}-M}\right) + V(\mathbf{q}^{eq}_{M}; \mathbf{q}_{N_{vib}-M}(t))\right], \quad (6.2.6)$$

which is exact in the limit of a separable potential.

$$V_S(\tilde{\mathbf{q}}(t)) \equiv V\left(\tilde{\mathbf{q}}(t); \mathbf{q}^{eq}_{N_{vib}-M}(t)\right) + \lambda(t). \quad (6.2.7)$$

Subspace are selected in order to collect together the mostly interacting degrees of freedom, and leaving out from each subspace the remaining ones. Interacting modes can be found by looking at the off-diagonal terms of a time-averaged hessian matrix $\tilde{\mathbf{H}}$ along a test trajectory. In our simulations we use as test trajectory, the central one, *i.e.* starting from $(\mathbf{q}_{eq}, \mathbf{p}_{eq})$. The basic idea behind it is that, if two degrees of freedom are not coupled, then the corresponding hessian off-diagonal term should be equal to zero. On the opposite, high values (in modulos) of the off-diagonal term suggests a strong interaction between modes. We then set an arbitrary threshold paramenter ε, and we look for combinations of modes that have $H_{ij} \geq \varepsilon$. The threshold is chosen to have subspaces dimensions as high as possible, but compatible with semiclassical calculations. A more detailed description of the procedure is reported in Section (7.1).

6.3 Proofs of concept

6.3.1 a) Three uncoupled Morse oscillators

As a first step, we test DC SCIVR against a model potential made by three uncoupled Morse oscillators. We remind that in this case, the method should be exact and it has to provide the same full-dimensional SCIVR values, that we use to benchmark the method. The potential is

$$V(q_1, q_2, q_3) = D \sum_{i=1}^{3} \left[1 - e^{-\alpha_i\left(q_i - q_i^{eq}\right)}\right]^2 \quad (6.3.1)$$

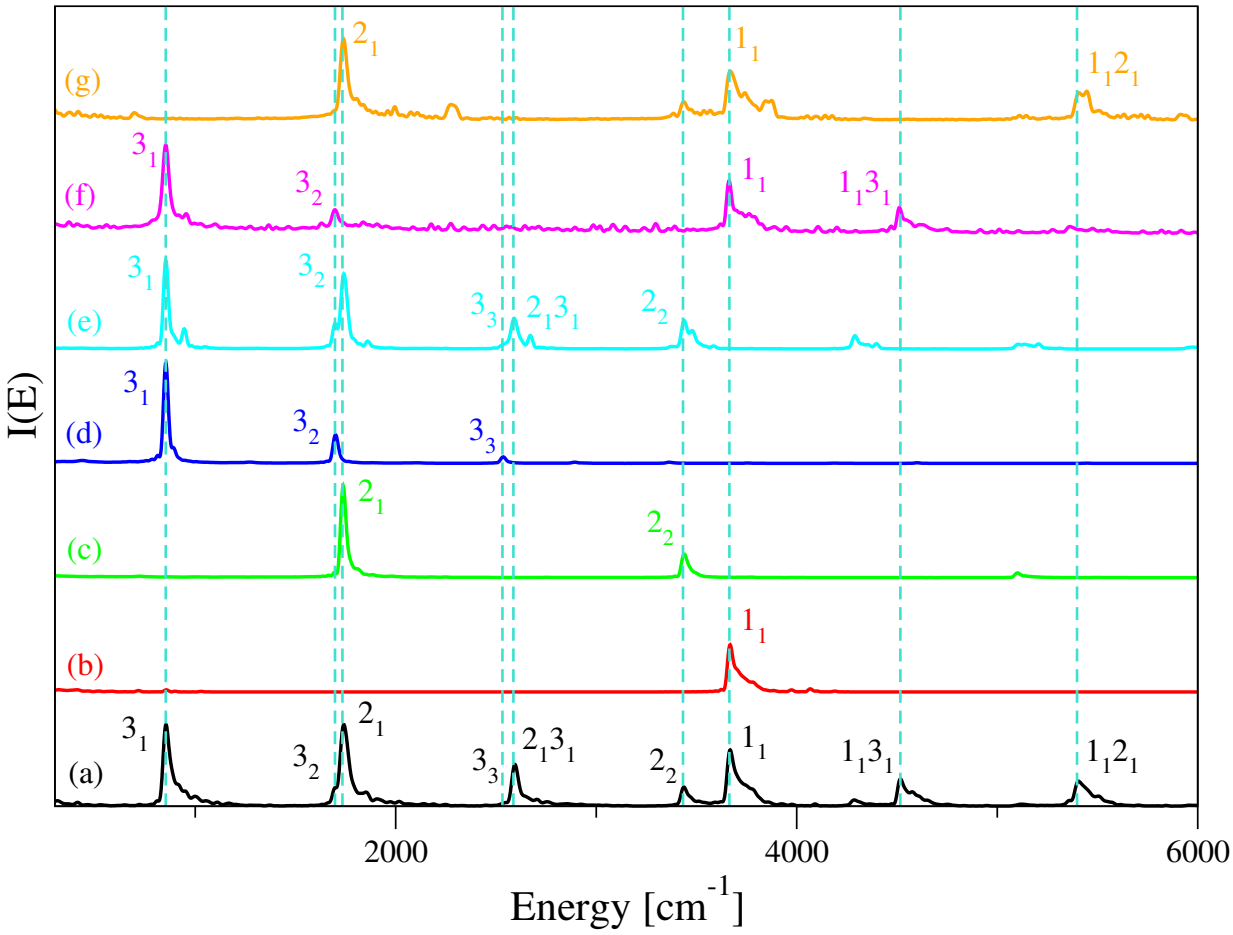

Figure 6.3.1: DC-SCIVR spectra for the Morse oscillators of Eq. (6.3.1). (a) black line for the full dimensional TA-SCIVR spectrum; (b) red line for the DC-SCIVR spectrum of mode 1; (c) green line, the same of (b) for mode 2; (d) blue line, the same of (b) for mode 3; (e) cyan line, DC-SCIVR for the subspace composed by mode 2 and 3; (f) magenta line, the same as (e) but for modes 1 e 3; (g) yellow line, the same as (e) but for modes 1 and 2. Vertical dashed turquoise lines indicates the exact values.

where the dissociation energy $D = 0.2\ a.u.$ is the same for the three oscillators, and $\alpha_i = \omega_i\sqrt{\mu/2D}$. The reduced mass is that one of the H_2 molecule, *i.e.* $\mu = 918.975\ a.u.$, and the frequencies are 3832, 1770, and 861 wavenumbers. We sample the phase space $(\tilde{\mathbf{p}}(t), \tilde{\mathbf{q}}(t))$ trajectories according to the Husimi distribution using a Box-Muller sampling centered at $\tilde{\mathbf{q}}^{eq} = (0,0,0)$ and $\tilde{\mathbf{p}}^{eq} = \left(\sqrt{\omega_1}, ..., \sqrt{\omega_M}\right)$, where $\tilde{\mathbf{p}}^{eq}$ has been taken at the ZPE value. The reference state $|\chi\rangle = \prod_i^M \left|\sqrt{\omega_i}, q_i^{eq}\right\rangle$ is defined for each M-dimensional subspace. We perform 10000 trajectories per each subspace and each trajectory is 50000 a.u. time long. The results are reported in Fig.(6.3.1) where all possible

space subdivisions for the three dimensional space are considered. More specifically, the bottom spectrum is the full dimensional TA-SCIVR calculation, *i.e.* without any space subdivision. The other spectra are reporting the partial power spectra $\tilde{I}(E)$ of the subspace subdivision. The one-dimensional for mode 1 is the red line, the same for mode 2 in green and for mode 3 in blue. The cyan line spectrum is for a subspace composed of modes 3 and 2, the magenta one for modes 1 and 3, and the orange one for modes 1 and 2. In all cases the agreement with the full dimensional one is very strict. The ZPE obtained by composition of the partial spectra $\tilde{I}(E)$ is $3212\,cm^{-1}$, which is the same as the full dimensional TA-SCIVR ZPE value and to compared with the exact one $3205\,cm^{-1}$. This is a confirmation that the DC SCIVR method is exact, *i.e.* the same as TA-SCIVR, for separable systems. Moreover, Fig.(6.3.1) shows that the power of the divide and conquer approach can not only accelerate the Monte Carlo integration by virtue of the reduced dimensionality of each subspace and get better resolved spectra, but also help to identify each peak.

6.3.2 b) Two coupled Morse oscillators

We now move toward a non-separable potential. The potential is made by two strongly coupled Morse oscillators. The high level of coupling between the degrees of freedom can be evinced from the high rejection ratio of the classical trajectories reported below, and from the deviation of the exact energy levels from the uncoupled ones. The Morse oscillators have harmonic frequencies equal to 3000 and 1700 wavenumbers, and the same dissociation energy equal to $D = 0.2$. The potential is expressed as

$$V(q_1, q_2, q_3) = D \sum_{i=1}^{2} \left[1 - e^{-\alpha_i \left(q_i - q_i^{eq}\right)}\right]^2 + c\,(q_1 - q_1^{eq})^2\,(q_2 - q_2^{eq})^2\,, \qquad (6.3.2)$$

and c is the coupling constant set equal to $c = 10^{-7}\mu^2$ in our calculations. The equilibrium coordinates are set equal to $q_1^{eq} = q_2^{eq} = 0$. For the full-dimensional SCIVR simulation

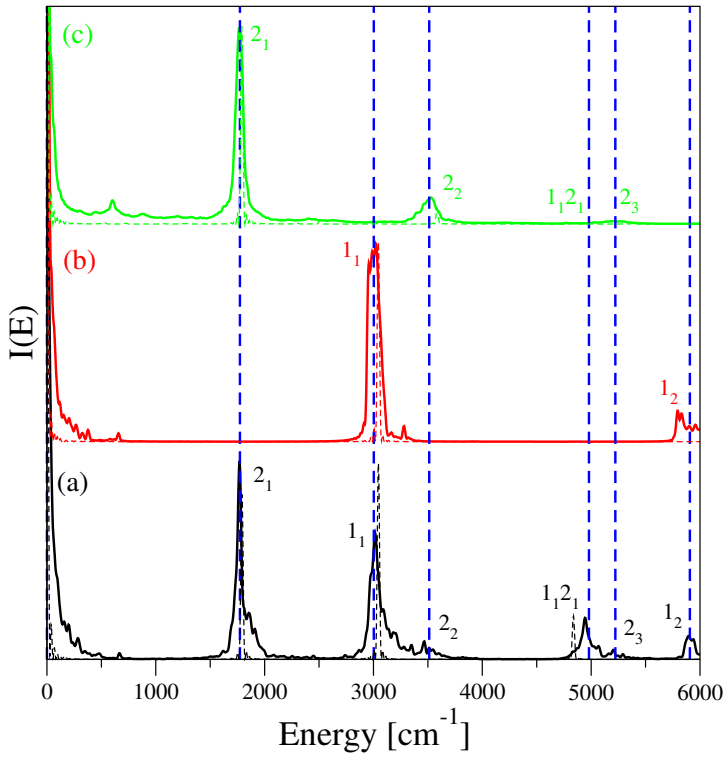

Figure 6.3.2: DC-SCIVR spectra for the Morse oscillators of Eq. (6.3.2). Dashed lines are for the MC-SCIVR simulations (single trajectories) and continuous ones for 10000-trajectory simulations. (a) black line for the full-dimensional TA-SCIVR spectrum; (b) red line for the DC-SCIVR spectrum of mode 1; (c) green line, the same of (b) for mode 2. Vertical dashed blue lines indicate the exact values calculated by a Discrete Variable Representation (DVR) approach.[13]

we sample 10000 classical trajectories while for DCSCIVR spectra 10000 trajectories are sampled for each subspace. Furthermore, we also perform single-trajectory simulations by tailoring the reference state according with Eq. (4.3.2). In the case of SCIVR simulation the high rejection ratio 39% bear the high deviation from a separable problem. Figure (6.3.2) reports the computed spectra, and we can observe that the two fundamental excitations are very well detected as well as the first overtones, while the first significant deviations from SCIVR energy levels appear for the high energetic overtones above 5000 wavenumbers.

Table 6.1: Vibrational energy levels of water. The first and second columns show the vibrational state label and the exact results respectively; the third column reports the full-dimensional TA-SCIVR eigenvalues. Column four shows the DC-SCIVR results with the Hessian matrix criterion (DC SCIVR$_{\text{Hess}}$). The last column reports the harmonic estimates. All values are in cm^{-1}. MAE stands for Mean Absolute Error and it is calculated with respect to the exact values,[96] and for DC-SCIVR simulations also with respect to the full-dimensional TA-SCIVR values.

Mode	Exact[96]	TA SCIVR	DC SCIVR$_{\text{Hess}}$	HO
1_1	1595	1580	1581	1649
1_2	3152	3136	3154	3298
2_1	3657	3664	3656	3833
3_1	3756	3760	3824	3944
MAE Exact		11	21	141
MAE SCIVR			23	

6.3.3 c) H_2O

We now do a step forward with respect to the previous subsections, by moving our attention onto a realistic system as the water molecule. To do that we employ a Potential Energy Surface (PES) for which exact energy levels are available; we use the Purtridge and Schwenke PES,[90] recently used as one-body term is the new generation of water Potential Energy Surfaces of Bowman's group.[91, 60, 92, 93, 94, 95] We also perform full-dimensional SCIVR calculation as a further benchmark for our DCSCIVR method. We run 4000 trajectories per subspace in the case of DC SCIVR simulations, while 12000 in the case of full-dimensional SCIVR. The analysis of the off-diagonal terms of the time-averaged Hessian matrix suggests that the symmetric bending and stretching modes have to be separated from mode 3, the asymmetric stretching. Table (6.1) reports our DC SCIVR estimates, compared with SCIVR results and exact energy levels. First of all, the method accounts also for the high anharmonicity of the system, as can be evinced by the low average deviation from exact levels equal to 20 cm^{-1} to be compared with 140 cm^{-1} for the normal mode analysis. Moreover, despite the high level of inter-mode coupling, DC SCIVR estimates are very well in agreement both with SCIVR and exact levels. These results, even if combined with the previous ones on Morse oscillators, provides a remark-

able milestone for the reliability of our method, since excitations were found to be very accurate even if the degrees of freedom are highly coupled. Below in the text we test the method against an extremely chaotic potential, and then we will increase the dimensionality proving the final goal of the method: the applicability of semiclassical spectroscopy calculations for high-dimensional systems.

6.3.4 d) CH_4

Methane molecule represents a quite challenging system for testing our new method. It is made by nine vibrational degrees of freedom whose dynamics undergo a very high caothic behavior due to the presence of many interacting light atoms such as hydrogens. For full-dimensional SCIVR simulations we have to run 180000 classical trajectories because 95% of them are rejected using the criterion $1 - \det \left| \mathbf{M}^T(t)\, \mathbf{M}(t) \right| > 10^{-5}$. In the case of DC SCIVR simulations we run 20000 classical trajectories for each degree of freedom in order to have the same total number as for SCIVR. We use the Potential Energy Surface of Carter *et al*, for which exact eigenvalues are available.[58] According with the Hessian partitioning method the nine vibrational modes are grouped into a six-dimensional and a three-dimensional subspaces.

Figure (6.3.3) reports our computed spectra, while Table (6.2) contains our DC SCIVR estimates compared with full-dimensional SCIVR and exact levels. By looking at Figure (6.3.3) we can deduce that the method recovers both fundamental and overtones excitations accurately, and the partitioning also helps into the interpretation and the assignment of peaks very close in energy. It can happen that some excitations appear in both spectra because of the symmetry, since some degenerate modes are collected in the six-dimensional subspaces and the remaining in the three-dimensional one. By looking at Table (6.2) instead we can observe that DC SCIVR estimates are very accurate as well as full-dimensional SCIVR ones when compared with exact eigenvalues. The mean absolute deviation is very tiny (11 cm^{-1}). This example once again suggests that the divide-and-

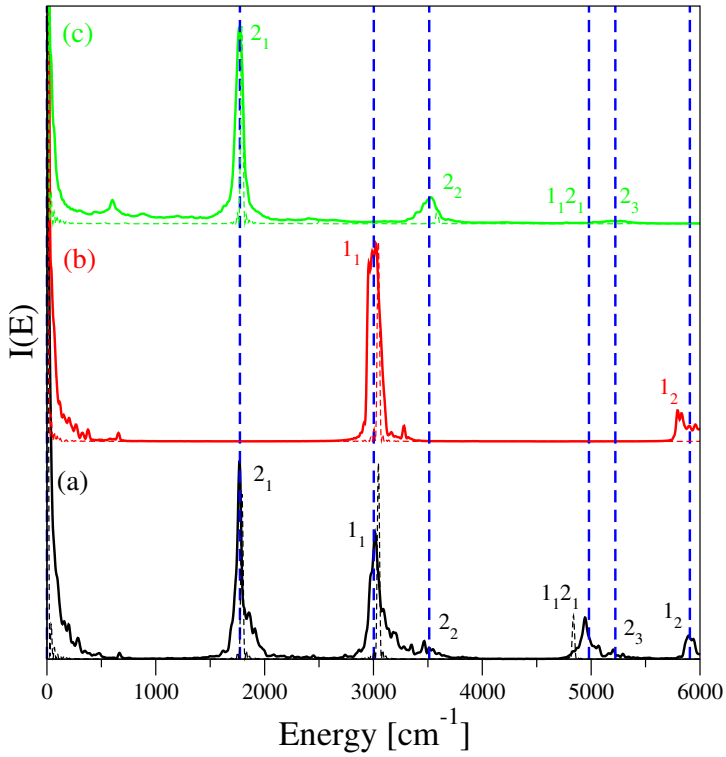

Figure 6.3.3: DC-SCIVR spectra for the methane. Starting from the bottm (a) black line for the spectrum of a six-dimensional subspace; (b) red line for the of a three-dimensional one; Vertical dashed blue lines indicate the full-dimensional SCIVR values calculated using Eq. (4.2.1).

Table 6.2: Vibrational frequencies of CH_4. "QM" labels the exact quantum eigenvalues; "SCIVR" refers to a full dimensional semiclassical calculation; "DC-SCIVR" labels frequencies obtained with the "divide-and-conquer" approach here presented; "HO" are harmonic estimates. All values are in cm^{-1}.

State	QM[58]	SCIVR	DC-SCIVR	HO
1_1	1313	1300	1300	1345
2_1	1535	1529	1532	1570
1_2	2624	2594	2606	2690
$1_1 2_1$	2836	2825	2834	2915
3_1	2949	2948	2964	3036
2_2	3067	3048	3050	3140
4_1	3053	3048	3044	3157
MAE		12	11	68

conquer method can accurately detect energy levels with good accuracy.

After these three proofs-of-principle we now test the method against molecular systems for which full-dimensional SCIVR can not be afforded. In the first example we calculate the vibrational excitations of Benzene, comparing them with exact calculations of Halverson and Poirier,[14] and then we move on a C_{60} model potential for which exact results are not available.

6.4 Application to Benzene

After testing the method against different model potentials and real molecular systems for which full-dimensional SCIVR calculations are doable, we now attempt to calculate the vibrational eigenvalues of benzene, for which full-dimensional calculations are out of reach.

Benzene is made by twelves atoms, and consequently by 30 vibrational degrees of freedom. At the best of our knowledge it is also the highest dimensional molecular system for which exact vibrational levels are available. They were recently computed by Halverson and Poirier[14] employing the Potential Energy Surface of Handy.[97] In this work we use the same PES for comparison. The chaotic behaviour of the classical trajectories and the consequent rejection events are tamed by using the second order iterative approximation to the pre-exponential factor reported in Eq. (5.3.16). In this way, 1000 classical trajectories per degree of freedom are propagated for 30000 atomic units, which represents a typical dynamics lenght for semiclassical calculations. Thus, the total number of propagated trajectories is equal to 30000. $(\mathbf{q}_{eq}, \mathbf{p}_{eq})$ of the reference state $\left|\chi\right\rangle$ are chosen as usual. $\mathbf{q}_{eq}$ are the equilibrium coordinates, while $\mathbf{p}_{eq}$ are obtained by distributing energy according to the harmonic frequencies, and in order to have a total energy equal to 95% of the harmonic ZPE. The test trajectory for the Hessian method is propagated starting from $(\mathbf{q}_{eq}, \mathbf{p}_{eq})$. The vibrational space is separated into one eigth-dimensional,

Table 6.3: Vibrational fundamental excitations of benzene. Columns "DC-SCIVR" indicates our estimates, while columns "EQD" reports available quantum results. Degenerate frequencies are not replicated. Values are in cm^{-1}.

State	DC-SCIVR	EQD[14]	State	DC-SCIVR	EQD[14]
1_1	388	399.455	10_1	1024	1040.980
2_1	610	611.428	11_1	1157	1147.751
3_1	732	666.929	12_1	1157	1180.374
4_1	706	710.732	13_1	1295	1315.612
5_1	908	868.911	14_1	1357	1352.563
6_1	990	964.013	15_1	1460	1496.231
7_1	996	985.829	16_1	1606	1614.455
8_1	996	997.624	MAE	19	
9_1	1018	1015.64			

8 bi-dimensional, and 6 mono-dimensional subspaces. The computed energy levels are compared with exact ones in Table (6.3). Remarkably, the overall accuracy of DC SCIVR estimates is within the typical semiclassical range with only one mode slightly off-the mark, and the MAE is for this system equal to 19 wavenumbers.

6.5 Application to Fullerene model

After benchmarking the method, we now move our attention on an high dimensional system to show that DC SCIVR can provide clear spectral signals, even when the dimensionality becomes very large and exact calculations are not doable. For this purpose we calculate vibrational excitations of a Fullerene-like system. It presents 60 atoms and consequently 174 vibrational degrees of freedom. Nuclei are moved under a pre-existing force field obtained at a DFT level of theory and originally used for graphene. This potential accounts for stretching, bending, and torsional contributions, but neglects bond-coupling terms and van der Waals interactions.[98] Actually, it is not designed for quantitately describing fullerenes. However, in this section our goal is to show that in the presence of an available Potential Energy Surface or some ab-initio potential, clear spectral signals can be exctracted, overcoming in this way the curse of dimensionality. Moreover, the

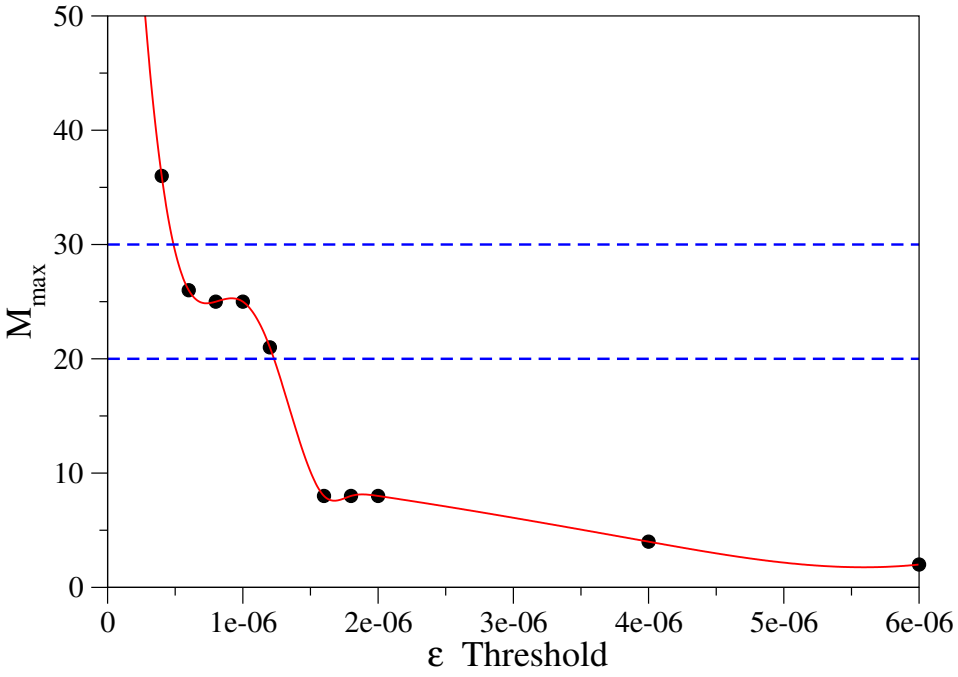

Figure 6.5.1: Trend of Maximum subspace dimensionality (M_{max}) against the threshold ε for the C_{60} calculation. The red curve fits the overall behavior, while the dashed blue lines sorround desirable (M_{max}) values.

benchmark calculations reported above suggest that in the presence of a suitable potential, outcoming DC-SCIVR vibrational frequencies are quite accurate, sometimes as well as standard SCIVR calculations, and in general only few wavenumbers worse.

To start-off, the 174-dimensional vibrational degrees of freedom are separated in subspaces according with the Hessian criterion. Figure (6.5.1) shows how the maximum subspace dimension (M_{max}) depends from the threshold parameter. In particular, a value of ε equal to 10^{-6} leads to (M_{max})=25, a good trade-off between accuracy and feasibility. The vibrational modes are grouped into a 25-dimensional, two 14-dimensional, two 8-dimensional, a 6-dimensional, three tri-dimensional, one bi-dimensional, and 90 mono-dimensional subspaces. Because of the high number of dimensions (174), we employ the multiple coherent state approach by running 175 classical trajectories propagated for 50000 atomic units, and tailoring the reference state of the semiclassical propagator according with Eq. (4.3.2). Figures (6.5.2) and (6.5.3) show the partial spectra of a tri-dimensional and a bi-dimensional subspaces, while Table (6.4) reports the computed

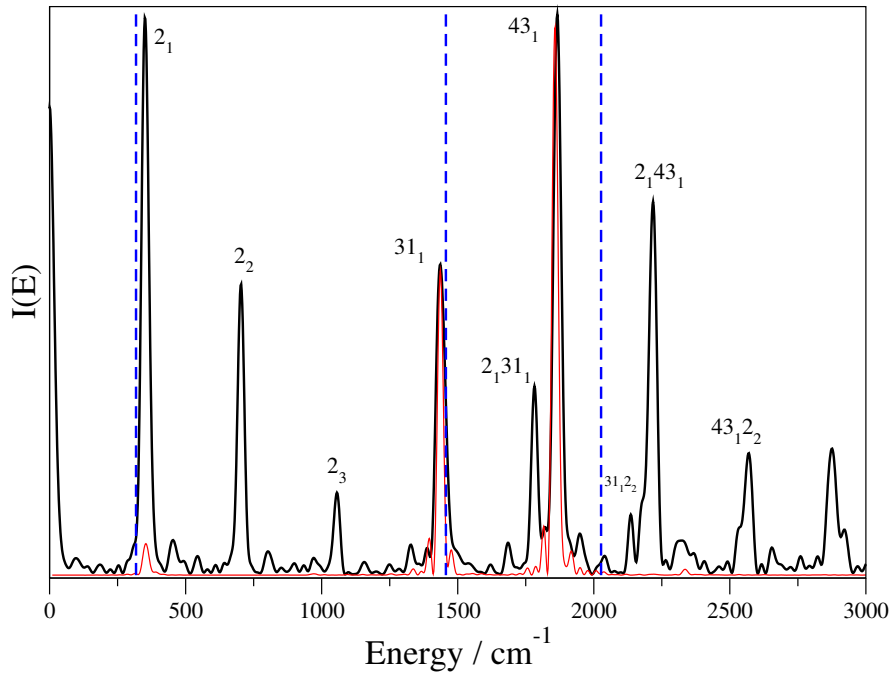

Figure 6.5.2: Partial spectrum of a tri-dimensional subspace of C_{60}. Black line is for DC-SCIVR, while red line is the classical spectrum obtained as Fourier transform of the velocity-velocity correlation function. Harmonic frequencies are reported in dashed blue lines. The label of the excitations is the same of Table (6.4).

energy levels up to 1600 wavenumbers. The first conclusion we can draw is that C_{60} can be with good approximation assumed as a classical object. However, many spectral

Table 6.4: Vibrational frequencies of the C_{60} model up to 1600 cm^{-1}. "HO" column indicates harmonic values; "Cl" labels the classical estimates of fundamental frequencies; "DC-SCIVR" introduces our semiclassical results. Values are in cm^{-1}.

State	HO	Cl	DC-SCIVR	St.	HO	Cl	DC-SCIVR	St.	HO	Cl	DC-SCIVR	St.	HO	Cl	DC-SCIVR
1_1	255	254	254	2_2	636		706	20_1	905	880	880	11_2	1202		1150
2_1	318	355	352	12_1	648	630	626	21_1	962	971	971	27_1	1225	1218	1218
3_1	359	347	346	13_1	657	652	651	6_2	968		966	28_1	1252	1231	1231
4_1	404	432	432	3_2	718		693	7_2	976		1093	12_2	1296		1254
5_1	404	404	403	14_1	770	767	767	8_2	988		957	29_1	1310	1269	1264
6_1	484	483	483	15_1	775	766	766	22_1	1000	997	998	13_2	1314		1303
7_1	488	547	547	16_1	781	777	777	23_1	1014	1015	1015	31_1	1457	1438	1434
8_1	494	478	478	4_2	808		863	24_1	1042	1039	1037	32_1	1470	1398	1391
1_2	510		506	5_2	808		807	25_1	1052	1075	1075	33_1	1526	1467	1506
9_1	546	545	546	17_1	816	779	774	26_1	1091	1062	1060	14_2	1540		1534
10_1	568	611	610	18_1	863	872	872	9_2	1092		1091	15_2	1550		1533
11_1	601	571	572	19_1	890	911	911	10_2	1136		1220	16_2	1562		1554

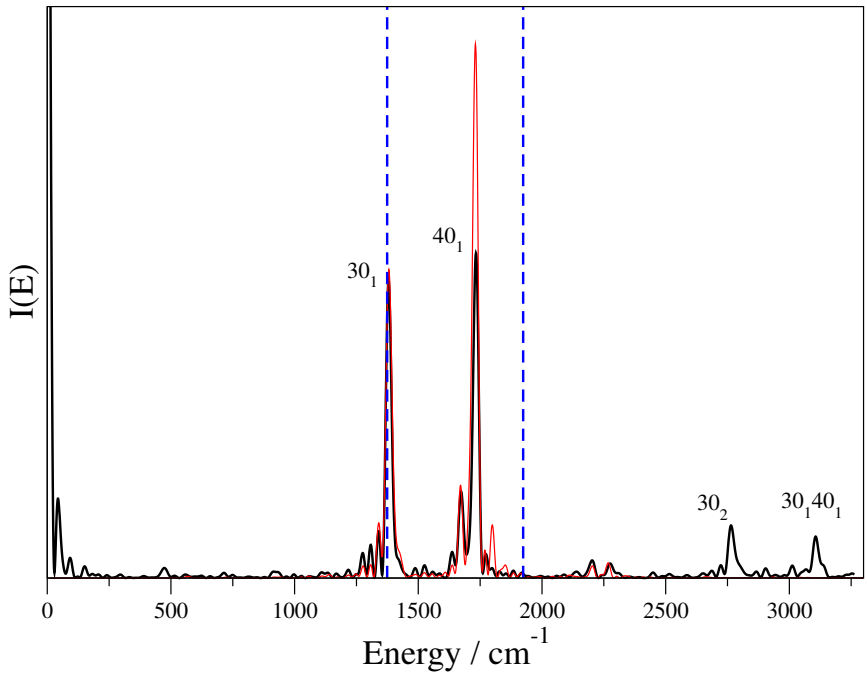

Figure 6.5.3: Partial spectrum of a bi-dimensional subspace of C_{60}. Black line is for DC-SCIVR, while red line is the classical spectrum obtained as Fourier transform of the velocity-velocity correlation function. Harmonic frequencies are reported in dashed blue lines. The label of the excitations is the same of Table (6.4).

features as overtones, are neglected by a classical simulations, and a complete description of the molecule is possible only by means of a quantum mechanical approach. Despite the high symmetry of the system, we want to point out that DC SCIVR does not take advantage of symmetry constraints, since it is based on propagation of full dimensional classical trajectories. As a further proof about it, we isotopically substitute 3 carbon atoms imposing to have the mass of gold; we call this isotopic model C_{60}^*. In this way all the symmetry is removed and consequently the degeneracies of the vibrational excitations. Figure (6.5.4) shows the partial spectra of subspaces containing five modes that should be degenerate in C_{60}, while in C_{60}^* they should show a splitting. According with the harmonic estimates (vertical dashed lines) the DC SCIVR spectrum shows a double peak in the tailored model, while a single peak is observed in the case of C_{60}.

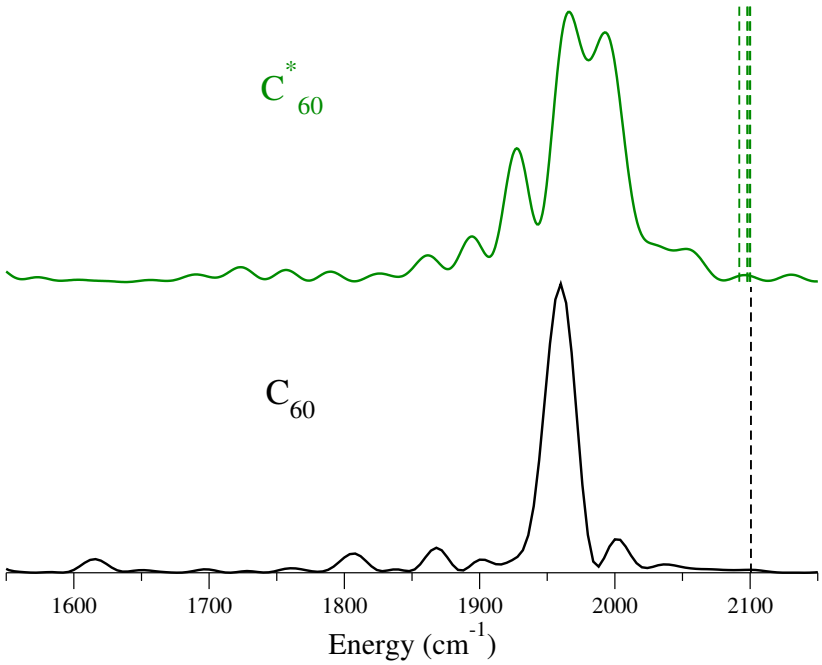

Figure 6.5.4: DC-SCIVR partial spectra of C_{60} (black line) and of C_{60}^{*} (dark green line). Harmonic frequencies are reported in dashed lines.

Chapter 7

How to select the subspaces?

As clearly appears by looking at how the potential, the coherent states, and the pre-exponential factor are projected, a critical issue of the divide-and-conquer method is represented by the choice of the subspaces. The original method, as already introduced, was based on the analysis of the off-diagonal terms of the Hessian matrix. Here we show two other alternative methods, based on the analysis of the monodromy matrix blocks. The common idea behind all of the proposed partitioning methods is to perform a test trajectory, starting from the equilibrium configuration and having initial kinetic energy usually equal to the harmonic ZPE, distributed according to the harmonic frequencies.

7.1 Hessian matrix method

The idea behind it is to enroll in the same subspace the most interacting degrees of freedom, where the indicator is supposed to be the magnitude off the off-diagonal terms of the time averaged hessian matrix along a test trajectory. This assumption is correct in principle in the case of a separable potential, where the off-diagonal terms go to zero. In particular, if the $\tilde{H}_{ij}$ element of the the time-averaged Hessian matrix $\tilde{\mathbf{H}}$ is greater than a threshold value ε, then modes i,j are enrolled in the same subspace. Nevertheless if $\tilde{H}_{ij} \leq \varepsilon$, the two modes could be grouped together if there exists a third mode k, for which $\tilde{H}_{ik} \leq \varepsilon$ and $\tilde{H}_{kj} \leq \varepsilon$. Clearly, by setting $\varepsilon = 0$, the full-dimensional picture is recovered, while the greater is ε the greater is the fragmentation, till reaching a picture where

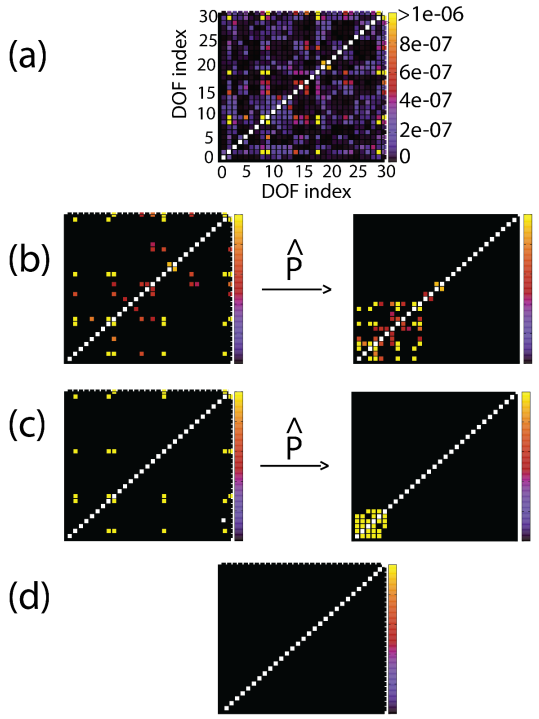

Figure 7.1.1: Hessian matrix elements of a 30-dimensional system at different values of the threshold ϵ. Diagonal elements are out of scale and reported as white pixels. Panel (a) shows as pixels only the coupling elements that are greater than $\epsilon = 0$ a.u. Panels (b), (c) and (d) are similar respectively for $\epsilon = 4.5 \cdot 10^{-7}$a.u., $\epsilon = 9 \cdot 10^{-7}$a.u. and $\epsilon = 6 \cdot 10^{-6}$a.u. In (b) and (c), the matrix elements have been conveniently arranged after permutations ($\hat{\mathbf{P}}$) into sub-blocks. Each sub-block determines a subspace.

the space is fully fragmentated into all mono-dimensional subspaces. This trend is depicted in Figure (7.1.1), where increasing the value of the threshold for a 30-dimensional system, the amount of interaction accounted is reduced. This method is extremely convenient since it requires only the knowledge of the hessian matrix along a test trajectory and the computational cost to obtain the collection of subspaces is negligible compared with the dynamics one. Unfortunately, the method is quite arbitrary and in general one could look at other dynamics quantities.

7.2 Wherle, Sulk, Vanicek method (WSV)

Recently, Wherle, Sulk, and Vanicek proposed a method based on the monodromy matrix, still working on time-averaging the reference matrix and comparing the elements with an arbitraty threshold value.[34] The monodromy matrix can be used as an indicator of interactions since it accounts for the exchange in energy between the degrees of freedom. The first step is the take the monodromy matrix

$$\boldsymbol{M}(t) \equiv \begin{pmatrix} \partial \boldsymbol{p}(t)/\partial \boldsymbol{p}(0) & \partial \boldsymbol{p}(t)/\partial \boldsymbol{q}(0) \\ \partial \boldsymbol{q}(t)/\partial \boldsymbol{p}(0) & \partial \boldsymbol{q}(t)/\partial \boldsymbol{q}(0) \end{pmatrix} = \begin{pmatrix} \boldsymbol{M_{pp}} & \boldsymbol{M_{pq}} \\ \boldsymbol{M_{qp}} & \boldsymbol{M_{qq}} \end{pmatrix} \tag{7.2.1}$$

and to calculate a time averaged matrix $\mathbf{B}$, where each element is equal to

$$B_{ij} = \left| \frac{\beta_{ij}}{\beta_{ii}} \right|, \text{ with } \beta_{ij} = \frac{1}{T} \int_0^T dt \left(|M_{q_i q_j}(t)| + |M_{q_i p_j}(t)| + |M_{p_i q_j}(t)| + |M_{p_i p_j}(t)| \right). \tag{7.2.2}$$

Then a treshold values ε_b is compared with $\max\{B_{ij}, B_{ji}\}$, and similarly to what happens in the hessian method, if $\max\{B_{ij}, B_{ji}\} \geq \epsilon_B$, then modes i,j are collected in the same subspace. Furthermore, in our implementation we set the threshold and we find the corresponding highest dimensional subspace, then on the remaning N_{vib}-M_{max} degrees of freedom we repeat the procedure with an higher value of ε. The procedure is iterated till reaching a complete space separation.

7.3 Jacobi method

Now we propose a method, still based on the monodromy matrix, that looks at the conservation of Liouville theorem. As already shown above in Section (3.2), the monodromy matrix is the Jacobian of the transformation $(\mathbf{p}_t, \mathbf{q}_t) \leftarrow (\mathbf{p}_0, \mathbf{q}_0)$ and by virtue of Liouville's theorem, its determinant has to be equal to one along the classical dynamics of an isolated system. The idea behind our method is to define a subspace as a collection of

degrees of freedom as close as possible to be an isolated system, or better, that does not exchange energy with the remaining vibrational modes. The sentence can be easily translated in formulas by looking at the determinant of a reduced dimensional Jacobian matrix $\tilde{\mathbf{J}}$. In particular, after setting a target subspace dimensionality M, we can look at the combination of degrees of freedom that minimizes the deviation $\left[1 - det\left(\tilde{\mathbf{J}}\right)\right]$ at every time t. In general, the best combination can change with time, and the search should be performed for the whole dynamics lenght. By overall, a set of combinations is obtained, each one resembling the best subspace for a certain dynamics frame. The overall best combination is assumed to be the most probable and on it, we can calculate the average deviation from unity. The procedure can be generalized to different values of M (in principle all possible ones), consequently obtaining for each value of M a M-dimensional combination of degrees of freedom and the averaged deviation $\left[1 - det\left(\tilde{\mathbf{J}}\right)\right]$. The value of M that minimizes the deviation is taken as the best subspace. Then, all the procedure is repeated by looking at the remaning degrees of freedom. As a result, the N_{vib}-dimensional space is separated into disjoint subspaces. This method is in principle more solid than the hessian one; nevertheless, the seek for the best subspace requires to look all the possible permutations of degrees of freedom, and in the case of high values of M, it can become very computationally demanding.

7.4 Applications to variously sized molecular systems

We now perform DC-SCIVR calculations on variously sized molecular systems to test the different partitioning criteria. The vibrational estimates are compared with full-dimensional SCIVR results and exact levels. The systems under investigation span from three-dimensions up to thirdy, with different levels of intermode coupling and chaotic regimes. We believe that all the try-outs provide a broad scenario to test the performance of the partiotioning methods.

7.4.1 a) H_2O

We start from water molecule, the lowest molecular system under investigation. Differently from Section (6.3.3) we employ in this case the Partridge and Schwenke potential,[96] that was recently used as the one-body term for the description of accurate water clusters Potential Energy Surfaces.[92, 60, 94, 93, 91, 99, 100, 101] For SCIVR we run 12000 classical trajectories sampled using the Husimi distribution, while for DC SCIVR calculations we sample 4000 trajectories for each degree of freedom, in order to have the same total number as for SCIVR. The reference state is chosen as $\left|\chi\right\rangle = \left|\mathbf{p}_{eq}\mathbf{q}_{eq}\right\rangle$. Each classical trajectory is propagated for 30000 atomic units. Starting from the Hessian method, the three-dimensional subspace is separated in a mono-dimensional and a bi-dimensional subspaces, where the asymmetric stretching occupies the mono-dimensional one. Both monodromy matrix based methods provide instead a different picture, where the symmetric and asymmetric stretchings are collected in the same subspace and the bending vibration stays alone. Thus, DC SCIVR results arising from WSV, and Jacobi methods will be the same. Table (7.1) reports the computed energy levels compared with SCIVR and exact ones. First of all, we observe that the high anharmonic behaviour of the molecule is properly accounted by both SCIVR and DC SCIVR approaches, as can be evinced by comparing their average deviations (MAE) from the exact results and the same for harmonic estimates. In the first case, MAEs of DC SCIVR are within the typical semiclassical accuracy, while for normal mode analysis the deviation is very high, equal to 140 wavenumbers. All the partitioning criteria performs very well providing almost the same level of accuracy, either when compared with exact values and with full-dimensional SCIVR estimates. Finally, Figure (7.4.1) reports Jacobi DC SCIVR spectra in panels (a) and (b) while vertical dashed lines are centered at SCIVR levels.

Table 7.1: Vibrational frequencies of water. The first column indicate the label of the excitation, while the second one contains exact levels. The third column reports the full-dimensional TA-SCIVR eigenvalues. Column four shows the DC-SCIVR results with the Jacobi subspace criterion (DC $SCIVR_{Jacobi}$); column five with same based on the WSV method (DC $SCIVR_{WSV}$); in column six results obtained by employing the Hessian matrix criterion (DC $SCIVR_{Hess}$) are listed. The last column reports the harmonic estimates. All values are in cm^{-1}. Mean Absolute Error i.e. calculated with respect to exact values[96] and reported in row "MAE exact", while the average deviation from TA-SCVIR results is reported in row "MAE SCIVR".

Mode	Exact[96]	TA SCIVR	DC $SCIVR_{Jacobi}$	DC $SCIVR_{WSV}$	DC $SCIVR_{Hess}$	HO
1_1	1595	1580	1584	1584	1581	1649
1_2	3152	3136	3164	3164	3154	3298
2_1	3657	3664	3668	3668	3656	3833
3_1	3756	3760	3802	3802	3824	3944
MAE Exact		11	20	20	21	141
MAE SCIVR			20	20	23	

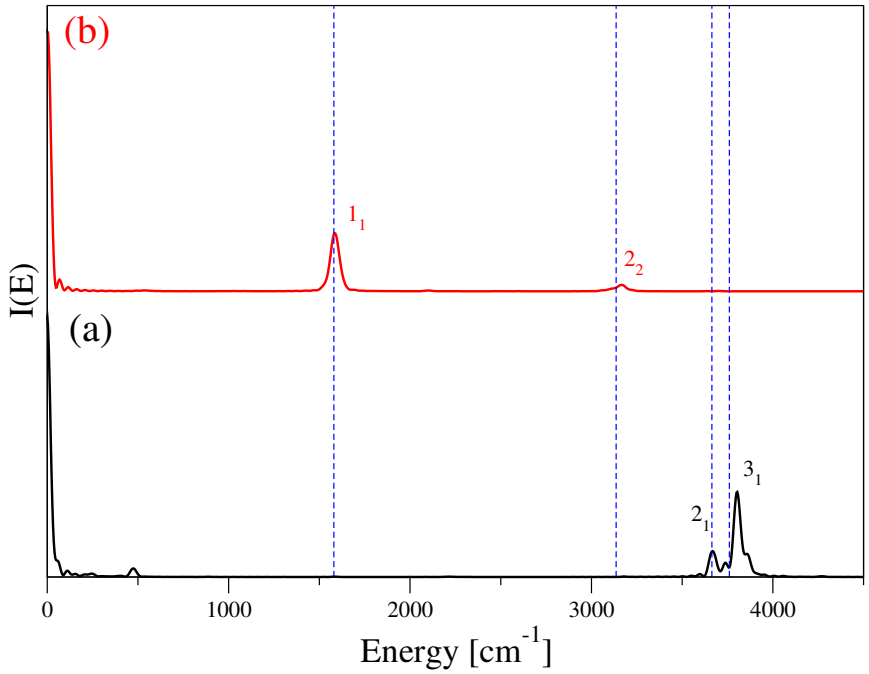

Figure 7.4.1: Jacobi DC-SCIVR spectra of water. Panel (a) show the partial spectrum arising from the bi-dimensional subspace, while panel (b) from the mono-dimensional one. Vertical blue dashed line indicat TA-SCIVR computed levels.

7.4.2 b) CH_2O

We now move toward CH_2O having six vibrational degrees of freedom. Molecular dynamics simulations are performed on the accurate Potential Energy Surface of Martin *et al*[86] for 30000 au, the same as water. We run 24000 classical trajectories in the case of SCIVR simulations while 4000 for each degree of freedom in the case of DC SCIVR. The partitioning criteria once again offer different subspaces; the Hessian method provides a mono-dimensional, a bi-dimensional, and a tri-dimensional subspaces employing a threshold value equal to $\epsilon = 3.0 \cdot 10^{-7}$. By employing the Jacobi method two subspaces are obtained. The highest dimensional is a four-dimensional and the latter contains the remaining two degrees of freedom. The four-dimensional subspace was chosen according to average deviation of $\left[1 - det\left(\tilde{\mathbf{J}}\right)\right]$, as can be evinced by looking at the black line of Figure (7.4.3). The value M=4 minimizes the deviation when compared with other values of subspace dimensionality. The WSV method returns back the same partitioning employing a threshold $\varepsilon_b = 120$. Table (7.2) reports the computed DC SCIVR energy levels with the different partitioning methods compared with both exact and SCIVR values. When either WSV or Jacobi methods are employed, results are very accurate and the MAE with respect to exact levels is 12 wavenumbers, while when the Hessian matrix is used to evaluate the interactions the MAE stays at 25 cm^{-1}. This trend in accuracy is followed also by the deviation from full-dimensional SCIVR results, where the MAE is very low (6 cm^{-1}) for both WSV and Jacobi, while when the hessian method is used the deviation increases to 19 wavenumbers. Finally, Figure (7.4.2) shows the computed DC $SCIVR_{Jacobi}$ partial spectra of the two subspaces.

7.4.3 b) CH_4

We now do a step further by studying vibrational features of methane. This molecule have nine vibrational degrees of freedom, strongly coupled with each other, and undergoing a

Table 7.2: Vibrational excitations CH_2O. The first column reports the label of the excitations, while the second and third one contain exact and full-dimensional SCIVR values. Columns four, five, and six of four DC SCIVR results employing the Hessian method, WSV method and Jacobi method respectively. The last column reports harmonic estimates. Mean Absolute Error i.e. calculated with respect to exact values[58] and reported in row "MAE exact", while the average deviation from TA-SCVIR results is reported in row "MAE SCIVR". Values are reported in cm^{-1}.

Mode	Exact[87]	SCIVR	DC SCIVR$_{Jacobi}$	DC SCIVR$_{WSV}$	DC SCIVR$_{hess}$	HO
1_1	1171	1162	1154	1154	1192	1192
2_1	1253	1245	1246	1246	1244	1275
3_1	1509	1509	1508	1508	1508	1544
4_1	1750	1747	1746	1746	1755	1780
1_2	2333	2310	2288	2288	2286	2384
2_2	2502	2497	2490	2490	2423	2550
5_1	2783	2810	2816	2816	2836	2930
6_1	2842	2850	2845	2845	2864	2996
3_2	3016	3018	3016	3016	3024	3088
4_2	3480	3476	3478	3478	3486	3560
MAE Exact		9	12	12	25	66
MAE SCIVR			6	6	19	

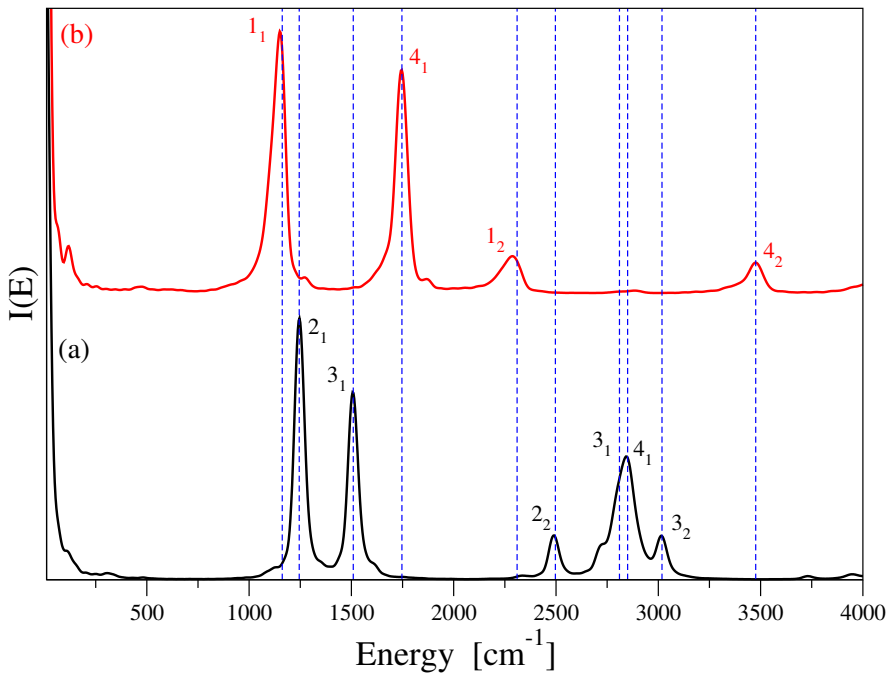

Figure 7.4.2: DC-SCIVR vibrational spectra of CH_2O. Starting from the bottom, panel (a) reports the spectrum of the four-dimensional subspace, while panel (b) the bi-dimensional one. Vertical blue dashed lines indicate the full-dimensional SCIVR values.

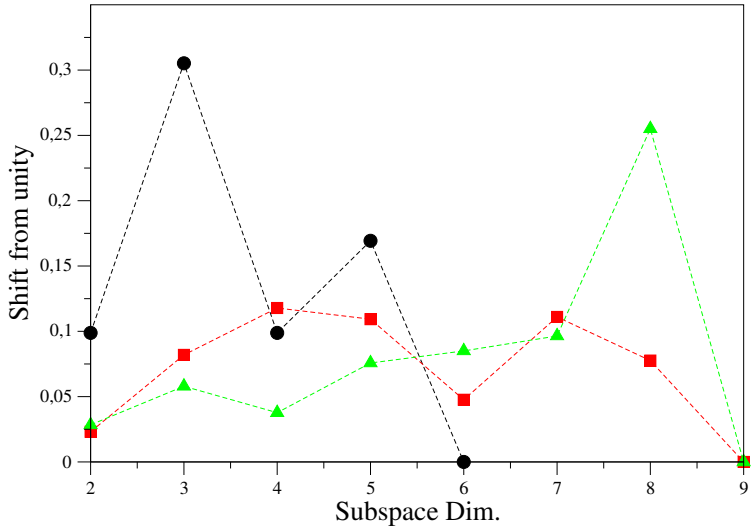

Figure 7.4.3: Average deviation of $\left|1 - \det\left(\tilde{\mathbf{J}}_M(t)\right)\right|$ for the best grouping for different subspace dimensionalities M. Black filled circles for CH_2O , red filled squares for CH_4, and green filled triangles for CH_2D_2.

strong chaotic behaviour. For full-dimensional SCIVR we run 180000 classical trajectories on the Potential Energy Surface of Carter *et al.*[88] The high number of trajectories is necessary because of 95% of rejection ratio. In the case of DC SCIVR calculations 20000 classical trajectories are classically evolved for each degree of freedom, in order to have the same number as for SCIVR. When employing the hessian method, the nine-dimensional space is divided into two subspaces, one six-dimensional and the remaining three-dimensional. When the space is partitioned using the WSV method, a threshold $\varepsilon_b = 85$ leads to a six-dimensional and a three-dimensional subspaces, but different from the outcomes of the hessian method. Finally, when we apply the Jacobi method, the better maximum dimension is six, as can be evinced by looking at Figure (7.4.3). The remaining three degrees of freedom are instead grouped into a bi-dimensional and mono-dimensional subspaces. Table (7.3) shows DC SCIVR energy levels computed by means of the different partitioning, and compared with full-dimensional SCIVR and exact values. All three partitioning methods offer accurate results, and the hessian method seems to be the most accurate one. However, we observe that the most of the deviation for Jacobi and WSV arises from an overtone estimate (1_2) quite off-the mark. If only fundamental exci-

Table 7.3: The same as in Table(7.2) but for the vibrational energy levels of CH_4.

Mode	Exact[58]	SCIVR	DC SCIVR$_{\text{Jacobi}}$	DC SCIVR$_{\text{WSV}}$	DC SCIVR$_{\text{Hess}}$[71]	HO
1_1	1313	1300	1296	1308	1300	1345
2_1	1535	1529	1530	1530	1532	1570
1_2	2624	2594	2556	2588	2606	2690
$1_1 2_1$	2836	2825	2830	2832	2834	2915
3_1	2949	2948	2960	2933	2964	3036
2_2	3067	3048	3060	3044	3050	3140
4_1	3053	3048	3056	3038	3044	3157
MAE Exact		12	17	15	11	68
MAE SCIVR			11	7	7	

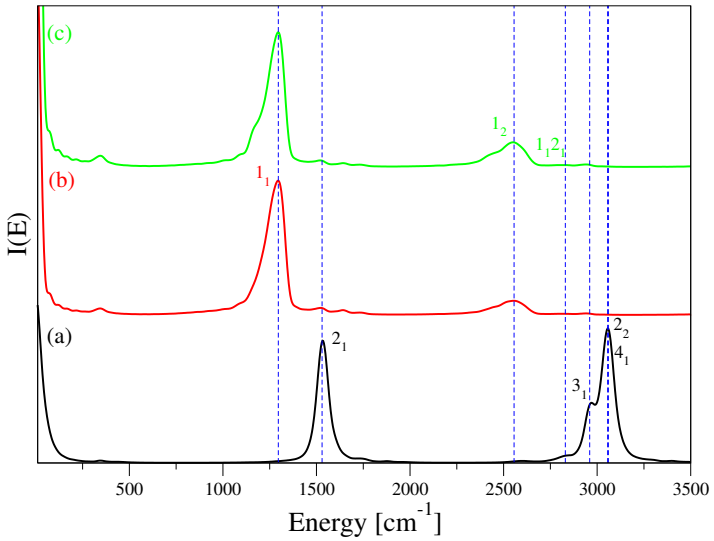

Figure 7.4.4: DC-SCIVR vibrational partial spectra of CH_4 reported with different colors. Starting from the bottom, panel (a) reports the six-dimensional subspace partial spectrum, panel (b) the bi-dimensional one, and panel (c) the mono-dimensional one. Vertical blue dashed lines indicate the full-dimensional SCIVR values.

tations are considered, then even deviations of Jacobi and WSV approach DC SCIVR$_{\text{hess}}$ one. Finally, Figure (7.4.4) shows the DC SCIVR$_{\text{Jacobi}}$ partial spectra, where starting from the bottom we find the six-dimensional, bi-dimensional, and mono-dimensional power spectra.

7.4.4 c) CH_2D_2

After methane we look for one of its isotopologue, CH_2D_2. The chaotic regime of the classical trajectories seems to be not tamed too much, despite the presence of two heavier atoms. Consequently the rejection ratio remains almost unchanged. Thus, on the same Potential Energy Surface,[88] 180000 trajectories are evolved for SCIVR calculations and 20000 per degree of freedom in the case of DC SCIVR simulations. When the hessian method is employed with a threshold value equal to $\varepsilon = 2 \cdot 10^{-7}$, the nine-dimensional space is separated into a six-dimensional and a three-dimensional subspaces. When instead, we take advantage of the Jacobi method, the first outcoming subspace is a four-dimensional one, as depicted in Figure (7.4.3), while the remaining five degrees of freedom are collected into a bi-dimensional and a three-dimensional subspaces. Finally, with a threshold $\varepsilon_B = 180$, the WSV method, provides a four-dimensional, a three-dimensional, and a bi-dimensional subspaces, with a different partition of the degrees of freedom when compared with the Jacobi method. Table (table 7.4) reports the computed energy levels according with the different space-partitions, together with SCIVR estimates, and exact results. Once again, Jacobi DC SCIVR results are the most accurate and are comparable with full-dimensional vibrational estimates. Moreover, the hessian method seems to be as accurate as WSV one, but the latter is closer to full-dimensional SCIVR benchmark values. By overall, all partitioning methods provide estimates within the typical range of accuracy of semiclassical methods, and in general all results are much better than simple Normal Modes Analysis. Finally, Figure (figure 7.4.5) shows the DC SCIVR spectra in the case of Jacobi subspaces.

7.5 Application to Benzene

Last, we test the partitioning methods against a molecule for which the curse of dimensionality makes unfeasible full dimensional calculations, *i.e.* Benzene. It is made

Table 7.4: The same as in Table(7.2) but for the vibrational energy levels of CH_2D_2.

Mode	Exact[58]	SCIVR	DC SCIVR$_{\text{Jacobi}}$	DC SCIVR$_{\text{WSV}}$	DC SCIVR$_{\text{hess}}$	HO
1_1	1034	1026	1028	1020	1038	1053
2_1	1093	1084	1072	1098	1086	1116
3_1	1238	1230	1234	1212	1230	1266
4_1	1332	1329	1320	1326	1316	1360
5_1	1436	1430	1430	1420	1434	1471
$1_1 2_1$	2128	2110	2089	2080	2114	2169
6_1	2211	2199	2195	2192	2137	2236
$1_1 3_1$	2242	2236	2250	2231	2210	2319
7_1	2294	2268	2274	2250	2274	2336
$1_1 4_1$	2368	2356	/	/	2400	2413
$1_1 5_1$	2474	2456	2485	2436	2484	2524
$2_1 5_1$	2519	2504	2516	2494	2510	2587
$3_1 5_1$	2674	2660	2661	2672	2627	2737
$4_1 5_1$	2769	2756	2754	2734	/	2831
8_1	3008	3050	3000	3012	3026	3103
MAE Exact		14	13	21	21	47
MAE SCIVR			12	15	19	

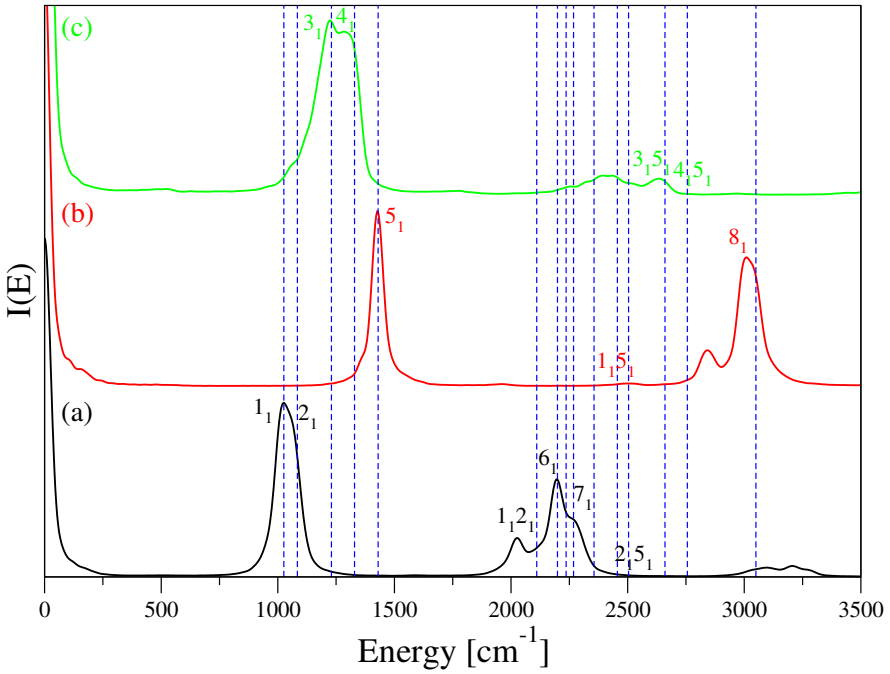

Figure 7.4.5: DC-SCIVR vibrational spectra of the CH_2D_2 molecule. Starting from the bottom; panel (a) is for the 4-dimensional subspace, panel (b) for the three-dimensional, and panel (c) for the remaining bi-dimensional subspace. Vertical blue dashed lines are the full-dimensional SCIVR values.

by twelve atoms and consequently 30 vibrational degrees of freedom. Because of the high-dimensionality, we run 1000 classical trajectories per degree of freedom, employing a second-order iterative approximation of the pre-exponential factor to avoid rejection events. The Potential Energy Surface is the one by Handy[97] for which Halverson and Poirier recently computed exact vibrational eigenvalues.[14] The test trajectory for the partitioning methods is sampled at equilibrium configuration and a 95% fraction of harmonic ZPE is given to account for anharmonicity. To remove noisy spurious effects in the spectra we adopt in the Fourier transform a Gaussian filter of the type $e^{-\alpha t^2}$ with $\alpha = 3 \cdot 10^{-8}$ a.u.. As already reported above, the hessian method provides a eight-dimensional, eight bi-dimensional, and six mono-dimensional subspaces. When WSV method is employed with a threshold value $\varepsilon_B = 5.6 \cdot 10^3$, the full-dimensional space is divided into a ten-dimensional, two seven-dimensional, and a six-dimensional subspaces. Finally, when employing the Jacobi method we restrict the seek for the best subspace in the range of subspace dimensionality 6≤M≤10. It represents a good trade-off between accuracy and computation demand, since the dimensionality range is centered close to maximum subspace dimensionality obtained with the original hessian method, and the maximum value (M=10) is instead equal to WSV maximum dimensionality. Higher values of M would require a too high computational demand which would hardly significantly improve results. Within this restrictions, from the full-dimensional space is first separated a seven-dimensional subspace, as reported in Figure (figure 7.5.1). Then, a ten-dimensional subspace and six-dimensional one. Eventually, the remaining degrees of freedom are grouped together into a seven-dimensional subspace. Table (table 7.5) reports the computed DC SCIVR energy levels with the different partitioning methods. The column associated to the Hessian method is missing since results are already present in Table (table 6.3). Jacobi estimates are very accurate with an average deviation of only 9 wavenumbers from exact levels. Conversely, the hessian method is the least accurate with an average deviation of 19 cm^{-1}(values are reported in Section section §6.4); WSV

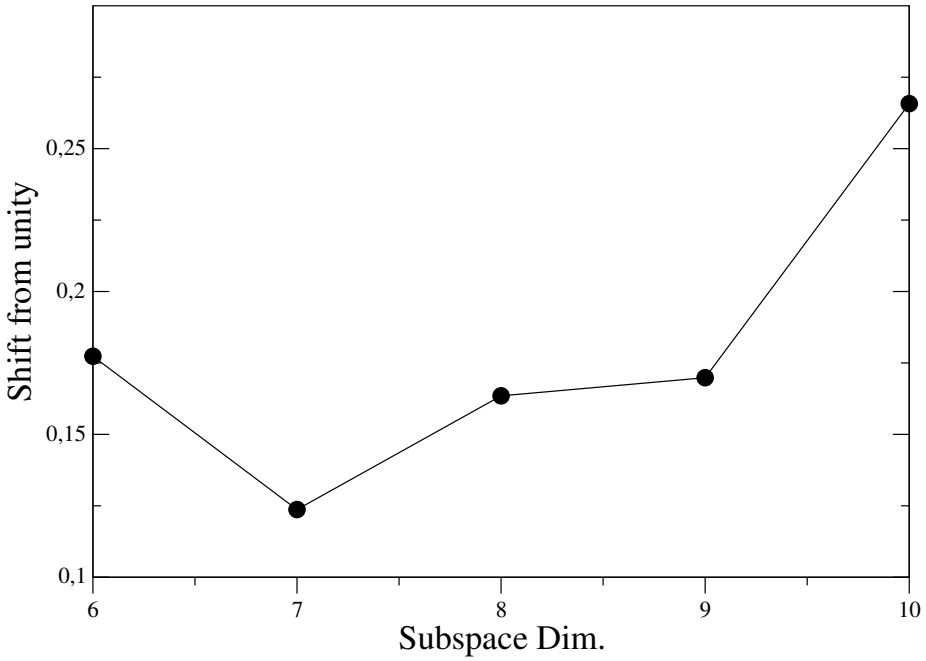

Figure 7.5.1: Values of $\left|1-\det\left(\tilde{\mathbf{J}}_M(t)\right)\right|$ for different choices of the subspace dimensionality M for the C_6H_6 molecule in the range $6 \leq M \leq 10$.

Table 7.5: DC-SCIVR vibrational frequencies of benzene. Columns "EQD" report available quantum results. Columns "DC $SCIVR_{WSV}$" are for frequencies obtained employing the WSV method, while Columns "DC $SCIVR_{WSV}$" indicate results arising from the Jacobi method. Energies are reported in cm^{-1}.

State	HO	DC $SCIVR_{WSV}$	DC $SCIVR_{Jacobi}$	EQD	State	HO	DC $SCIVR_{WSV}$	DC $SCIVR_{Jacobi}$	EQD
1_1	407	432	399	399.4554	11_1	1167	1150	1144	1147.751
2_1	613	610	606	611.4227	12_1	1192	1189	1175	1180.374
3_1	686	610	696	666.9294	2_2	1226	1223	1228	1221.27
4_1	718	742	719	710.7318	13_1	1295	1330	1314	1315.612
5_1	866	865	869	868.9106	14_1	1390	1375	1352	1352.563
6_1	989	990	997	964.0127	4_2	1436	1410	1437	1418.58
7_1	1011	1038	1020	985.8294	15_1	1512	1464	1492	1496.231
8_1	1008	1002	990	997.6235	16_1	1639	1614	1602	1614.455
9_1	1024	1014	1014	1015.64	5_2	1732	/	1752	1737.51
10_1	1058	1042	1042	1040.98	MAE		15	9	

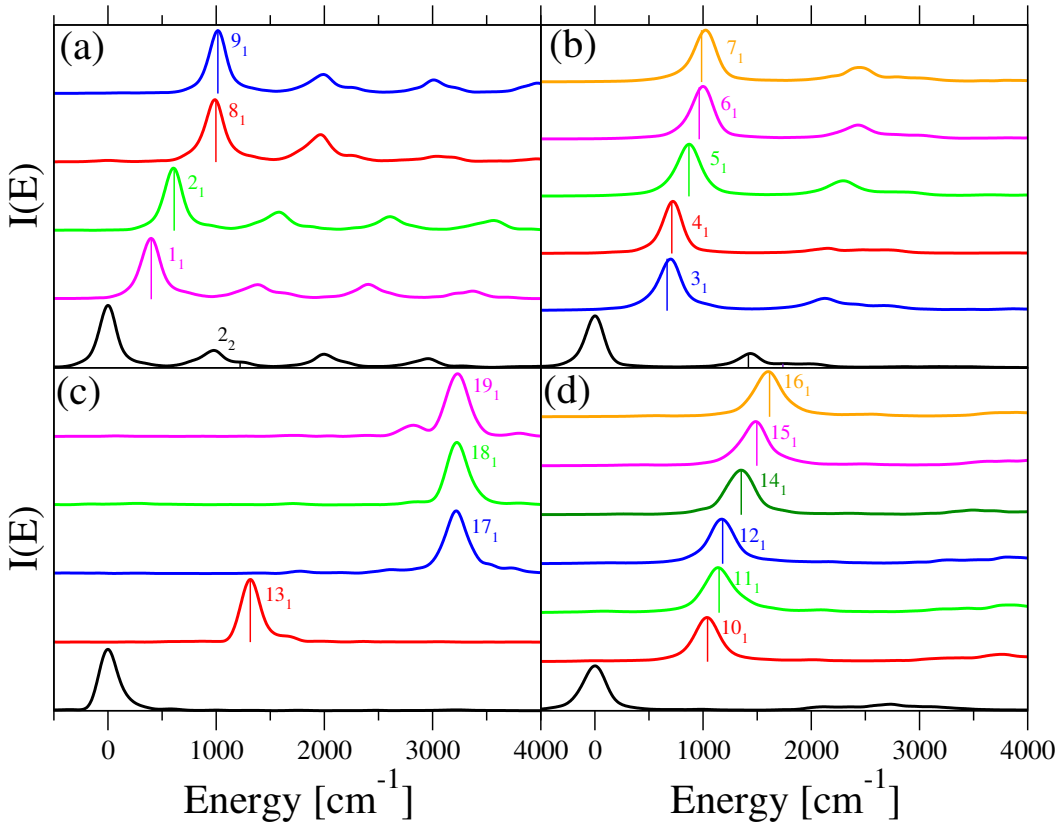

Figure 7.5.2: Vibrational spectra of C_6H_6 as a result of the Jacobi partitioning method. Panel (a) reports fundamental excitations spectra of the six-dimensional subspace. Panels (b) and (c) contain the spectra of the two seven-dimensional subspaces, while panel (d) refers to the 10-dimensional subspace. The vertical lines are centered at the exact EQD levels.[14]In black line is reported the Zero Point Energy signal for each subspace.

method lies in the middle, with a very good accuracy since the MAE is only 15 cm^{-1}. Finally, Figure (figure 7.5.2) reports the spectra obtained according with the Jacobi method.

7.6 Application to Zundel cation

Our last application concerns Zundel cation $H_5O_2^+$, a molecule known to be extremely anharmonic and vibrationally strongly coupled. For this reasons it represents a very tough challenge for any molecular dynamics based method. In particular, motions involving the shared proton can be shifted from harmonic estimates even by hundreds of wavenumbers,

making a simple normal mode analysis definitely insufficient. Moreover, the coupling of water bendings with the proton transfer motion generates an high separation in energy between the gerade and ungerade frequencies. The main spectral feature of this molecule is however the signal associated to the proton transfer; it is not only highly anharmonic but it also shows a doublet in the range 900-1100 cm^{-1}. In our investigation, we focus of these main spectral features, *i.e.* proton transfer excitations, OH bendings plus OH stretchings, which are intense and located at higher energies showing a typical double peak. Molecular dynamics are performed on the accurate Potential Energy Surface of Huang *et al*,[102] for which in the past years Vendrell *et al* provided very detailed MCTDH results and vibrational estimates.[103, 104, 105, 106, 107, 108, 109] Classical trajectories usually undergo a strong ro-vibrational coupling and the removal of rotational energy is required to obtain clear vibrational signals. It unavoidably implies a loss in total energy, that nevertheless does not affect too much spectral densities. This strong ro-vibrational coupling leads also to an high instability of the monodromy matrix making not possible to employ partitioning methods based on it. For this reason we rely on the hessian method. Furthermore, because of this complex scenario, full-dimensional TA SCIVR calculations do not provide an undisputed picture, and DC SCIVR estimates will be only compared with available quantum estimates. Rejection events are also avoided by employing a second order iterative approximation of the pre-exponential factor. The hessian based analysis of the test trajectory suggests to enroll the four OH stretchings vibrations together in same subspace, while the two water bendings and the shared proton motion should be enrolled in mono-dimensional subspaces. The OO stretching vibration is instead collected in a bi-dimensional subspace together with a wagging state, by taking insights from previous Literature results. Eventually, we sample 2000 classical trajectories per degree of freedom, namely 8000 for the four-dimensional subspace, 4000 for the bi-dimensional subspace, and 2000 for each one of the mono-dimensional subspaces. Figure (7.6.1) shows the spectrum associated to the four OH stretchings where peaks in panels (a) and (b) were

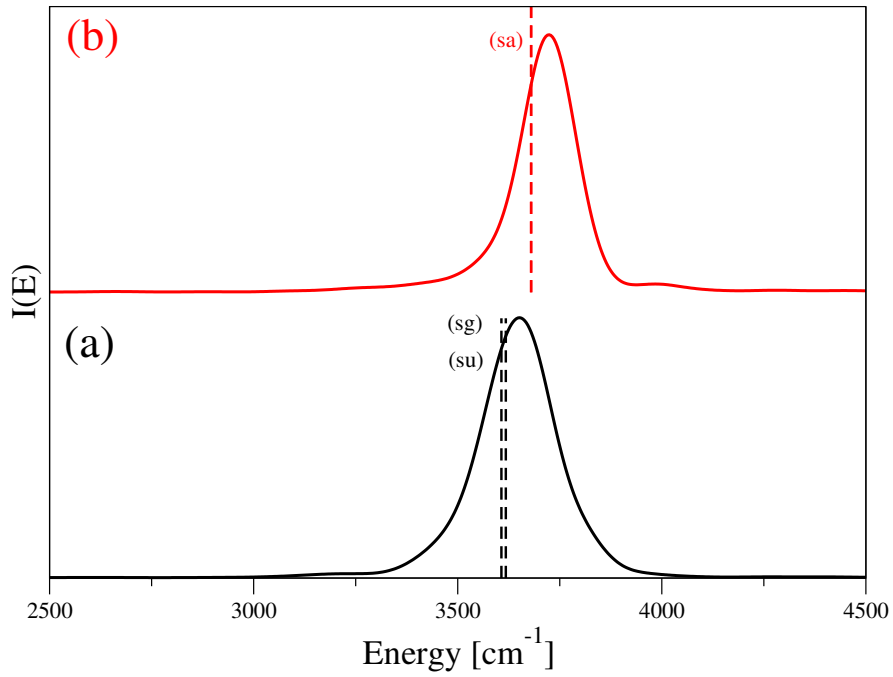

Figure 7.6.1: Vibrational spectra of OH stretching vibrations of Zundel cation. Starting from top, panel (b) is for the double degenerate (sa) excitations, while panel (a) is the spectrum of the (sg) and (su) stretchings. The vertical lines are centered at MCTDH estimates.[103]

obtained by tailoring the reference state according with the Multiple Coherent state approach. In particular panel (a) shows the peak associated to (sg) and (su) excitations, while panel (b) the remaining two OH stretchings, the double degenerate (sa) states. The labels follow the usual nomenclature found in the Literature.[103, 108] Figure (7.6.2) instead reports low energetic excitations, as the two bendings (bg) and (bu), the proton transfer signal $(1z)$, the OO stretching labelled by $(1R)$, and the wagging state (ω_3) spectrum. We can observe that also evidences of the combined excitation $(1R, \omega_3)$ are present in the red spectrum, as well as $(1z, 1R)$ in the blue one. Table (7.6) summarizes our computed DC SCIVR levels, compared with available quantum results. The overall deviation (MAE) from MCTDH estimates is 46 cm^{-1}, mainly due to the overtone$(1z, 1R)$ estimate that is quite off-the mark. If we exclude it, MAE decreases to 38 cm^{-1}, that is quite a good result considering the complexity of the molecule, and the usual accuracy of semiclassical methods.

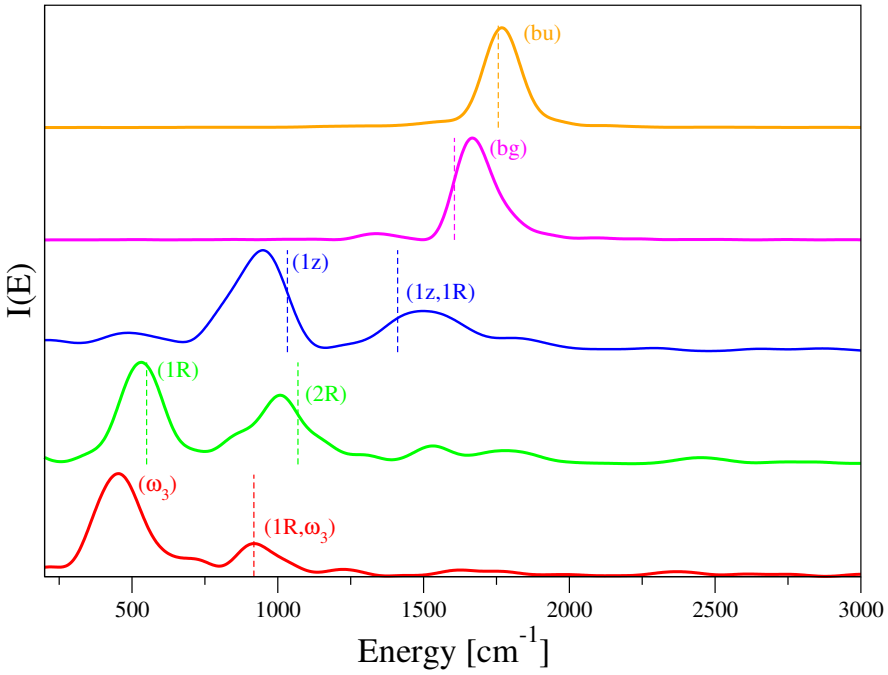

Figure 7.6.2: Vibrational spectra of Zundel cation below 2000 wavenumbers. Starting from the top, orange and magenta lines are spectra of mono-dimensional subspaces associated to the two water bending excitations (bu) and (bg). Blue line reports the proton transfer signal $(1z)$. Green and red lines reports the spectra of $(1R)$ and (ω_3) excitations belonging to the same bi-dimensional subspace. The vertical lines are centered at MCTDH estimates.[103]

Table 7.6: Vibrational energy levels of Zundel cation reported in cm^{-1}. The first column reports the label of the excitation according with Ref.[103] The second column contains experimental values, the third one MCTDH results,[103] while the fourth one our DC-SCIVR estimates. Column five reports VCI energy levels[110] and the column six harmonic estimates of fundamental excitations. The last row reports the mean absolute error of DC-SCIVR estimates with respect to MCTDH values.

Label	Exp[111]	MCTDH[103]	DC SCIVR	VCI[110]	HO
(1R)		550	532		630
$(1R, \omega_3)$	928	918	920		
(1z)	1047	1033	952	1070	861
(2R)		1069	1008		
$(1z, 1R)$	1470	1411	1520	1600	
bg		1606	1668	1604	1720
bu	1763	1756	1768	1781	1770
sg		3607	3650	3610	3744
su	3603	3614	3650	3625	3750
sa	3683	3689	3720	3698	3832
MAE			46		

7.7 Summary

The investigation of H_2O, CH_2O, CH_4, CH_2D_2 by means of DC SCIVR approach combined with different partitioning methods suggests that vibrational estimates are in general accurate when compared with either exact and full-dimensional TA SCIVR values. The overall accuracy is in general within the typical range provided by semiclassical methods. Moreover, DC SCIVR can also access systems' dimensionalities which are out of reach for the standard TA SCIVR approach, as can be evinced by looking at Benzene application. Finally, despite the extremely high complexity, even molecules as Zundel cation are accessible with quite good accuracy. However, for this last case, the already cited complex motion leads to an high ro-vibrational coupling that is mainly responsible of a general broadening of the spectral features.

As a general outcome, the decomposition of the whole spectra density into partial ones helps the recovery of clear signals and makes easier their undisputed assignment, that otherwise would be very hard, especially in the presence of peaks very close in energy. This issue is expected to be more helpful as the dimensionality increases, where the number of peaks raises in the typical range of vibrational excitations. Moreover, the Jacobi method seems to be the most accurate one, probably as a consequence of seek for subspaces close to preserve Liouville theorem. The WSV method is in general more accurate that the Hessian one as can be evinced by looking at Figure (7.7.1).

Further applications of the divide-and-conquer method are reported below and exploit systems characterized by a very complex Potential Energy Surface as water clusters, and other molecular systems relevant in biological and technological processes.

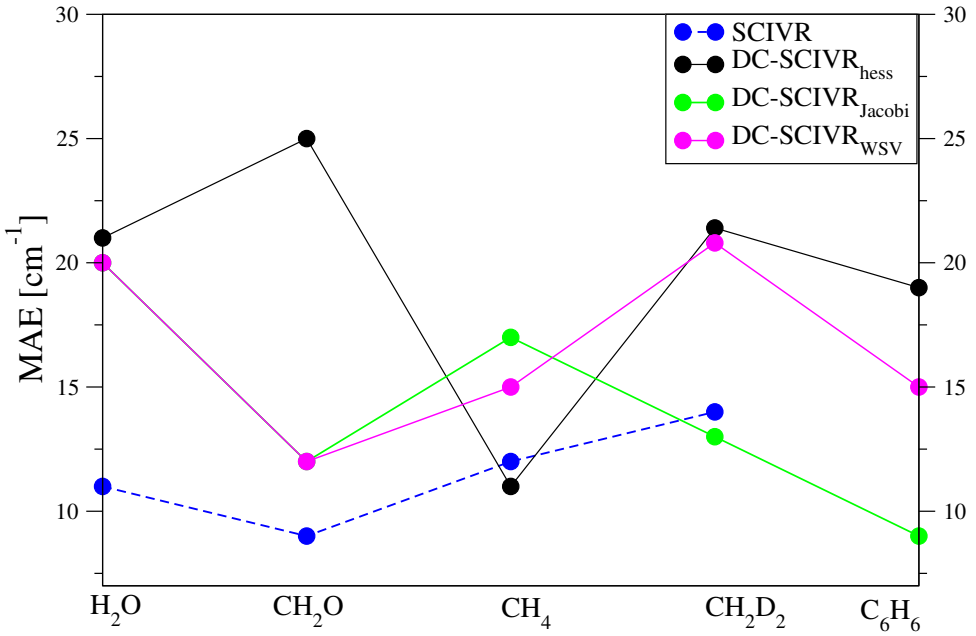

Figure 7.7.1: Mean absolute error (MAE) for the different molecular systems investigated. Blue values are for full-dimensional TA SCIVR calculations, while black ones are based on DC SCIVR$_{hess}$ results. DC SCIVR$_{Jacobi}$ and DC SCIVR$_{WSV}$ results are reported in green and magenta respectively. The overall trend of the MAE is reported with solid lines for DC SCIVR, and with a dashed line for TA SCIVR.

Chapter 8

Vibrational investigation of water clusters

We now apply the divide-and-conquer method to study water clusters of increasing dimensionality. A twofold reason trigger this choice; the first one involves the increasing importance that they have been gained in recent years, and the second one is instead their very high complexity. Our results are compared with experiments when possible, and with MultiMode and Local Monomer calculations of Bowman and co-workers. Below in the text an introduction about the state of art of water clusters is reported, then we report the computational setup. In the remaining sections the method is first applied on water dimer and trimer to show its reliability, and then the focus moves toward the water hexamer, for which relevant conclusions can be drawn about the importance of dynamical effects. Finally, the water decamer is investigated by employing an extension of the Multiple Coherent State approach, because of the high computational overhead required to run thousand and thousand classical trajectories.

8.1 Introduction

The water molecule has always catalyzed the attention of the scientific community due to the fundamental role that it plays into processes responsible of the life on our planet.[112, 113, 114, 115, 116, 117, 118] The effects of the peculiar interaction mechanism between

water molecules, mainly due to hydrogen bonds which govern most of its physical and chemical processes were deeply studied by both experiment and theory.[119, 120]Such interactions are also the main responsible of the formation of variously sized networks called water clusters.[121, 122, 123]

Water clusters are systems made by water molecules which represent a very important and challenging test case to deeply understand the overall properties of water. They are also assumed to be important for their implications in photocatalytic processes in the atmosphere.[124, 125] They were deeply and widely investigated in the past, both focusing on the structure and the interaction network, by taking advantage of both theoretical and experimental approaches.

The attention focused on water clusters went also beyond homogeneous clusters in recent years, since today concerns also the interaction picture between water and other molecules like methane and clatrates,[59, 126] HCl hydrates[127, 128, 129] or even solvated ions.[130, 131, 132, 133] Furthermore, hundreds of papers have enriched the literature in the field of water molecules sharing a proton.[109, 108, 107, 106, 105, 104, 103, 134, 135, 136, 137, 110, 22, 138, 111, 139, 140, 141, 142, 143] These protonated water clusters represent the best simplified model systems to investigate and to understand the nature and the implications of the proton transfer mechanism in aqueous solutions.

Starting from 80s and 90s, several accurate vibrational spectra were reported in the literature for small, medium and large sized clusters and the presence of four main features was very often displayed in the region 1500-4000 cm^{-1} of the spectrum. The first one, lowest in energy, relies to the OH bending frequencies roughly at 1600 cm^{-1},[144, 145, 146, 147] the other three are instead present at higher energies rely to OH stretchings at approximately 3000, 3500, and 3700 wavenumbers. The highest in energy is due to free OH stretches, while the remaining are due to hydrogen bonded OH stretches.[148, 149, 150, 151, 152, 153, 154, 155] Moreover, Clary and co-workers suggested that hydrogen bonds guide to what is the most stable isomer, and vibrational spectroscopy is a good

probe of their presence,[156] because the vibrational spectral features of OH bonds were shown to be extremely sensitive to hydrogen interactions. To understand this issue it is enough to think that they could undergo a red-shift that can reach even roughly 600-700 cm^{-1}.[157, 148, 149, 150, 152] On an opposite trend, the position of free OH stretchings is instead almost unchanged with the clusters' size.[157, 148] In the bending region instead a slight overall blue-shift of the OH frequencies is observed with the increasing of the clusters' size.[144]

From the theoretical side, Xantheas and co-workers, followed by others research groups, revealed that even in the presence of small clusters, the potential energy surface is very complicated because several local minima are possible and their energy differences can be even fewer than 200-300 wavenumbers.[158, 159, 160, 161, 162, 163, 164] Moreover, Zero Point Energy contribution is definitely not-negligible to determine the relative stability between such several minima.[158] Consequently, an high level of theory is necessary to properly represent, ruling out the possibility to exploit ab-initio simulations. The development in the past years of fitting procedures and accurate parametrizations of the PES has opened the way to many theoretical investigations of small, medium, large sized water clusters.[100, 91, 95, 94, 165, 166, 167, 168, 169, 170, 171, 172] Among all we recall the work done by Purtridge and Schwenke[90] in which they developed an accurate one body term, and the parametrization of the water model by Burnham and Leslie.[173] Most recently the effort profused by the groups of Xantheas and Bowman led to a very accurate dynasty of Potential Energy Surfaces.[91, 93, 99, 92, 174, 101][175, 176, 177, 178] In particular, Bowman's HBB and later WHBB PES were showed to be extremely accurate and flexible for water clusters of any size. In these last PES implementations are present two and three body terms, since the high order ones are negligible as shown by the groups of Xantheas, Clary and Paesani.[179, 180, 171]

In this work we present a theoretical investigation of variously sized water clusters with our new-established divide-and-conquer semiclassical method DC-SCIVR.[71, 181]

Results show that quantum anharmonic effects are not-negligible, and dynamics effects are relevant because of strong hydrogen bond interactions. Furthermore, we also provide a methodology to reduce the computational demand and to calculate spectra of high dimensional systems characterized by several relevant minima, retaining good accuracy.

8.1.1 Computational setup

Power spectra of water clusters are calculated by means of the divide-and-conquer method already introduced above in the text. All molecular dynamics simulations are performed for 30000 atomic units, and the sampling function is the Husimi distribution as usual. From one up to 10000 classical trajectories are sampled for each subspace. The high complexity of these systems requires to introduce a further device consisting into giving zero initial kinetic energy to very low energetic libration motions. Nevertheless, we show that this *ad-hoc* trick does not relevantly affect the accuracy of the OH bendings and stretches spectra. Throughout the text, results labelled by DC SCIVR$_{\mathrm{Xk}}$ are based on X000 trajectories sampled for each subspace, while MC-DC SCIVR$_{1\ \mathrm{traj}}$ labels results arising by employing the multiple coherent state approach, where the equilibrium position is located at geometry global minimum. We also calculate the Fourier transform of the classical velocity velocity correlation function by taking advantage of the divide-and-conquer method, to further understand the very complex nature of some OH stretching excitations strongly red-shifted because of hydrogen bonding. Furthermore, similarly to what done by Kaledin and Miller for semiclassical spectral densities it also possible to time-averaged the classical expression. The standard expression is

$$I\left(E\right)=\int dte^{iEt}\Big\langle \mathbf{v}\left(t\right)\mathbf{v}\left(0\right)\Big\rangle =\int dte^{iEt}\int d\mathbf{p}_{0}d\mathbf{q}_{0}\rho\left(\mathbf{p}_{0},\mathbf{q}_{0}\right)\mathbf{v}_{t}\left(\mathbf{p}_{0},\mathbf{q}_{0}\right)\mathbf{v}_{0}\left(\mathbf{p}_{0},\mathbf{q}_{0}\right), \tag{8.1.1}$$

where ρ is a distribution function used to sample initial conditions. Following Kaledin and Miller idea, we can add a further time-integration and obtain a working formula for

the time-averaged version of Eq. (8.1.1), where the time T concerns the amount of the time in which the correlation function is time averaged.

$$I(E) = \int d\mathbf{p}_0 d\mathbf{q}_0 \rho(\mathbf{p}_0, \mathbf{q}_0) \frac{1}{2T} \left| \int_0^T dt e^{iEt} \mathbf{v}_t(\mathbf{p}_0, \mathbf{q}_0) \right|^2 \tag{8.1.2}$$

In the divide-and-conquer framework projected quantities replace full-dimensional one and the equation becomes

$$\tilde{I}(E) = \int d\tilde{\mathbf{p}}_0 d\tilde{\mathbf{q}}_0 \tilde{\rho}(\tilde{\mathbf{p}}_0, \tilde{\mathbf{q}}_0) \frac{1}{2T} \left| \int_0^T dt e^{iEt} \tilde{\mathbf{v}}_t(\tilde{\mathbf{p}}_0, \tilde{\mathbf{q}}_0) \right|^2. \tag{8.1.3}$$

8.1.2 A three body version of the Potential Energy Surface

Our molecular dynamics simulations are performed on the accurate WHBB Potential Energy Surface.[92, 93, 60, 91] It was constructed as a combination of different many body contributions, truncating the expansion at the three-body term. Many body contributions were shown to be negligible in the past years.

$$V(\mathbf{q}) = \sum_i^N V^W(\mathbf{q}_i) + \sum_{j>i}^N V^{W-W}(\mathbf{q}_i, \mathbf{q}_j) + \sum_{k>j>i}^N V^{W-W-W}(\mathbf{q}_i, \mathbf{q}_j, \mathbf{q}_k), \tag{8.1.4}$$

We denote with V^W the one body contribution arising from the Partridge and Schwenke potential,[96] with V^{W-W} and V^{W-W-W} the two- and three-body terms of the WHBB potential. Our semiclassical calculations will explore high-dimensional clusters for which the calculation of two and three body terms is computationally demanding. To overcome this problem we present a new version of the three body interaction potential, obtained from a refit of the original 40000 ab-initio point database used to obtain V^{W-W-W} of the WHBB. The new version is made by 1181 polynomials and shows a root mean square deviation of 46 cm^{-1} from the ab-initio points, and 51 cm^{-1} from the original WHBB with

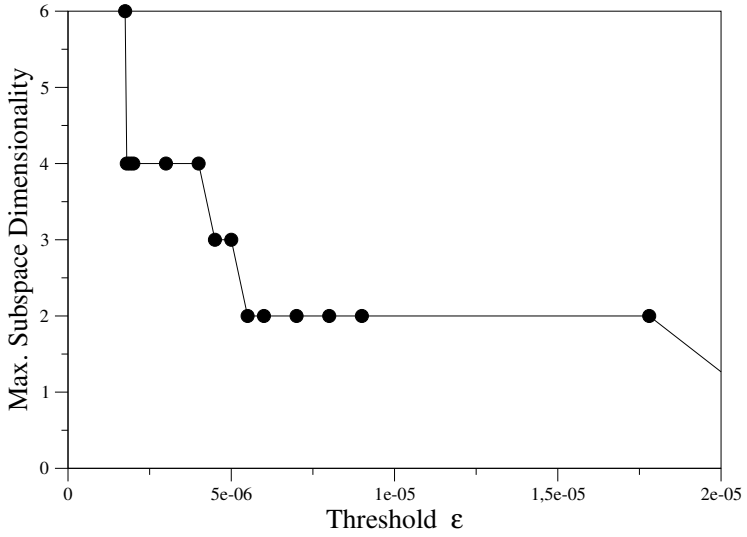

Figure 8.2.1: Dependence of the maximum subspace dimensionality on the arbitrary Hessian threshold for the water dimer.

maximum polynomial order 5. It is roughly 70 times faster, and has a similar speed to a new version of the potential developed in the group of Bowman and called WHBB2.[99]

8.2 Water Dimer $(H_2O)_2$

The water dimer is the lowest dimensional water cluster, it is made by two weakly interacting water molecules. Six of the twelve degrees of freedom are OH stretching and OH bending vibrations. We apply DC SCIVR approach by sampling classical trajectories 30000 atomic units long. Unfortunately, by providing initial kinetic energy to all the vibrational modes, outcoming spectra are too noisy for an undisputed assignment probably because of a strong ro-vibrational coupling involving low energetic excitations. We decided to give zero initial kinetic energy to the very low energetic flussional modes with the aim of mitigating this effect. The hessian method is used to partition the full-dimensional space, and the trend of the maximum subspace dimensionality for the test trajectory is reported in Figure (8.2.1). As a first tentative we took a six-dimensional subspace made by all the OH stretching and OH bending vibrations, but unfortunately once again spectra were too noisy. Consequently, we descreased the maximum subspace

Table 8.1: Vibrational frequencies of the water dimer, in cm^{-1}. Assignments of mode excitations are reported in the first column; the following columns present, in order, the experimental results, the harmonic estimates, Multimode (MM) and Local Monomer Model (LMM) results, DC-SCIVR frequencies obtained from 5,000 and 10,000 trajectories, MC-DC-SCIVR frequencies based on 5 trajectories, and MC-DC-SCIVR results from a single trajectory started from the global minimum. The mean absolute errors (MAE) for the DC-SCIVR simulations are relative to the experimental values. The MAE for the MC-DC-SCIVR simulations are referred to DC-SCIVR$_{10k}$ results. [a] from Ref. 145; [b] from Ref. 91.

Index	Exp.[a]	HO	MM[b]	LMM[b]	DC SCIVR$_{10k}$	DC SCIVR$_{5k}$	MC-DC SCIVR$_{5}$ trajs, multmin	MC-DC SCIVR$_{1}$ traj
7_1	1600	1650	1588	1595	1597	1597	1562	1572
8_1	1617	1669	1603	1602	1585	1578	1588	1578
7_2	3163	3300	3144	3153	3154	3178	3128	3156
8_2	3194	3338	3157	3168	3130	3100	3180	3156
9_1	3591	3758	3573	3550	3550	3539	3476	3356
10_1	3661	3828	3627	3637	3690	3693	3680	3540
11_1	3734	3917	3709	3701	3670	3671	3582	3628
12_1	3750	3935	3713	3724	3764	3764	3717	3690
MAE			25	23	32	39	48	69
	7207					7266		
	7362					7336		
	5328					5375		

dimensionality following the trend shown in Figure (8.2.1), till reaching a value equal to two, corresponding to a wide plateau. The threshold value employed in our calculation is $\varepsilon = 1.8 \cdot 10^{-5}$. We started all the trajectories with the cluster in its equilibrium geometry. Initial atomic velocities were extracted, for each subspace calculation, from the chosen distribution of the normal mode initial kinetic energy. Specifically, for modes included in the subspace under investigation a Husimi distribution centered on momentum values corresponding to one quantum of harmonic excitation was employed; other bending and stretching motions belonging to different subspaces were instead assigned the corresponding harmonic zero-point energy contribution. Below are shown results by running from 1 up to 10000 classical trajectories for each subspace. As a first evidence, we observe that in general 5000 classical trajectories for each subspace are enough to reach a reasonable convergence in peaks' position. In Table (8.1) DC SCIVR results are compared with experimental, MM and LMM calculations. When either DC SCIVR$_{5k}$ and

DC SCIVR$_{10k}$ are employed, vibrational frequencies are in good agreement with experimental ones with an average deviation of 39 cm^{-1} and 32 cm^{-1}, not so higher than 25 cm^{-1} of the MM benchmark method. On the opposite, single trajectory simulations MC-DC SCIVR$_{\text{single traj}}$ are very often off the mark. To better understand the reasons behind this discrepancy we investigated the Potential Energy Surface, and we found other four relevant local minima, very close in energy (below 200 cm^{-1}) to the global one. We sampled 1000 trajectories and run damped dynamics, where at each time-step velocities were scaled by a factor equal to 0.99 and checked if it was terminated into a minimum different from the global one. We repeated MC-DC-SCIVR calculations, by sampling for each subspace 5 classical trajectories, each one starting from a different minimum. By overall, the Mean Absolute Error descreases from 69 to 48 wavenumbers. This "multiple-minima" implementation suggests that for this molecular system non-local effects are relevant, and they can be responsible of non-negligible dynamics effects. It can also partially justify the differences between DC SCIVR$_{10k}$ and MM results. In Figure (8.2.2) are also shown spectra of the OH bending and OH stretching vibrations arising from the multiple-minima approach. Each excitation was estimated by tailoring the reference state $\left|\chi\right\rangle$ according with Eq. (4.3.2) and the Multiple Coherent State approach. We observe that it can happen that, because of a strong interaction between modes, more than one peak can appear in the spectra, as happens for the spectrum of mode 10 showing a second peak close in energy to the signal of mode 9, and for the overtone signal of mode 7 showing a peak at frequency close to mode 12. Finally, we also find a reasonable agreement between DC SCIVR and experiment in the overtone region of the spectra.

8.3 Water trimer

We now look at vibrational features of the water trimer. It has three OH bending vibrations and six OH stretches. Following the same procedure reported above in the dimer

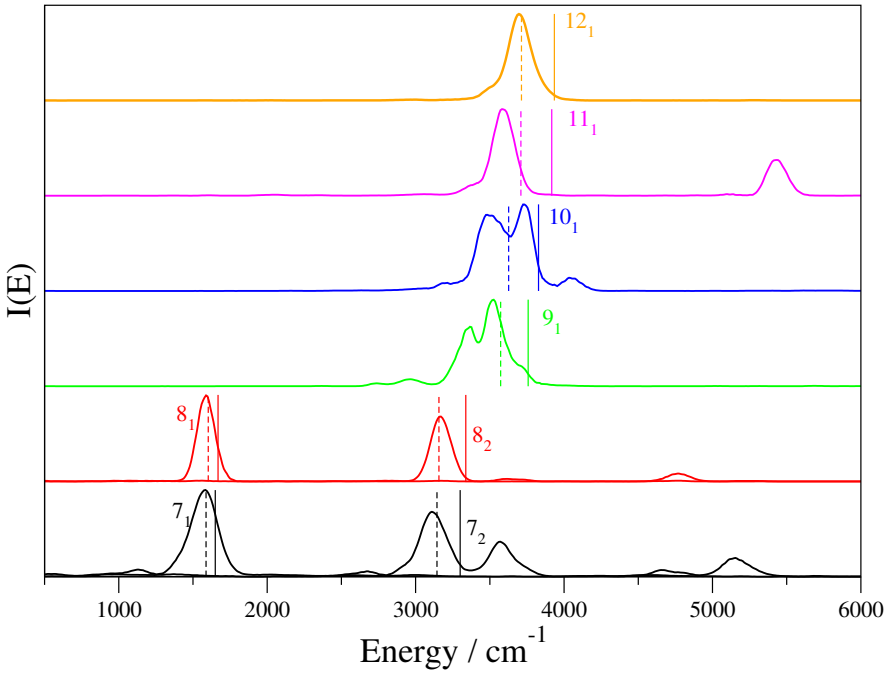

Figure 8.2.2: Vibrational spectra of the water dimer. the solid lines refer to MC-DC-SCIVR calculations with only 5 trajectories run for each subspace; vertical solid lines indicate the harmonic estimates. The bending fundamental and overtone signals were obtained by tuning the reference state according to Eq. (4.3.2).

section, we employed the Hessian method to partitionate the full-dimensional space. We find that the interaction network is less crowded, and definite spectra can be recovered by selecting maximum subspace dimensionality equal to three. The value of threshold parameter chosen for the calculations is $\varepsilon = 1.5 \cdot 10^{-5}$. The nine OH bending and stretching vibrations are divided as follow. Modes 16 and 20 are enrolled in a bi-dimensional subspace, while modes 17,18, and 19 in a three-dimensional one. The remaining modes are instead separated in mono-dimensional subspaces. We calculated vibrational spectra by employing DC SCIVR and sampling 10000 trajectories for each subspace, and MC DC SCIVR using single trajectories. Table (8.2) reports the computed energy levels compared with MultiMode and LocalMonomer ones. Once again the single trajectory implementation leads to poorly accurate results, while in the case of DC SCIVR$_{10k}$ the MAE is quite high but accettable (54 cm^{-1}). Once again, we looked for other relevant local minima on the PES, and we found other nine different from the global one. We repetead the MC-DC

Table 8.2: Vibrational frequencies of the water trimer. Labels are the same as in Table (8.1). Last column indicate classical-like estimates arising from Fourier transform ov velocity-velocity correlation function according to Eq. (8.1.3). MAE values are relative to the benchmark MultiMode (MM) results. Values are reported in cm^{-1}.

Index	HO	MM[91]	LMM[91]	DC SCIVR$_{10k}$	MC-DC SCIVR$_{10trajs,multmin}$	MC-DC SCIVR$_{1\ traj}$	FT$_{C_{VV}}$
13_1	1661	1597	1602	1584	1575	1534	1520
14_1	1664	1600	1614	1595	1637	1528	1520
15_1	1681	1623	1615	1627	1634	1530	1516
16_1	3664	3486	3489	3440	3386	3426	3536
17_1	3703	3504	3500	3450	3400	3547	3548
18_1	3711	3514	3510	3247	3380	3151	3480
19_1	3911	3709	3718	3640	3610	3706	3676
20_1	3916	3715	3718	3700	3675	3652	3697
21_1	3918	3720	3719	3736	3760	3684	3640
MAE	151	-	6	54	65	88	58

SCIVR simulations, by sampling 10 trajectories for each subspace, obtaining a significant increment of accuracy, *i.e.* the MAE moves from 88 cm^{-1} to 65 cm^{-1}. By looking at Figure (8.3.1), we can observe that some modes, in particular modes 16, 17, 18 appear as strongly red-shifted with respect to both harmonic and LocaMonomer ones. To understand why our method displays these discrepancies we calculated an histogram of the O-H and O...H distances between adjacent water molecules, which are the responsibible of lower energetic OH stretches. Figure (8.3.2) shows that modes 16, 17, 18 present significant tails at higher OH and lower O...H distances, as these modes were more affected by hydrogen bonding. In this evenience it is expected a bond weakining and consequently a frequency red-shift, probably enhanced because of the dynamics based method. We observe, that mode 18 is the most red-shifted and it shows the most important tails. On the opposite modes 19, 20, 21 seem to be less affected by hydrogen bonding, showing higher frequencies in the common region of free OH stretches. Furthermore, if we now compute the deviation from MultiMode levels for modes not affected by hydrogen bonding, we find an excellent agreement for both DCSCIVR$_{10k}$ and MC-DCSCIVR$_{multimin}$, with MAE equal to 20 cm^{-1} and 40 cm^{-1} respectively. Finally, in Table (8.2) we also reports vibrational estimates arising from Fourier transform of a classical velocity-velocity correlation

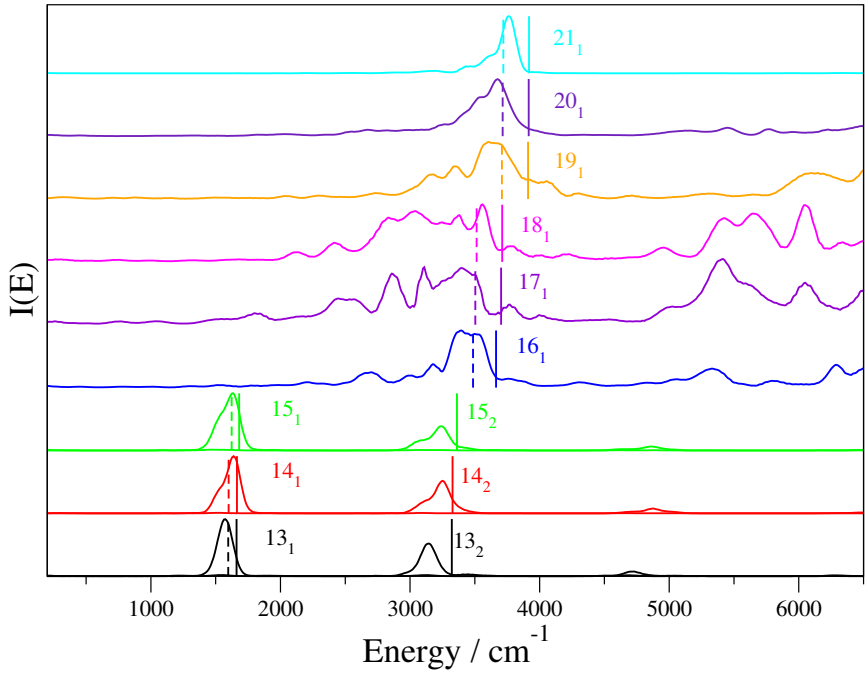

Figure 8.3.1: Vibrational spectra of the water trimer. the solid lines refer to MC-DC-SCIVR calculations with only 10 trajectories run for each subspace; vertical solid lines indicate the harmonic estimates. The bending fundamental and overtone signals were obtained by tuning the reference state according to Eq. (4.3.2).

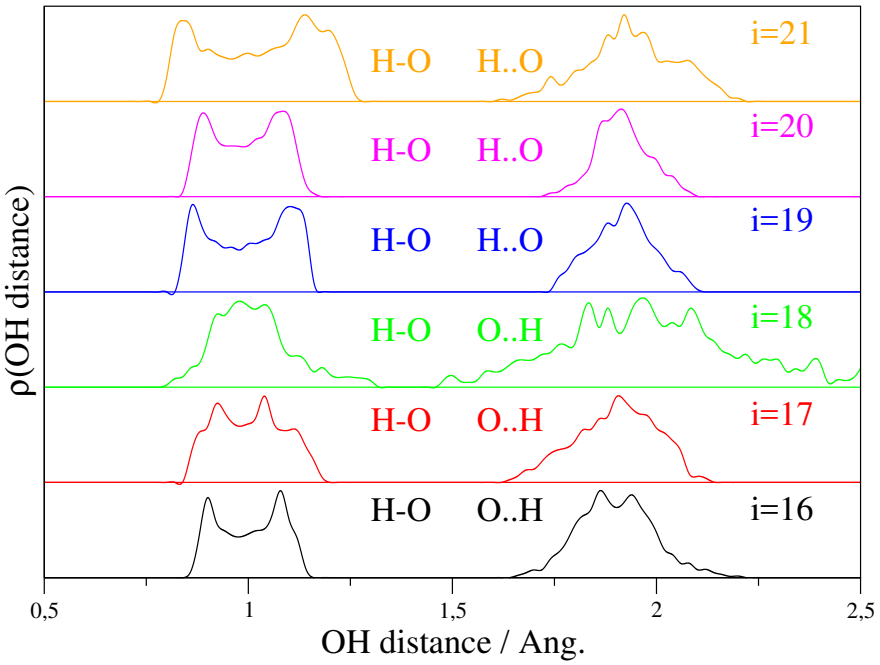

Figure 8.3.2: OH distance trend for the water trimer. OH distances are reported with different colors and are associated to the normal modes reported on the right. On the left is shown the trend of OH distance of bounded hydrogen and oxygen atoms, while on the right the plot relies to the O..H distance between the oxygen and hydrogen atoms of adiacent water molecules.

Table 8.3: Calculated vibrational estimates compared with available experimental levels. Experimental data are not assigned to a specific vibrational mode, so for each theoretical approach the closest frequency has been chosen for comparison. Labels are the same as in previous Tables. MAE is the mean absolute error referred to experimental data. Values are reported in cm^{-1}.

	Exp.[151, 146]	MM[91]	LMM[91]	DC SCIVR$_{10k}$	MC-DC SCIVR$_{10trajs,multmin}$	$FT(C_{vv})$
	1608	1597	1602	1584	1575	1520
	1609	1600	1614	1595	1637	1520
	1629	1623	1615	1627	1634	1516
	3533	3514	3510	3640	3610	3536
	3726	3720	3719	3736	3760	3697
MAE	-	10	11	31	35	64

function, as reported in Eq. (8.1.3), to investigate if the strong red-shift can be regained even in a classical picture. For modes 16-18 the red-shift seems to be less prominent than DC SCIVR, while the three OH bending vibrations are substantially red-shifted with respect to DC SCIVR, MultiMode, and LocalMonomer ones. As expected, no evidences of overtone excitations can be found in classical-like spectra. Finally, in Table (8.3) we compare our DC SCIVR with available experimental data, finding a good agreement (MAE = 31 cm^{-1}), within the typical semiclassical range of accuracy. On the opposite, classical estimates are off-the mark in the bending region, that is instead very well reproduced by DC SCIVR.

8.4 Water hexamer

After looking at lower dimensional clusters as the dimer and the trimer, we now look at the water hexamer prism. It presents 48 vibrational degrees of freedom, 18 of which are OH bending and stretching motions. We observe by looking at the connections network that, similarly to the dimer and trimer, it is less intense and the with same threshold value employed in the trimer cases, all modes should be enrolled in mono-dimensional subspaces with exception on modes 35 and 45. We evolved 5000 classical trajectories per subspace, instead of 10000, because of the high computational demand. However, as we already ob-

Table 8.4: Vibrational frequencies of the water hexamer prism. The labels are the same of Table (8.2). The MC-DC-SCIVR simulation based on 11 trajectories has been performed upon selection of 10 local minima from the correlation distribution. MAE values are referred to the LMM benchmark. Frequency are reported in cm^{-1}.

Index	HO	LMM[91]	DC SCIVR$_{5k}$	MC-DC SCIVR$_{11trajs,multmin}$	MC-DC SCIVR$_{single\ traj}$
31_1	1661	1606	1617	1602	1606
32_1	1672	1612	1623	1620	1592
33_1	1676	1620	1622	1622	1588
34_1	1701	1633	1664	1636	1682
35_1	1715	1654	1661	1640	1684
36_1	1739	1677	1715	1712	1722
37_1	3377	3092	2925	2956	3011
38_1	3494	3256	3052	3060	3012
39_1	3619	3372	3182	3168	2940
40_1	3638	3442	3516	3395	3198
41_1	3714	3482	3573	3556	3200
42_1	3735	3521	3640	3616	3500
43_1	3792	3579	3592	3606	3680
44_1	3809	3588	3580	3574	3608
45_1	3827	3630	3678	3650	3602
46_1	3915	3697	3771	3610	3578
47_1	3923	3706	3698	3750	3768
48_1	3925	3728	3677	3712	3700
MAE	169	-	64	57	102

served above, 5000 classical trajectories usually lead to accurate peaks' positions. Once again, DC SCIVR$_{5k}$ are compared with MC-DC SCIVR based on single trajectories calculations. Table (8.4) shows that single-trajectory simulations lead to very high deviations when compared with benchmark Local Monomer (LMM) approximation calculations, while the agreement is much better between DC SCIVR and LMM, especially in the OH bending and free OH stretching regions. Following the procedure explained above, we explored the PES to look for other relevant local minima by running damped dynamics, by scaling the velocities at each time-step by a factor equal to 0.99. Differently from the previous applications, because of the high-dimensionality, a very high number of possible structures is possible making no advantageous the multiple-minima approach with respect to sampling classical trajectories using a Gaussian distribution function. Because of it, we

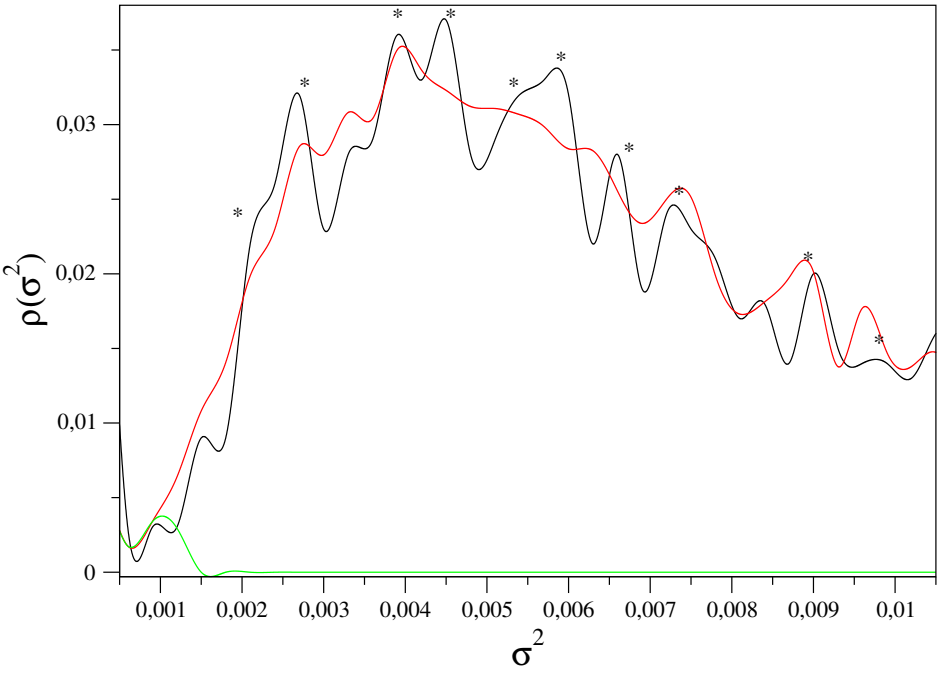

Figure 8.4.1: Correlation distribution between the global minimum and the local minima found by exploring the hexamer many-body PES. The plots report the results for 1,000 (black) and 10,000 (red) damped-dynamics trajectories. Data have been interpolated by means of a cubic spline. The black asterisks represent the correlation peaks corresponding to the minima employed in the MC-DC-SCIVR calculations.

took insight from a recent work, and we looked for the most "correlated" local minima with the global one. The correlation between minima is calculated as a structural quantity. In particular, a correlation parameter (σ^2) is introduced as a function of a set of atomic distances $\{d_i\}_{i=1,\ldots,N_{distances}}$. It is computed as

$$\sigma^2 = \sum_{i=1}^{N_{distances}} (d - d_i^{ref})^2, \tag{8.4.1}$$

where in our calculations we consider all the distances between bounded OH and adjacent OO. d^{ref} describes the reference set of distances, equal to the ones of the global minimum. Now, highly correlated minima are expected to show high values of σ^2, while non-correlated minima should have $\sigma^2 \to 0$. Figure (8.4.1) shows a correlation distribution, where we considered values of σ^2 within 0.011, which is enough to account for 80% of the total number of minimum structures explored by the damped dynamics. Peaks in

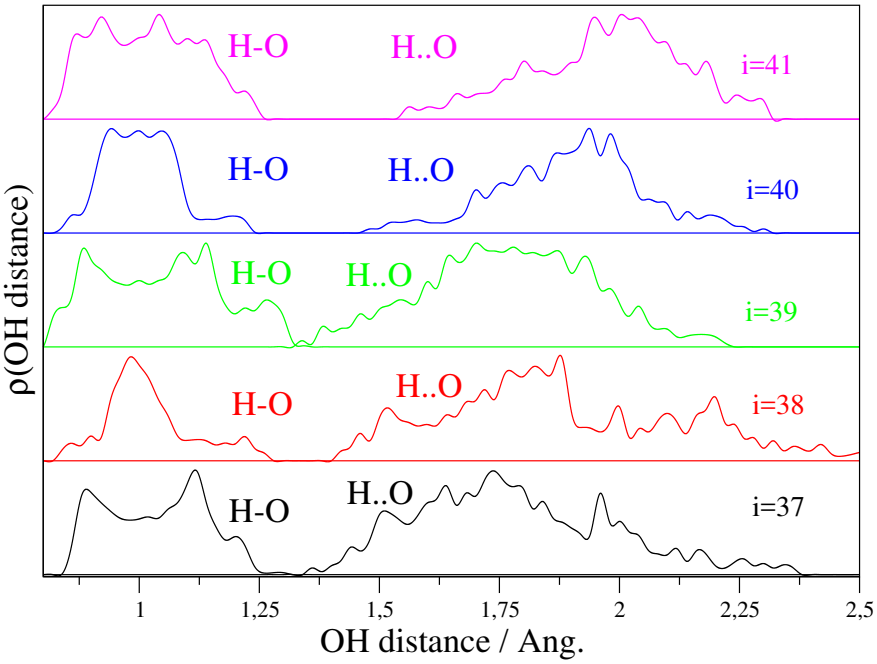

Figure 8.4.2: OH distance trend for the water haxamer. OH distances are reported with different colors and are associated to the normal modes reported on the right. On the left is shown the trend of OH distance of bounded hydrogen and oxygen atoms, while on the right the plot relies to the O..H distance between the oxygen and hydrogen atoms of adjacent water molecules.

the distribution are chosen as starting configurations for MC-DC SCIVR multiple-minima calculations. When 11 minima are considered for MC-DC SCIVR, results strongly improve reaching a Mean Absolute Error similar to the DC SCIVR one, obtained by sampling 5000 classical trajectories for each subspace. Table (8.4) shows the computed energy levels compared with Local Monomer (LMM) approximation calculations; we see that same OH stretching vibrations appear as strongly red-shifted beeing located in the 2900-3100 cm^{-1} energy range. This modes, labelled by 37, 38, 39 seems to be strongly affected by hydrogen bonding. This picture is also consistent with Figure (8.4.2) showing the histogram of OH distances, we see that for modes 37-39 more relevant tails are present at higher OH and lower O...H distances, with respect to modes 40-41, that indeed show a less intense red-shift in the spectra. Similarly to the trimer case, if we consider only OH bending and free OH stretching energy levels, the agreement between DC SCIVR and LMM increases, and the MAE shifts from 64 cm^{-1} to 25 cm^{-1} for DC SCIVR and from 57

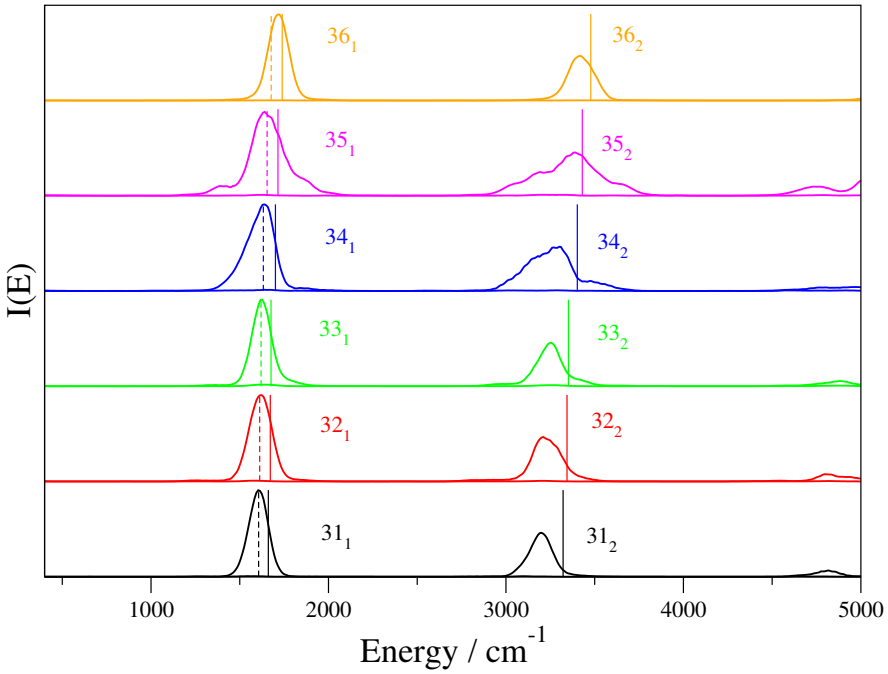

Figure 8.4.3: Vibrational spectra of the water hexamer in the OH bending region. The solid lines refer to MC-DC-SCIVR calculations with only 11 trajectories run for each subspace; vertical solid lines indicate the harmonic estimates. The bending fundamental and overtone signals were obtained by tuning the reference state according to Eq. (4.3.2).

cm^{-1}to 22 cm^{-1} for MC-DC SCIVR$_{\text{multimin}}$. Figure (8.4.3) shows the MC-DC SCIVR$_{\text{multimin}}$ spectra in the OH bending region, while figures (8.4.4) and (8.4.5) the spectra in the OH stretching regions. Vibrational spectra of OH bending and free OH stretches are very well resolved, while the hydrogen bonded OH vibrations display more complex features probably due to interaction with bending overtones excitations, which are located close in energy, and because of strong intermode coupling. This is evident for instance by looking the spectra of modes 39 and 40 showing double peaks, or for modes 41, 42, which also show a shoulder at the frequency of mode 37.

In summary, vibrational estimates of the water hexamer prism are in good agreement with the benchmark LMM ones, especially in the OH bending and free OH stretching regions, while a more intense red-shift is found for hydrogen-bonded OH stretches. More-

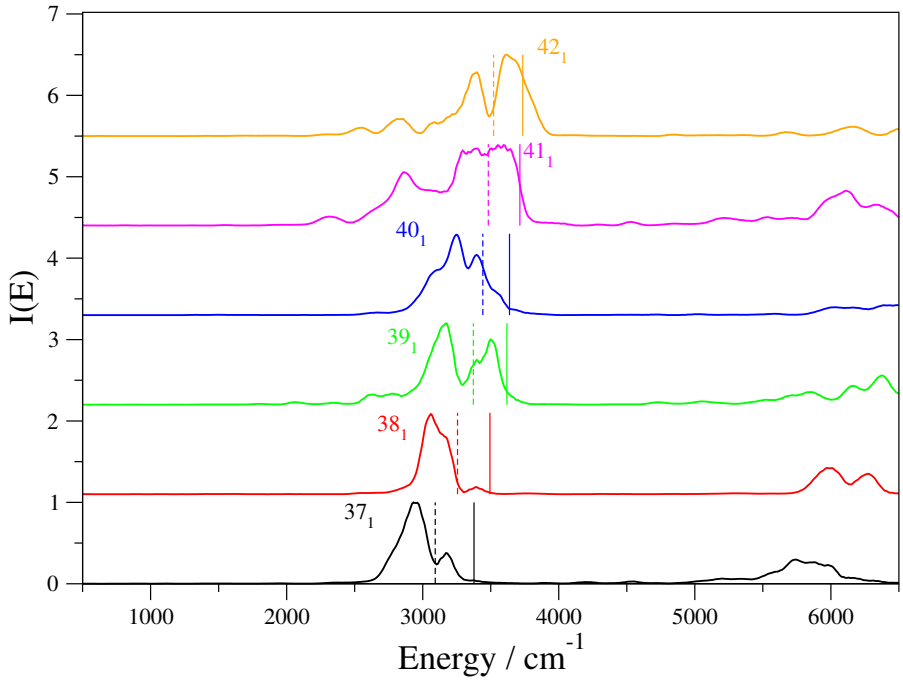

Figure 8.4.4: Vibrational spectra of the water hexamer in the hydrogen-bonded OH stetching region. The solid lines refer to MC-DC-SCIVR calculations with only 11 trajectories run for each subspace; vertical solid lines indicate the harmonic estimates.

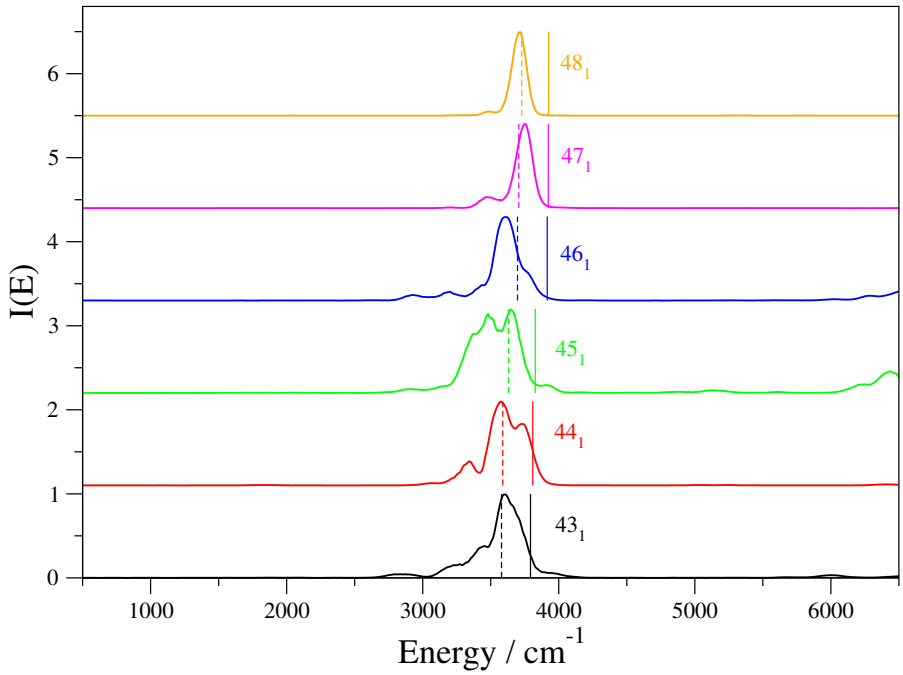

Figure 8.4.5: Vibrational spectra of the water hexamer in the free OH stetching region. The solid lines refer to MC-DC-SCIVR calculations with only 11 trajectories run for each subspace; vertical solid lines indicate the harmonic estimates.

over, the MC-DC SCIVR$_{\text{multimin}}$ results based on 11 trajectories simulations are comparable with DC SCIVR ones based on 5000 trajectories per subspace. This opens up the possibility to move further with higher dimensional clusters, as the decamer, for which the calculation of thousand trajectories would be out of reach.

8.5 Water decamer

We now perform DC-SCIVR simulations focusing on the water decamer, a system made by 84 degrees of freedom. Semiclassical estimates were performed employing monodimensional subspaces, and using the multi-minima approach described in the previous section, because of the high computational demand. Ten minima chosen by sampling 1000 damped dynamics with the same damping factor used for smaller clusters. Figure (8.5.1) shows the correlation distribution calculated using Eq. (8.4.1), where we considered all OH distances between bounded atoms, and OO distances between adjacent oxygen atoms. Table (8.5) shows the computed DC SCIVR energy levels compared with available local monomer approximation results. Results are in good agreement, especially in OH bending and free OH stretching regions, with and average deviation equal to 36 wavenumbers. Once again, OH stretching vibrations are located in three main regions due to free stretches, hydrogen bonded, and strongly hydrogen bonded ones. Moreover, both DC SCIVR and LMM provide more red shifted levels when compared with the water hexamer. Nevertheless, the discrepancy between DC SCIVR and LMM values in the 3000-3200 cm^{-1} region seems to be attenuated with respect to the previous cluster.

8.6 Summary

We have presented here an application of the Divide-and-Conquer method on water clusters of increasing dimensionality. By overall, DC SCIVR estimates for OH bending and

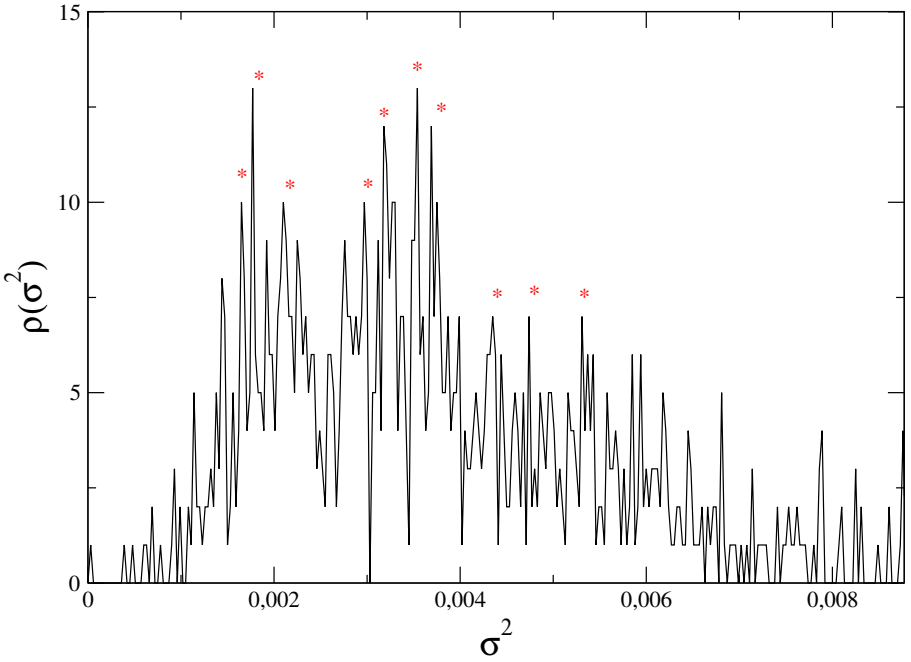

Figure 8.5.1: Correlation distribution between the global minimum and the local minima found by exploring the decamer many-body PES. The plots report the results for 1,000 damped-dynamics trajectories. The red asterisks represent the correlation peaks corresponding to the minima employed in the MC-DC-SCIVR calculations.

Table 8.5: Vibrational frequencies of the water decamer. Labels are the same of Tables (8.1), (8.2), (8.4). All values are reported in cm^{-1}.

HO	LMM[91]	MC-DC-SCIVR$_{11\ trajs,\ multmin}$	HO	LMM[91]	MC-DC-SCIVR$_{11\ trajs,\ multmin}$
1670	1600	1590	3571	3382	3337
1675	1602	1624	3659	3417	3379
1678	1608	1624	3666	3419	3400
1686	1609	1628	3676	3420	3406
1692	1617	1660	3682	3429	3448
1712	1647	1663	3727	3518	3492
1713	1664	1674	3741	3525	3496
1720	1665	1690	3756	3534	3522
1738	1669	1708	3774	3566	3532
1748	1691	1714	3781	3568	3565
3335	3013	2936	3914	3706	3640
3352	3036	3006	3920	3734	3668
3383	3046	3022	3924	3736	3672
3387	3050	3052	3925	3741	3680
3554	3286	3121	3926	3744	3800

free OH stretching vibrations are in very good agreement with benchmark MM and LMM ones. For the hydrogen bonded OH stretches we found a more intense red-shift, probably due to the dynamics nature of the method. This effect was more pronounced for the trimer and the hexamer, while the agreement between LMM and DC SCIVR in the decamer case was more strict. As a general feature, spectra are highly sensitive to the strong intermode coupling, resulting into a peaks' broadening. Furthermore, the high number of floppy motions generate a significant vibrational angular momentum, which contributes to increase peaks' width. This application also shows that the approximate MC-DC SCIVR approach retains good accuracy opening the way toward the application of the method on larger clusters, for which the standard DC SCIVR would be out of reach, because of the high number of trajectories required to converge the phase-space integration.

Chapter 9

$(Gly)_2 H^+$ vibrational features by means of DC SCIVR

9.1 Introduction

We now investigate the vibrational features of protonated glycine dimer $(Gly)_2 H^+$. It has 21 atoms, for a total of 57 vibrational degrees of freedom. Within the semiclassical approach, such an high dimensionality needs a Divide-and-Conquer semiclassical treatment. Protonated glycine dimer presents three main and independent minima that are reported in Figure (9.1.1).

Figure 9.1.1: CS01, ZW01 and CS02 minima of protonated glycine dimer. The left side of the panel shows the CS01 structure, the central one its zwitterionic version ZW01, and below is reported the CS02 local minimum.

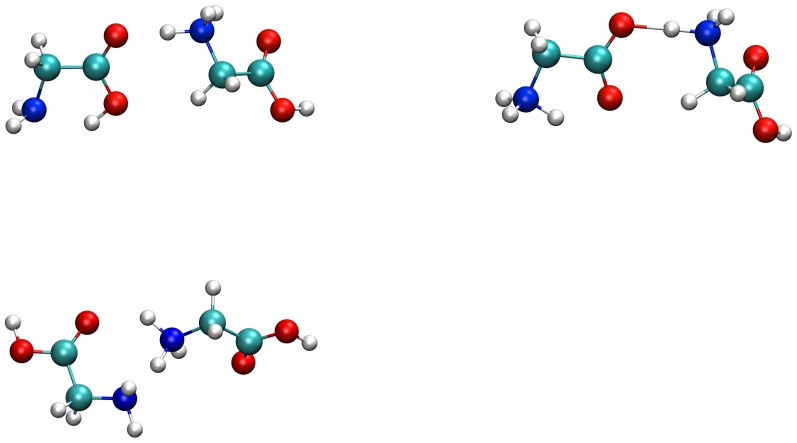

CS01 is the global minimum, while ZW01 is the corresponding zwitterionic structure. CS02 is instead a local minimum in which the interaction network between the two glycine monomers is different from CS01 and ZW01. In the past years this molecule was the focus of many works, with the aim of providing a conclusive assignment at which is the main conformer contributing to the experimental spectrum. Usually, high level experimental techinques as Infrared Multiple Photon Dissociation Spectroscopy (IRPMD) were combined with theoretical estimates relying to scaling approaches of the harmonic frequencies. In some cases experimental features were appointed to CS02 when compared with scaled frequencies,[182] while in other ones, the spectrum was assigned to CS01.[183] This ambiguity was mainly due to the comparison with scaled harmonic frequencies, whose arise by a too crude approach that neglects anharmonicities, and in general any contribution arising from the exploration of regions of the space far from the equilibrium geometry. For these reasons a conclusive attribution of the spectral features to the proper isomer is still missing today. Our reference experimental spectrum come from the works of McLafferthy and co-workers,[182] and McMahon and co-workers[183]

groups.

In the first, the spectrum was recovered in the high frequency region, from 3000 to 3700 cm^{-1}, *i.e.* only in the CH, NH, and OH stretching region. The theoretical assignment to the isomer was done by computing the harmonic frequencies of CS02 at a B3LYP/6-31G(d) level of theory, and introducing a scaling factor, equal to 0.97. In the other work the frequencies were computed at B3LYP/6-311+G(d,p) level of theory and then scaled by a factor equal to 0.985. They recovered the spectrum in the 1000-2000 cm^{-1} spectral region. With their scaling factor value, they found that the best spectrum is the one of CS01, which is the global minimum at B3LYP/6-311+G(d,p). The highest energetic spectral window 3000-3700 $cm^{-1}$was reproduced introducing a further scaling factor, *i.e* 0.96.

We think that the harmonic approximation is definitely insufficient to describe such complex systems. The harmonic estimates can be extremely sensitive to the scaling factor value, and different regions of the spectrum require different values of the scaling factor. Thus, an alternative approach without any arbitrary scaling factors is needed. Our divide-and-conquer semiclassical method looks like a possible solution.

We perform DC SCVIR semiclassical calculations on the isomers introduced before. Since no potential energy surfaces are available, the nuclei potential is evaluated ab-initio employing the NWCHEM package[184] at the same level of theory of McMahon and co-workers,[183] and we compare our results with experimental data, with the aim of providing which is the main conformer contributing to the experimental spectrum.

9.2 AIMD with NWCHEM

We perform *ab-initio* molecular dynamics simulations employing NWCHEM package[184] at a DFT B3LYP/6-311+G(d,p) level of theory.[185] Since we are looking for semiclassical vibrational frequencies we set the initial conditions $(\mathbf{p}_0, \mathbf{q}_0)$ of the classical trajectories

equal to $(\mathbf{p}_{eq}, \mathbf{q}_{eq})$ where $\mathbf{q}_{eq}$ is the equilibrium geometry of the isomer under investigation, while $\mathbf{p}_{eq}$ is the collections of momenta following an harmonic fashion $\frac{\hbar\omega_i}{2} = \frac{p_i^2}{2m}$, leading to a trajectory with energy equal to the harmonic Zero Point Energy. Due to the high computational demand of the calculation we set the dynamics length equal to 25000 atomic units, since it was showed to be enough to recover very accurate and nearly converged vibrational levels for glycine based molecules.[76] We run 3 classical trajectories, each one centered at the equlibrium configuration of a relevant isomer. We also employ the proper NWCHEM module in order to keep approximately equal to zero the total angular momentum and its components. According with the literature, the zwitterionic isomer very quickly interconverts into the global minimum CS01, in agreement with the literature consensus about its negligible contribution to the vibrational spectrum. Figure (9.2.1) shows the OH (black line) and NH (red line) distances during the dynamics of ZW01. We observe that the OH distance starts oscillating from the equilibrium one for ZW01, but after very short time it drops into the CS01 basin and the distance oscillates around the equilibrium one of CS01 reported with a black horizontal dashed line. A similar behavior is followed by NH distance. Because of it, we perform our semiclassical calculations on CS01 and CS02 which are believed to be relevant in the IRPMD spectrum.

Figure 9.2.1: Plot of NH and OH distances during the dynamics of ZW01. The black line reports the OH distance, while the red line the NH one. Horizontal dashed lines are centered at equilibrium distances for CS01 and ZW01.

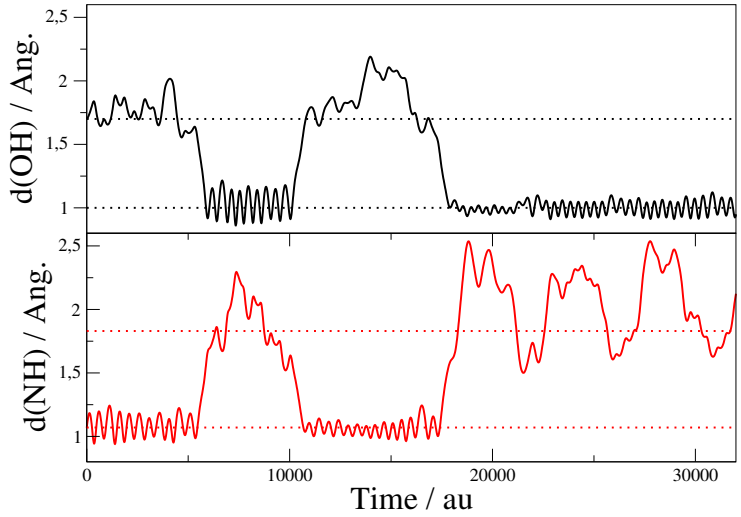

9.3 DC-SCIVR applied on CS01

We separate the 57-dimensional space in order to have a maximum subspace dimensionality equal to 16, which is a reasonable value for the glycine-based systems studied with DC-SCIVR.[186] We employ a threshold value equal to $4.8 \cdot 10^{-6}$ obtaining one 16-dimensional space, one 6-dimensional, one four-dimensional, one three-dimensional, three bi-dimensional, and 22 monodimensional subspaces. Figure (9.3.1) shows a threshold trend where a very quick descreasing of the subspace dimensionality is observed. At max. subspace dimensionality equal to 16 we observe a small flat region.

Figure 9.3.1: Threshold trend in the case of CS01 minimum.

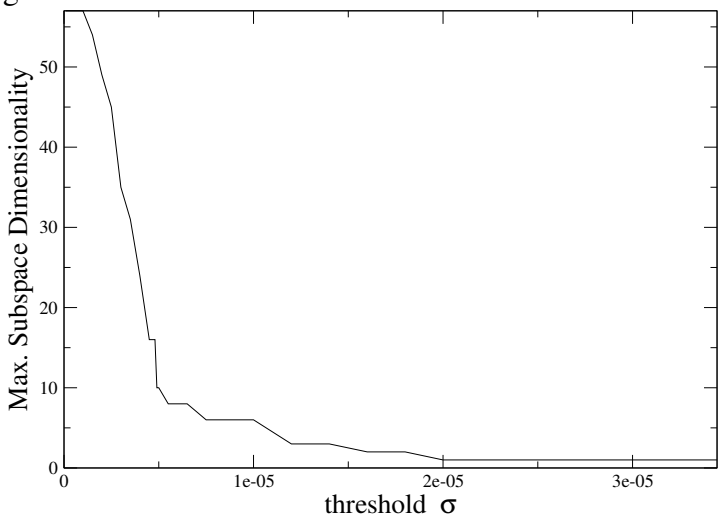

In order to reduce the noisy features we employ a Gaussian filter. The filtering function is $e^{-\alpha t^2}$ with $\alpha = 3 \cdot 10^{-8}$. To reduce numerical instability issues of the classical trajectory we employed in all semiclassical calculations a second order iterative pre-exponential factor approximation. In table (9.1) we report the experimental frequencies compared with our semiclassical and harmonic estimates.

Table 9.1: DC-SCIVR frequencies of CS01 compared with experimental findings and harmonic estimates. The value are reported in cm^{-1}. The experimental levels in the range 1000-2000 cm^{-1} are taken from Ref (183), while the values from 3000-4000 $cm^{-1}$are taken from Ref (182). Last row reports the Mean Average Error (MAE) with respect to the experimental values.

Label	Exp	DC-SCIVR	HO
free OH bending	1191	1172	1192
hydrogen bonded OH bending	1439	1450	1461
Nitrogen umbrella inversion	1523	1511	1570
carbonyl stretching	1757	1750	1756
carbonyl stretching	1808	1804	1811
N^+-H symmetric stretching	3372	3375	3500
free OH stretching	3585	3628	3730
MAE	/	14	50

Table (9.1) shows a good agreement between theory and experiment with dispacements within 20 cm^{-1} and a Mean Average Erorr equal to be only 14 wavenumbers, below the typical semiclassical range of accuracy, 20-30 cm^{-1}. The only exception to this trend is represented by the free OH stretching frequency, shifted by 43 cm^{-1}, that we estimate to be 3628 cm^{-1} while the experimental finding is 3585 cm^{-1}. It is noteworthy to compare our discrepancy with a crude NMA, that estimates the frequency to be very blue-shifted at 3730 cm^{-1}. All computed CS01 frequencies are in excellent agreement with the IRPMD spectrum, giving the first evidences of the strong contribution of this isomer to the experimental spectrum. Figure (9.3.2) provides the partial spectra obtained with our DC-SCIVR method of the modes compared with the experiment. Modes in panel (a) belong to the 16th-dimensional subspace, while modes in panels (b) belong to a three-dimensional subspace. Modes in panel (c) are enrolled in mono-dimensional subspaces. Each excitation is labelled according to its normal mode.

Figure 9.3.2: Vibrational spectra of modes compared with the experiment. The frequencies are cumputed at a DC-SCIVR level of theory. Modes in panel (a) are involved a 16-dimensional space, while modes in panel (b) are enrolled in a three-dimensional space. Modes in panel (c) are enrolled in mono-dimensional subspaces. The vertical lines are centered at the experimental frequencies.

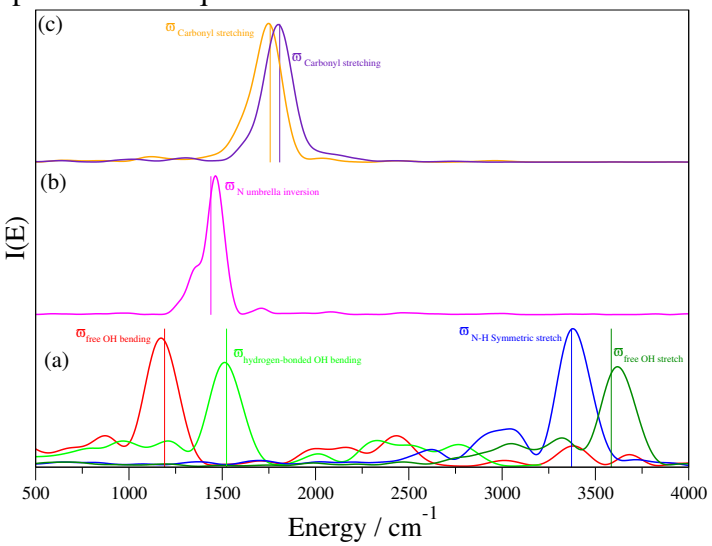

By overall, excellent agreement is found between our CS01 DC-SCIVR frequencies and the experimental ones. In Table (9.2) are reported all computed energy levels in the range 1000-4000 cm^{-1}.

Table 9.2: Vibrational frequencies of CS01 isomer reported in cm^{-1}.

Mode	DC-SCIVR	HO	Exp	Mode	DC-SCIVR	HO	Exp	Mode	DC-SCIVR	HO	Exp
26	1003	1020		37	1386	1435		48	2959	3059	
27	1074	1075		38	1344	1443		49	2987	3084	
28	1108	1133		39	1450	1461	1439	50	2966	3101	
29	1109	1159		40	1434	1485		51	3051	3142	
30	1174	1178		41	1511	1570	1523	52	3197	3191	
31	1172	1192	1191	42	1629	1669		53	3243	3309	
32	1188	1246		43	1633	1675		54	3375	3498	3372
33	1267	1315		44	1641	1686		55	3415	3537	
34	1340	1338		45	1750	1756	1757	56	3435	3609	
35	1320	1339		46	1804	1811	1808	57	3628	3730	3585
36	1320	1351		47	2658	2707		MAE	14		

Last, to better appreciate the reliability of our results with respect to crude harmonic estimates, we report in Figure (9.3.3) the experimental spectrum compared with scaled

harmonic frequencies and semiclassical ones.

Figure 9.3.3: Experimental spectra (black line) compared with scaled harmonic estimates of CS01 (vertical red lines), scaled harmonic estimates of CS02 (vertical green lines), semiclassical estimates of CS01 (vertical blue lines), and semiclassical estimates of CS02 (vertical magenta lines). The harmonic frequencies are scaled with a factor equal to 0.985. The intensity of semiclassical estimates is equal among all of them since they come from power spectra calculations. The experimental spectrum at the left of panel, *i.e.* 1000-2000 cm^{-1} comes from Ref (183), while the spectrum from 3000-4000 cm^{-1} is taken from Ref (182).

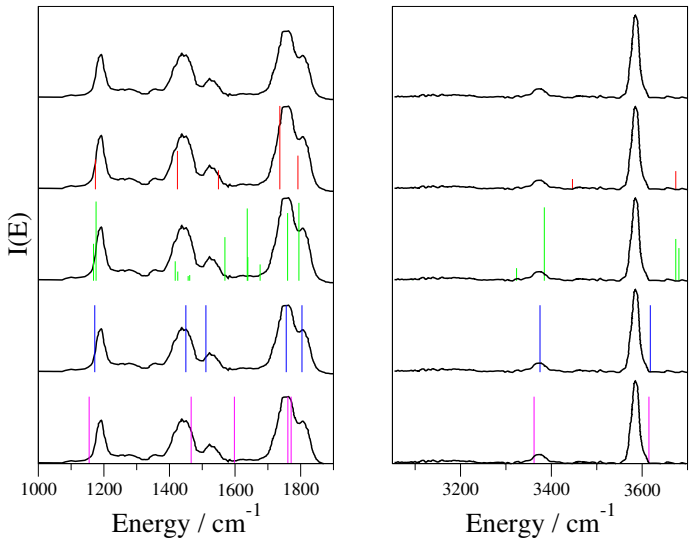

By Looking at scaled harmonic frequencies, it can be only hypothized the contribution of CS01, since the estimates are sometimes close to the experiment in the 1000-2000 cm^{-1}, while they are definitely out of consideration in the 3000-4000 cm^{-1}region. If ones looks instead at semiclassical estimates, which intrinsicaly accounts for quantum anharmonities, the picture appears much more clear, with an excellent matching between semiclassical CS01 and experimental energy levels in the whole energy range. A tentative improvement of the scaled harmonic estimates in the 3000-4000 cm^{-1} region can be done by employing a "more anharmonic" scaling factor equal to 0.96. In the last case, depicted in Figure (9.3.4) the agreement is very good in the highest energy region, but unfortunately the region 1000-2000 cm^{-1} is badly reproduced.

Figure 9.3.4: Experimental spectra (black line) compared with scaled harmonic estimates of CS01 (vertical red lines), scaled harmonic estimates of CS02 (vertical green lines), semiclassical estimates of CS01 (vertical blue lines), and semiclassical estimates of CS02 (vertical magenta lines). The harmonic frequencies are scaled with a factor equal to 0.96. The intensity of semiclassical estimates is equal among all of them since they come from power spectra calculations. The experimental spectrum at the left of panel, *i.e.* 1000-2000 cm^{-1} comes from Ref (183), while the spectrum from 3000-4000 cm^{-1} is taken from Ref (182).

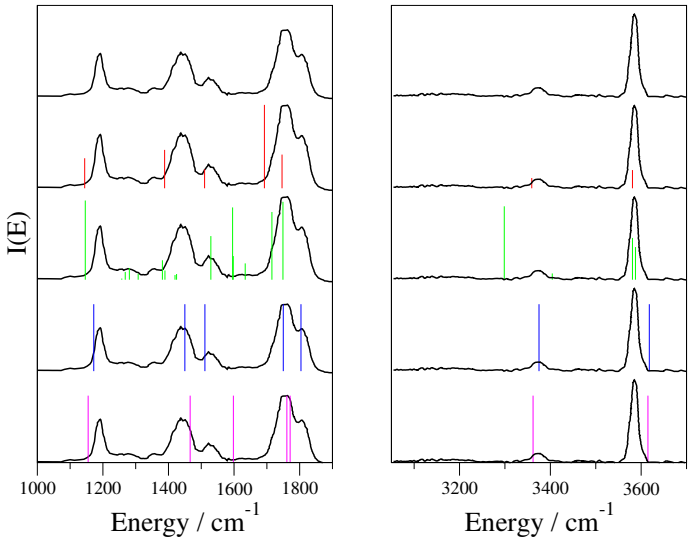

As an overall result, from one side the harmonic estimates are very sensitive to the scaling factor, and can not reproduce accurately the whole spectral range, but only reduced region of the spectrum, while semiclassical estimates intrinsicaly account for quantum anharmonity and can be compared with experimental data in the whole spectral window.

9.4 DC-SCIVR applied on CS02

We separate the 57-dimensional space in order to have a maximum subspace dimensionality equal to 18. This choice is done according to the threshold trend, reported in Figure (9.4.1), where a flat zone is observed at maximum dimension equal to 18, and to be comparable with the choice done for CS01. The value of the threshold in this case was $5.6 \cdot 10^{-6}$ obtaining one 18-dimensional subspace, one four-dimensional subspace, four bi-dimensional subspaces, and 27 mono-dimensional subspaces.

Figure 9.4.1: Threshold trend in the case of CS02 minimum.

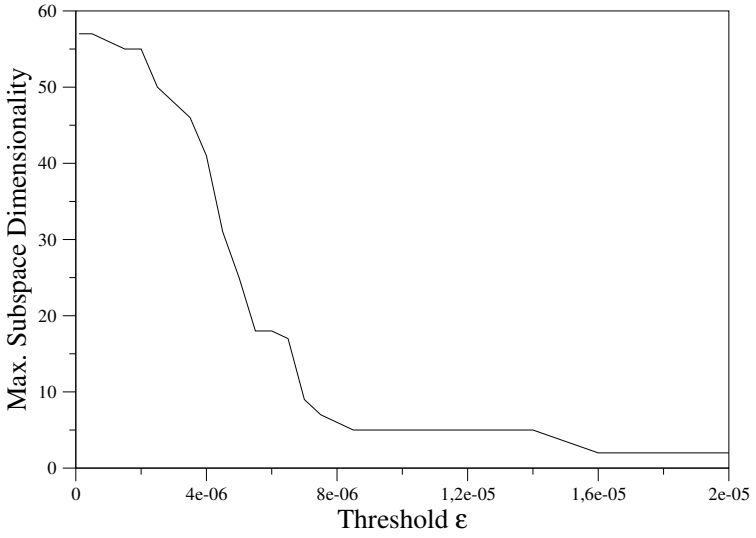

The filtering function of the semiclassical integrand is the same of CS01, *i.e.* $e^{-\alpha t^2}$ with $\alpha = 3 \cdot 10^{-8}$. In table (9.3) we report the computed DC-SCIVR frequencies compared with experimental and harmonic estimates.

Table 9.3: DC-SCIVR frequencies of CS02 compared with experimental findings and harmonic estimates. The value are reported in cm^{-1}. Last row reports the Mean Average Error (MAE) with respect to the experimental values.

Label	Exp	DC-SCIVR	HO
free OH bending	1191	1155	1202
hydrogen bonded OH bending	1439	1466	1485
Nitrogen umbrella inversion	1523	1598	1665
carbonyl stretching	1757	1771	1784
carbonyl stretching	1808	1761	1817
N^+-H symmetric stretching	3372	3362	3546
free OH stretching	3585	3615	3727
MAE	/	34	79

In this case, the agreement with the experimental features is good only for the high energetic OH and NH stretching region, while the lower energetic excitations are very different from the experimental ones. In particular in the carbonyl stretching region we find two peaks at 1761 and 1771 cm^{-1}, while the splitting in the experiment is much more pronounced, and the levels are located at 1757 and 1808 cm^{-1}. Most importantly, in the experiment a peak is present at 1523 cm^{-1}, conversely in this region the DC-SCIVR level

is located quite far at 1598 cm^{-1}. The signal at 1598 cm^{-1} is mainly due to the bending motion of NH_2 group of neutral glycine. Figure (9.4.2) shows that the agreement between CS02 and the experiment is less strict with respect to CS01 and the mean deviation is 32 cm^{-1}. In Table (9.4) are reported all computed energy levels above 1000 cm^{-1}.

Table 9.4: Vibrational frequencies of CS02 isomer reported in cm^{-1}.

Mode	DC-SCIVR	HO	Exp	Mode	DC-SCIVR	HO	Exp	Mode	DC-SCIVR	HO	Exp
25	1033	1036		36	1341	1362		47	2714	2707	
26	1015	1054		37	1382	1438		48	2979	3048	
27	1050	1091		38	1421	1447		49	2975	3086	
28	1095	1117		39	1463	1479		50	2988	3087	
29	1106	1156		40	1452	1485		51	3007	3138	
30	1138	1186		41	1466	1593	1439	52	3171	3359	
31	1106	1194		42	1617	1662		53	3185	3431	
32	1155	1202	1191	43	1598	1665	1523	54	3316	3481	
33	1255	1305		44	1610	1700		55	3362	3546	3372
34	1295	1319		45	1771	1784	1757	56	3615	3727	3585
35	1362	1334		46	1761	1817	1808	57	3640	3734	

Finally, Figure (9.4.2) reports the experimental spectrum against the DC-SCIVR one of CS01 and CS02. Although the DC-SCIVR features are sometimes broad, we observe that panels (a) and (b) are very well in agreement in the whole experimentally accessible energy range, giving insights about the CS01 contribution to the experimental spectrum.

Figure 9.4.2: Experimental spectra in panel (b) compared with DCSCIVR spectrum of CS01 in panel (a) and DC-SCIVR spectrum of CS02 in panel (c). The experimental spectrum in the 1000-2000 cm^{-1} region comes from Ref (183), while the spectrum from 3000-4000 cm^{-1} is taken from Ref (182).

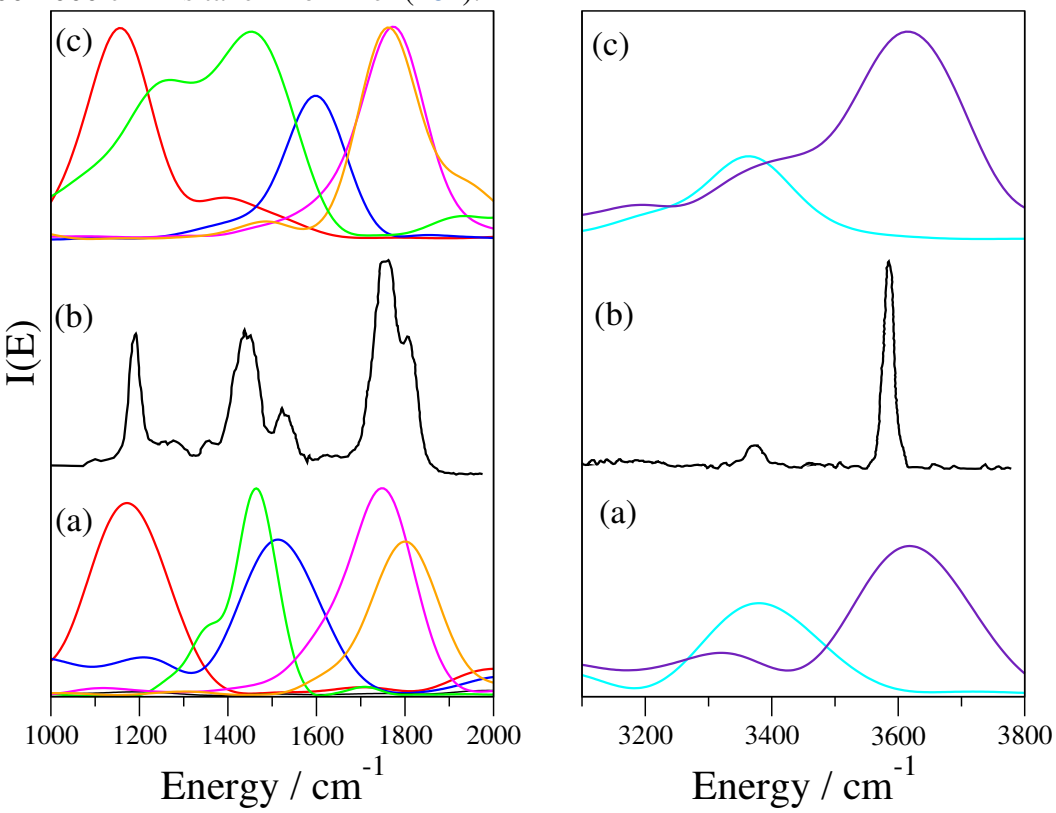

9.5 Summary

The vibrational investigation on CS01 and CS02 isomers suggests that CS01 maybe the most contributing isomer to the experimental spectrum. In particular, if from one side the high-frequency fundamentals well fit the experimental positions, in the mid-frequency region the picture is different. In the case of CS01 the agreement is strict while relevant deviations in CS02 simulated spectrum were found. For instance only in the CS01 the two carbonyl stretches are significantly separated in energy, and the experimental peak at 1523 cm^{-1}has a counterpart only for CS01 (1511 cm^{-1}).

Chapter 10

Conclusions

In this thesis advances of the Time Averaging Semiclassical Initial Value Represention (TA-SCIVR) approximation to the spectral density of molecular systems have been presented. In particular, the goal of the thesis was to overcome two limitations of the theory, the first one concerning the numerical instability of the pre-exponential factor, in the event of chaotic trajectories, whose often characterize high-dimensional and complex molecules. The second one was the so-called "curse of dimensionality" problem, in which the method (TA-SCIVR) runs out of steam when the systems' dimensionality overcome 25-30 degrees of freedom.

To address the first issue, numerical and analytical approximations to the pre-exponential factor have been developed and tested, showing good stability and retaining accuracy of the spectra. Then, we developed the "Divide and Conquer" method (DC-SCIVR) that allows to overcome the curse of dimensionality problem, and consequently vibrational spectra of high-dimensional molecules can be obtained. Furthermore, the method takes advantage of the same formalism of TA-SCIVR and the very basic idea is to decompose the full-dimensional problem in lower-dimensional ones. In this way, from one side it is possible to deal with large systems, and from the other the computational overhead can be reduced, since lower-dimensional matrices are required instead of the full-dimensional ones. To do that, the semiclassical quantities are projected in subspaces, that are selected by an appropriate method. The original one is based on the hessian matrix, and it is very

computationally cheap but less solid. On the opposide one can employ a methodology, called "Jacobian", based on the conservation of Liouville theorem, that is more demanding but more solid and accurate.

DC-SCIVR has been tested against low- and medium-sized molecules and a negligible loss of accuracy has been observed, especially when combined with the Jacobian-based seek of subspaces. Then, it was applied to study large molecules as benzene and fullerene, and finally it allowed to recover spectra of complex supramolecular systems as water clusters and protonated glycine dimer. Further applications of DC-SCIVR will exploit molecular systems involved in biological and technological processes.

Chapter 11

Appendix

11.1 Derivation of the Herman-Kluk propagator from Van-Vleck

In a one-dimensional problem the probability of going from $\left|\psi_i\right\rangle$ to $\left|\psi_f\right\rangle$ by approximating the quantum propagator using Eq. (3.1.4) is expressed as (assuming $\hbar = 1$)

$$\left\langle \psi_f \middle| e^{-\frac{i}{\hbar}\widehat{H}t} \middle| \psi_i \right\rangle = \iint dq_0 dq_1 \left(2\pi i\hbar \left|M_{qp}\right|\right)^{-\frac{1}{2}} e^{\frac{i}{\hbar}S_t(p_0,q_0)} \left\langle \psi_f \middle| q_1 \right\rangle \left\langle q_0 \middle| \psi_i \right\rangle \quad (11.1.1)$$

where the initial and final wavefunctions can be taken as coherent states.

$$\left\langle q_0 \middle| \psi_i \right\rangle = \psi_i\left(q_0\right) = \left(\frac{\gamma}{\pi}\right)^{\frac{1}{4}} e^{-\frac{\gamma}{2}\left(q_0-q_i\right)^2+\frac{i}{\hbar}p_i\left(q_0-q_i\right)}$$

$$\left\langle \psi_f \middle| q_1 \right\rangle = \psi_f\left(q_1\right)^* = \left(\frac{\gamma}{\pi}\right)^{\frac{1}{4}} e^{-\frac{\gamma}{2}\left(q_1-q_f\right)^2-\frac{i}{\hbar}p_f\left(q_1-q_f\right)}$$

If we now introduce the explicit representation of the wavefunctions into Eq. (11.1.1), we obtain

$$\left\langle \psi_f \middle| e^{-\frac{i}{\hbar}\widehat{H}t} \middle| \psi_i \right\rangle = \iint dq_0 dq_1 \left(2\pi i\hbar \left|M_{qp}\right|\right)^{-\frac{1}{2}} e^{-\frac{\gamma}{2}\left(q_0-q_i\right)^2-\frac{\gamma}{2}\left(q_1-q_f\right)^2}$$

$$\times\, e^{\frac{i}{\hbar}\left[S_t(q_0,q_1)+p_i\left(q_0-q_i\right)-p_f\left(q_1-q_f\right)\right]}. \quad (11.1.2)$$

We now call the exponential part $\phi_t(q_0, q_1)$, where

$$\phi_t(q_0, q_1) = S_t(q_0, q_1) + p_i(q_0 - q_i) - p_f(q_1 - q_f) + \frac{i\hbar\gamma}{2}\left[(q_0 - q_i)^2 + (q_1 - q_f)^2\right]. \tag{11.1.3}$$

The quantum probability can be written now in a more simplified way as

$$\left\langle \psi_f \middle| e^{-\frac{i}{\hbar}\widehat{H}t} \middle| \psi_i \right\rangle = \iint dq_0 dq_1 \left(2\pi i\hbar \left|M_{qp}\right|\right)^{-\frac{1}{2}} e^{\frac{i}{\hbar}\phi_t(q_0,q_1)}. \tag{11.1.4}$$

To solve Eq. (11.1.4) Miller took inspiration from the Filinov filter, briefly described below.[187, 188] Let's take a strongly oscillating integral

$$I = \int dx e^{i\phi(x)} \tag{11.1.5}$$

and add an identity arising from a Gaussian integral

$$1 = \sqrt{\frac{A}{\pi}} \int dx_0 e^{-A(x-x_0)^2}. \tag{11.1.6}$$

Within this trick, the integral becomes apparently more complicated since two integrals have to be solved

$$I = \sqrt{\frac{A}{\pi}} \int\int dx dx_0 e^{-A(x-x_0)^2 + i\phi(x)}. \tag{11.1.7}$$

Things utterly change if we take advantage of a stationary phase approximation, since we expect the integral to be different from zero close to stationary points of the function $\phi(x)$. Expanding the function up to the second order, the integral is approximated as

$$I \sim \sqrt{\frac{A}{\pi}} \int\int dx dx_0 e^{-A(x-x_0)^2 + i\phi(x_0) + i\phi'(x_0)(x-x_0) + \frac{i}{2}\phi''(x_0)(x-x_0)^2}. \tag{11.1.8}$$

Now the integral along the variable x can be analytically solved, obtaining

$$I \sim \sqrt{\frac{A}{\pi}} \int dx_0 \sqrt{\frac{\pi}{A - \frac{i}{2}\phi''(x_0)}} e^{-\frac{\phi'(x_0)^2}{4\left(A - \frac{i}{2}\phi''(x_0)\right)} + i\phi(x_0)}. \tag{11.1.9}$$

Adding the transformation $\frac{c}{2} = \frac{1}{4\left(A-\frac{i}{2}\phi''(x_0)\right)}$, we obtain $\sqrt{\frac{A}{A-\frac{i}{2}\phi''(x_0)}} = \sqrt{1+ic\phi''(x_0)}$ and the oscillating integral becomes

$$I \sim \int dx_0 \sqrt{1+ic\phi''(x_0)} e^{-\frac{C}{2}\phi'(x_0)^2+i\phi(x_0)}, \tag{11.1.10}$$

while its multidimensional expression is

$$I \sim \int d\mathbf{x}_0 \sqrt{det\left(\mathbf{I}+i\mathbf{c}\boldsymbol{\phi}''(\mathbf{x}_0)\right)} e^{-\boldsymbol{\phi}'(\mathbf{x}_0)\frac{\mathbf{C}}{2}\boldsymbol{\phi}'(\mathbf{x}_0)^T+i\phi(\mathbf{x}_0)}. \tag{11.1.11}$$

Eq. (11.1.11) is the approximation of Eq. (11.1.5) in the Filinov filtering fashion. We can now take advantage of the Filinov filter to solve Eq. (11.1.4) (assuming that the Van-Vleck pre-exponential factor is smooth), where $\int dx_0$ is the double integral $\iint dq_0 dq_1$, the arbitrary Filinov parameter is a bi-dimensional matrix, that we choose to be

$$\mathbf{c} = \begin{pmatrix} c_0 & 0 \\ 0 & c_1 \end{pmatrix}.$$

Within the Filinov filtering framework we first have to calculate the first and second derivatives of the phase function $\phi_t(q_0, q_1)$ and then add them into Eq. (11.1.10). The first derivatives of $\phi_t(q_0, q_1)$ are

$$\frac{\partial \phi_t(q_0,q_1)}{\partial q_0} = \frac{\partial S_t}{\partial q_0} + p_i + i\hbar\gamma(q_0 - q_i) = -p_0 + p_i + i\hbar\gamma(q_0 - q_i)$$

$$\frac{\partial \phi_t(q_0,q_1)}{\partial q_1} = \frac{\partial S_t}{\partial q_1} - p_f + i\hbar\gamma(q_1 - q_f) = p_1 - p_f + i\hbar\gamma(q_1 - q_f),$$

while the second derivatives are

$$\frac{\partial^2 \phi_t(q_0,q_1)}{\partial q_0^2} = -\frac{\partial p_0}{\partial q_0} + i\hbar\gamma$$

$$\frac{\partial^2 \phi_t(q_0,q_1)}{\partial q_0 \partial q_1} = -\frac{\partial p_0}{\partial q_1}$$

$$\frac{\partial^2 \phi_t(q_0, q_1)}{\partial q_1 \partial q_0} = \frac{\partial p_1}{\partial q_0}$$

$$\frac{\partial^2 \phi_t(q_0, q_1)}{\partial q_1^2} = \frac{\partial p_1}{\partial q_1} + i\hbar\gamma.$$

We now call the pre-exponential term $\mathbf{c}_f^2(q_0, q_1) = \sqrt{I + i\mathbf{c}\boldsymbol{\phi}''(q_0, q_1)}$, where $\mathbf{c}_f(q_0, q_1)$ denotes a "*Filinov pre-exponential factor*"

$$\mathbf{c}_f^2(q_0, q_1) = \begin{pmatrix} 1 - \gamma c_0 + i c_0 \frac{\partial p_1}{\partial q_1} & i c_0 \frac{\partial p_1}{\partial q_0} \\ -i c_1 \frac{\partial p_0}{\partial q_1} & 1 - \gamma c_1 \frac{\partial p_0}{\partial q_0} \end{pmatrix} \tag{11.1.12}$$

The determinant of the squared Filinov pre-exponential factor is now equal to

$$det\left(\mathbf{c}_f^2(q_0, q_1)\right) = (1 - \gamma c_0)(1 - \gamma c_1) - i c_1 (1 - \gamma c_0) \frac{\partial p_0}{\partial q_0} +$$

$$+ i c_0 (1 - \gamma c_1) \frac{\partial p_1}{\partial q_1} + c_0 c_1 \left(\frac{\partial p_1}{\partial q_1}\frac{\partial p_0}{\partial q_0} - \frac{\partial p_1}{\partial q_0}\frac{\partial p_0}{\partial q_1} \right). \tag{11.1.13}$$

Miller then introduced the IVR transformation to make the expression of determinant more insightful, leading to

$$\iint dq_0 dq_1 \left(2\pi i\hbar |M_{qp}|\right)^{-\frac{1}{2}} \left(det\left(\mathbf{c}_f^2\right)\right)^{\frac{1}{2}} \rightarrow \iint dq_0 dp_0 \left(\frac{|M_{qp}|}{2\pi i\hbar} det\left(\mathbf{c}_f^2\right) \right)^{\frac{1}{2}}, \tag{11.1.14}$$

where $M_{qp} = \frac{\partial q_1}{\partial p_0}$. Now, we rewrite all the terms of the Filinov determinant in order to extrapolate at the denominator $\frac{\partial q_1}{\partial p_0}$ and simplify it with the Van-Vleck pre-exponential factor. The easiest term is $\frac{\partial p_1}{\partial q_1}$ since

$$\frac{\partial p_1}{\partial q_1} = \frac{\partial p_1}{\partial p_0}\frac{\partial p_0}{\partial q_1} == \frac{\partial p_1 / \partial q_1}{\partial q_1 / \partial p_0}. \tag{11.1.15}$$

Then because of Schwartz theorem

$$-i c_1 \frac{\partial p_0}{\partial q_1} = i c_0 \frac{\partial p_1}{\partial q_0}$$

and since c_0 and c_1 can be arbitrarily chosen, we make the choice $c_0 = c_1$ leading to

$$\frac{\partial p_1}{\partial q_0} = -\frac{1}{\partial q_1/\partial p_0}. \tag{11.1.16}$$

Then $\frac{\partial p_0}{\partial q_0}$ can be expressed as

$$\frac{\partial p_0}{\partial q_0} = \left(\frac{\partial p_0}{\partial q_1}\right)\left(\frac{\partial q_1}{\partial q_0}\right) = \frac{\partial q_1/\partial q_0}{\partial q_1/\partial p_0}, \tag{11.1.17}$$

and last

$$\frac{\partial p_0}{\partial q_1} = \frac{1}{\partial q_1/\partial p_0}. \tag{11.1.18}$$

By using Eqs. (11.1.15), (11.1.16), (11.1.17), and (11.1.18) the determinant Filinov pre-exponential factor becomes

$$det\left(\mathbf{c}_f^2\left(q_0,q_1\right)\right) = \left(1-\gamma c_0\right)\left(1-\gamma c_1\right) + ic_1\left(1-\gamma c_0\right)\frac{\partial q_1/\partial q_0}{\partial q_1/\partial p_0} + ic_0\left(1-\gamma c_1\right)\frac{\partial p_1/\partial p_0}{\partial q_1/\partial p_0} +$$

$$+ c_0c_1\left(\frac{\partial p_1/\partial p_0}{\partial q_1/\partial p_0}\frac{\partial q_1/\partial q_0}{\partial q_1/\partial p_0} + \frac{1}{\partial q_1/\partial p_0}\frac{1}{\partial q_1/\partial p_0}\right). \tag{11.1.19}$$

We now simplify the notation by writing

$$\left(\frac{|M_{qp}|}{2\pi i\hbar}\right)^{\frac{1}{2}}\left(det\left(\mathbf{c}_f^2\right)\right)^{\frac{1}{2}} = \frac{1}{2\pi\hbar}\left(-2\pi i\hbar\left|M_{qp}\right| det\left(\mathbf{c}_f^2\right)\right)^{\frac{1}{2}} \tag{11.1.20}$$

and calling *Filinov-Van-Vleck* pre-exponential factor $c_{fv} = \left(-2\pi i\hbar\left|M_{qp}\right| det\left(\mathbf{c}_f^2\right)\right)^{\frac{1}{2}}$. The square of c_{fv} is equal to

$$c_{fv}^2 = 2\hbar\gamma\left[-\left(1-\gamma c_0\right)\left(1-\gamma c_1\right)\frac{\partial q_1}{\partial p_0} + c_1\left(1-\gamma c_0\right)\frac{\partial q_1}{\partial q_0} + ic_0\left(1-\gamma c_1\right)\frac{\partial p_1}{\partial p_0} + ic_0c_1\frac{\partial p_1}{\partial q_0}\right]. \tag{11.1.21}$$

We now decide to choose $c_0 = c_1 = \frac{1}{2\hbar\gamma}$, and after some algebraic passages the previous equation becomes equal to

$$c_{fv}^2 = \frac{1}{2}\left[\frac{\partial q_1}{\partial q_0} + \frac{\partial p_1}{\partial p_0} - i\gamma\frac{\partial q_1}{\partial p_0} + \frac{i}{\gamma}\frac{\partial p_1}{\partial q_0}\right], \tag{11.1.22}$$

that is equal to the square of the Herman-Kluk pre-exponential factor, thus

$$c_{fv} = C_{HK}. \tag{11.1.23}$$

At this stage we have obtained that

$$\left\langle \psi_f \middle| e^{-\frac{i}{\hbar}\widehat{H}t} \middle| \psi_i \right\rangle = \iint dq_0 dp_0 C_{HK}\left(q_0, p_0\right) e^{-\boldsymbol{\phi'}(q_0,p_0)\frac{\mathbf{C}}{2}\boldsymbol{\phi'}(q_0,p_0)^T + i\phi(q_0,p_0)}, \tag{11.1.24}$$

with $\phi\left(q_0, p_0\right) = S_t\left(q_0, p_0\right) + p_i\left(q_0 - q_i\right) - p_f\left(q_1 - q_f\right) + \frac{i\hbar\gamma}{2}\left[\left(q_0 - q_i\right)^2 + \left(q_1 - q_f\right)^2\right]$.

We now focus on the exponential part of the integrand, starting from $-\boldsymbol{\phi'}\left(q_0, p_0\right)\frac{\mathbf{C}}{2}\boldsymbol{\phi'}\left(q_0, p_0\right)^T$. By solving the matrix product, the expression comes to be

$$-\boldsymbol{\phi'}\left(q_0, p_0\right)\frac{\mathbf{C}}{2}\boldsymbol{\phi'}\left(q_0, p_0\right)^T = -\frac{c_0}{2}\left[\left(p_1 - p_f\right)^2 + 2i\hbar\gamma\left(q_1 - q_f\right)\left(p_1 - p_f\right) - \hbar^2\gamma^2\left(q_1 - q_f\right)^2\right] +$$

$$-\frac{c_1}{2}\left[\left(p_i - p_0\right)^2 + 2i\hbar\gamma\left(q_0 - q_i\right)\left(p_i - p_0\right) - \hbar^2\gamma^2\left(q_0 - q_i\right)^2\right], \tag{11.1.25}$$

and relying to previous choice of c_0 and c_1 it becomes

$$-\boldsymbol{\phi'}\left(q_0, p_0\right)\frac{\mathbf{C}}{2}\boldsymbol{\phi'}\left(q_0, p_0\right)^T = -\frac{1}{4\hbar\gamma}\left[\left(p_1 - p_f\right)^2 + 2i\hbar\gamma\left(q_1 - q_f\right)\left(p_1 - p_f\right) - \hbar^2\gamma^2\left(q_1 - q_f\right)^2\right] +$$

$$-\frac{1}{4\hbar\gamma}\left[\left(p_i - p_0\right)^2 + 2i\hbar\gamma\left(q_0 - q_i\right)\left(p_i - p_0\right) - \hbar^2\gamma^2\left(q_0 - q_i\right)^2\right]. \tag{11.1.26}$$

Now, introducing Eq. (11.1.26) into the exponential part of Eq. (11.1.24), and after some simplifications, the exponential term becomes

$$-\boldsymbol{\phi'}\left(q_0, p_0\right)\frac{\mathbf{C}}{2}\boldsymbol{\phi'}\left(q_0, p_0\right)^T + i\phi\left(q_0, p_0\right) = \left\langle q_f p_f \middle| q_1 p_1 \right\rangle \left\langle q_0 p_0 \middle| q_i p_i \right\rangle. \tag{11.1.27}$$

The final expression of the quantum probability is

$$\left\langle \psi_f \middle| e^{-\frac{i}{\hbar}\widehat{H}t} \middle| \psi_i \right\rangle = \iint dq_0 dp_0 C_{HK}\left(q_0, p_0\right) \left\langle q_f p_f \middle| q_1 p_1 \right\rangle \left\langle q_0 p_0 \middle| q_i p_i \right\rangle, \tag{11.1.28}$$

that we recognize to be the Herman-Kluk expression of the quantum amplitude.

11.2 Time Averaged Semiclassical spectral density

To derive Eq. (4.2.1) we start by showing the truthfulness of the following identity

$$I = I_{TA}, \tag{11.2.1}$$

Where

$$I = \iint d\mathbf{p}_0 d\mathbf{q}_0 A\left(\mathbf{p}_0, \mathbf{q}_0\right)$$

and

$$I_{TA} = \frac{1}{T}\int_0^T dt \iint d\mathbf{p}_t d\mathbf{q}_t A\left(\mathbf{p}_t, \mathbf{q}_t\right).$$

I_{TA} is the Time-Averaged version of the integral I, where the integrand is considered to be a generic function of $(\mathbf{p}_0, \mathbf{q}_0)$. If the system fulfills Hamilton equations, by virtue of Liouville theorem the determinant of Jacobian of the transformation $(\mathbf{p}_0, \mathbf{q}_0) \leftarrow (\mathbf{p}_t, \mathbf{q}_t)$ is equal to one, resulting in

$$\iint d\mathbf{p}_0 d\mathbf{q}_0 A\left(\mathbf{p}_0, \mathbf{q}_0\right) = \iint d\mathbf{p}_t d\mathbf{q}_t A\left(\mathbf{p}_t, \mathbf{q}_t\right), \tag{11.2.2}$$

and

$$I_{TA} = \frac{1}{T}\int_0^T dt \iint d\mathbf{p}_0 d\mathbf{q}_0 A\left(\mathbf{p}_0, \mathbf{q}_0\right) =$$

$$\iint d\mathbf{p}_0 d\mathbf{q}_0 A\left(\mathbf{p}_0, \mathbf{q}_0\right) \frac{1}{T}\int_0^T dt = \iint d\mathbf{p}_0 d\mathbf{q}_0 A\left(\mathbf{p}_0, \mathbf{q}_0\right) = I. \tag{11.2.3}$$

By taking advantage of Eq. (11.2.3), Eq. (4.2.1) can be re-written as

$$I\left(E\right) = \left(\frac{1}{2\pi\hbar}\right)^F \iint d\mathbf{p}_0 d\mathbf{q}_0 \frac{1}{T}\int_0^T dt_1 \frac{Re}{\pi\hbar}\int_0^{+\infty} dt C_{t_1+t}\left(\mathbf{p}_{t_1}, \mathbf{q}_{t_1}\right) e^{\frac{i}{\hbar}S_{t_1+t}\left(\mathbf{p}_{t_1}, \mathbf{q}_{t_1}\right)}$$

$$\times \left\langle \chi \left| \mathbf{p}_{t_1+t}\mathbf{q}_{t_1+t} \right\rangle \left\langle \mathbf{p}_{t_1}\mathbf{q}_{t_1} \right| \chi \right\rangle e^{\frac{i}{\hbar}Et}, \tag{11.2.4}$$

where we remind that $\mathbf{p}_{t_{1+t}} = \mathbf{p}_{t_{1+t}}\left(\mathbf{p}_0, \mathbf{q}_0\right)$ and $\mathbf{q}_{t_{1+t}} = \mathbf{q}_{t_{1+t}}\left(\mathbf{p}_0, \mathbf{q}_0\right)$. The action term $S_{t_1+t}\left(\mathbf{p}_{t_1}, \mathbf{q}_{t_1}\right)$ describes the action of the path starting from $\left(\mathbf{p}_{t_1}, \mathbf{q}_{t_1}\right)$ and going

to $(\mathbf{p}_{t_1+t}, \mathbf{q}_{t_1+t})$ and it is equivalent to the action $S_{t_1+t}(\mathbf{p}_0, \mathbf{q}_0)$ starting from $(\mathbf{p}_0, \mathbf{q}_0)$ and going to $(\mathbf{p}_{t_1+t}, \mathbf{q}_{t_1+t})$ minus the action $S_t(\mathbf{p}_0, \mathbf{q}_0)$ of the same path but starting from $(\mathbf{p}_0, \mathbf{q}_0)$ and going to $(\mathbf{p}_t, \mathbf{q}_t)$. If we now call

$$t_2 = t_1 + t, \tag{11.2.5}$$

the action $S_{t_1+t}(\mathbf{p}_{t_1}, \mathbf{q}_{t_1}) = S_{t_2}(\mathbf{p}_{t_1}, \mathbf{q}_{t_1})$ is equal to

$$S_{t_2}(\mathbf{p}_{t_1}, \mathbf{q}_{t_1}) = S_{t_2}(\mathbf{p}_0, \mathbf{q}_0) - S_{t_1}(\mathbf{p}_0, \mathbf{q}_0). \tag{11.2.6}$$

Because of the change of variable in Eq. (11.2.5), the coherent states overlap becomes

$$\langle \chi \left| \mathbf{p}_{t_1+t} \mathbf{q}_{t_1+t} \right\rangle \langle \mathbf{p}_{t_1} \mathbf{q}_{t_1} | \chi \rangle = \langle \chi \left| \mathbf{p}_{t_2} \mathbf{q}_{t_2} \right\rangle \langle \mathbf{p}_{t_1} \mathbf{q}_{t_1} | \chi \rangle, \tag{11.2.7}$$

the pre-exponential factor

$$C_{t_1+t}(\mathbf{p}_{t_1}, \mathbf{q}_{t_1}) = C_{t_2}(\mathbf{p}_{t_1}, \mathbf{q}_{t_1}), \tag{11.2.8}$$

and the integration variables

$$\frac{1}{T}\int_0^T dt_1 \frac{Re}{\pi\hbar}\int_0^{+\infty} dt = \frac{1}{T}\int_0^T dt_1 \frac{Re}{\pi\hbar}\int_{t_1}^{+\infty} dt_2. \tag{11.2.9}$$

As an overall result, the spectral density will be calculated by evaluating two time integrals in t_1 and t_2

$$I(E) = \left(\frac{1}{2\pi\hbar}\right)^F \iint d\mathbf{p}_0 d\mathbf{q}_0 \frac{Re}{\pi\hbar}\frac{1}{T}\int_0^T dt_1 e^{-\frac{i}{\hbar}S_{t_1}(\mathbf{p}_0,\mathbf{q}_0)} e^{-\frac{i}{\hbar}Et_1} \left\langle \mathbf{p}_{t_1}\mathbf{q}_{t_1} \middle| \chi \right\rangle \times$$

$$\int_{t_1}^{+\infty} dt_2 C_{t_2}(\mathbf{p}_{t_1}, \mathbf{q}_{t_1}) e^{\frac{i}{\hbar}S_{t_2}(\mathbf{p}_0,\mathbf{q}_0)} \left\langle \chi \middle| \mathbf{p}_{t_2}\mathbf{q}_{t_2} \right\rangle e^{\frac{i}{\hbar}Et_2}. \tag{11.2.10}$$

Eq. (11.2.10) is still far apart from Eq. (4.2.1), since it presents two time integrals, which perhaps make it more complicated even than the original Herman Kluk version of the spectral density reported in Eq. (4.1.3). However, we note that the only component of the integrand depending from both t_2 and t_1 is the pre-exponential factor. It prevents the possibility to separate the two integrals. Kaledin and Miller suggested to employ the so-called separable approximation to address this issue, *i.e.* to consider the pre-exponential as a complex number of unitary modulos. Within this approximation

$$C_{t_2}\left(\mathbf{p}_{t_1}, \mathbf{q}_{t_1}\right) \sim e^{\frac{i}{\hbar}\varphi_{t_2}} e^{-\frac{i}{\hbar}\varphi_{t_1}}, \tag{11.2.11}$$

and now the integrand looks like much more friendly, since the two integral are separable

$$I\left(E\right) = \left(\frac{1}{2\pi\hbar}\right)^F \iint d\mathbf{p}_0 d\mathbf{q}_0 \frac{Re}{\pi\hbar} \frac{1}{T} \int_0^T dt_1 e^{-\frac{i}{\hbar}\left[S_{t_1}(\mathbf{p}_0,\mathbf{q}_0)+Et_1-\varphi_{t_1}\right]} \left\langle \mathbf{p}_{t_1}\mathbf{q}_{t_1} \middle| \chi \right\rangle \times$$

$$\int_{t_1}^{+\infty} dt_2 e^{\frac{i}{\hbar}\left[S_{t_2}(\mathbf{p}_0,\mathbf{q}_0)+Et_2-\varphi_{t_1}\right]} \left\langle \chi \middle| \mathbf{p}_{t_2}\mathbf{q}_{t_2} \right\rangle. \tag{11.2.12}$$

With T large enough the integration to be performed follows an insightful symmetry relation

$$\frac{1}{T}\int_0^T dt_1 \int_{t_1}^T dt_2 = \frac{1}{2T}\int_0^T dt_1 \int_0^T dt_2,$$

which leads Eq. (11.2.12) to be

$$I\left(E\right) = \left(\frac{1}{2\pi\hbar}\right)^F \iint d\mathbf{p}_0 d\mathbf{q}_0 \frac{Re}{2\pi\hbar} \frac{1}{T} \int_0^T dt_1 e^{-\frac{i}{\hbar}\left[S_{t_1}(\mathbf{p}_0,\mathbf{q}_0)+Et_1-\varphi_{t_1}\right]} \left\langle \mathbf{p}_{t_1}\mathbf{q}_{t_1} \middle| \chi \right\rangle \times$$

$$\int_0^T dt_2 e^{\frac{i}{\hbar}\left[S_{t_2}(\mathbf{p}_0,\mathbf{q}_0)+Et_2-\varphi_{t_1}\right]} \left\langle \chi \middle| \mathbf{p}_{t_2}\mathbf{q}_{t_2} \right\rangle \tag{11.2.13}$$

If we call

$$\frac{1}{T}\int_0^T dt e^{-\frac{i}{\hbar}\left[S_t(\mathbf{p}_0,\mathbf{q}_0)+Et-\varphi_t\right]} \left\langle \mathbf{p}_t\mathbf{q}_t \middle| \chi \right\rangle = f_E\left(\mathbf{p}_0, \mathbf{q}_0\right),$$

then we note that

$$f_E\left(\mathbf{p}_0,\mathbf{q}_0\right)^* = \frac{1}{T}\int_0^T dt e^{\frac{i}{\hbar}\left[S_t\left(\mathbf{p}_0,\mathbf{q}_0\right)+Et-\varphi_t\right]}\left\langle \chi\middle|\mathbf{p}_t\mathbf{q}_t\right\rangle.$$

Thus the two time integrals of Eq. (11.2.13) are complex conjugated and the overall expression of the spectral density becomes

$$I\left(E\right) = \left(\frac{1}{2\pi\hbar}\right)^F\left(\frac{1}{2\pi\hbar T}\right)\iint d\mathbf{p}_0 d\mathbf{q}_0\left|f_E\left(\mathbf{p}_0,\mathbf{q}_0\right)\right|^2$$

$$= \left(\frac{1}{2\pi\hbar}\right)^F\left(\frac{1}{2\pi\hbar T}\right)\iint d\mathbf{p}_0 d\mathbf{q}_0\left|\frac{1}{T}\int_0^T dt e^{-\frac{i}{\hbar}\left[S_t\left(\mathbf{p}_0,\mathbf{q}_0\right)+Et-\varphi_t\right]}\left\langle \mathbf{p}_t\mathbf{q}_t\middle|\chi\right\rangle\right|^2. \quad (11.2.14)$$

The integrand leading to the spectral density is now definite positive. Consquently it requires a lower number of classical trajectories to converge the integral. This Time Averaged version of the semiclassical spectral density requires only to approximate the pre-exponential factor as a complex number of unitary modulos, namely to account only for its phase. Such an approximation becomes exact when harmonic potentials are considered, where the pre-exponential factor is effectively $C_t\left(\mathbf{p}_0,\mathbf{q}_0\right) = e^{\frac{i}{\hbar}\varphi_t}$.

11.3 Harmonic oscillator pre-exponential factor

For an harmonic oscillator described by a potential $V = \frac{1}{2}\omega^2\left(q-q_0\right)^2$, where q_0 is the equilibrium coordinate, the classical equations of motions (with unitary mass $m=1$) are

$$\begin{cases} q_t = q_0 cos\left(\omega t\right) + \frac{p_0}{\omega} sin\left(\omega t\right) \\ p_t = p_0 cos\left(\omega t\right) - \omega q_0 sin\left(\omega t\right) \end{cases} \quad (11.3.1)$$

The monodromy matrix element are then

$$\begin{cases} M_{qq} = cos\left(\omega t\right) \\ M_{qp} = \frac{1}{\omega} sin\left(\omega t\right) \\ M_{pq} = -\omega sin\left(\omega t\right) \\ M_{pp} = cos\left(\omega t\right). \end{cases}$$

By substituting into Eq. (3.2.3) we obtain (assuming $\hbar = 1$)

$$C_t = \sqrt{\frac{1}{2}\left(cos\left(\omega t\right) + cos\left(\omega t\right) - isin\left(\omega t\right) + \frac{1}{i} sin\left(\omega t\right)\right)} = e^{-\frac{1}{2}i\omega t}. \tag{11.3.2}$$

Alternatively, we can take advantage of the Log-derivative formulation of the pre-exponential factor. In this case the Riccati equation (5.3.2) is analytically solvable since we have to solve a first order differential equation of the type

$$\dot{R}_t = -\omega^2 - R_t, \tag{11.3.3}$$

where in this context the hessian becomes a constant $K_t = \omega^2$. The general solution is

$$R_t = -\omega tan\left(\omega c_1 + \omega t\right)$$

that can be written also as

$$R_t = -\omega \frac{tan\left(\omega c_1\right) + tan\left(\omega t\right)}{1 - tan\left(\omega c_1\right) tan\left(\omega t\right)}.$$

By substituting the initial condition $R_0 = -i\omega$ we obtain $c_1 = \frac{1}{\omega} \arctan\left[i\right]$ and

$$R_t = -\omega \frac{i + tan\left(\omega t\right)}{1 - itan\left(\omega t\right)} = -i\omega \tag{11.3.4}$$

The Riccati solution is a constant imaginary number that substituted into Eq. (5.3.1) leads to

$$C_t\left(p_0, q_0\right) = \sqrt{\left[\frac{1}{2}\left(1 + \frac{i}{\omega}R_t\right)\right]} e^{\frac{1}{2}\int_0^t d\tau R_\tau} = e^{-\frac{1}{2}\omega t}, \tag{11.3.5}$$

that is equivalent to Eq. (11.3.2).

Bibliography

[1] A. Rahman, Physical Review **136**, A405 (1964).

[2] L. Verlet, Phys. Rev. **159**, 98 (1967).

[3] F. Ancilotto, W. Andreoni, A. Selloni, R. Car, and M. Parrinello, Phys. Rev. Lett. **65**, 3148 (1990).

[4] A. Selloni, A. Vittadini, and M. Grätzel, Surface science **402**, 219 (1998).

[5] N. Marzari, D. Vanderbilt, and M. C. Payne, Physical review letters **79**, 1337 (1997).

[6] R. Elber and M. Karplus, Science **235**, 318 (1987).

[7] M. Karplus and J. A. McCammon, Nature Structural & Molecular Biology **9**, 646 (2002).

[8] T. I. Cheatham, J. Miller, T. Fox, T. Darden, and P. Kollman, J. Am. Chem. Soc. **117**, 4193 (1995).

[9] R. R. Johnson, A. C. Johnson, and M. L. Klein, Nano Lett. **8**, 69 (2008).

[10] J. A. Morrone and R. Car, Phys. Rev. Lett. **101**, 017801 (2008).

[11] H.-D. Meyer, U. Manthe, and L. S. Cederbaum, Chem. Phys. Lett. **165**, 73 (1990).

[12] V. Barone, J. Chem. Phys. **122**, 014108 (2005).

[13] D. T. Colbert and W. H. Miller, J. Chem. Phys. **96**, 1982 (1992).

[14] T. Halverson and B. Poirier, J. Phys. Chem. A **119**, 12417 (2015).

[15] R. P. Feynman and A. R. Hibbs, *Quantum mechanics and path integrals [by] RP Feynman [and] AR Hibbs* (McGraw-Hill, 1965).

[16] W. H. Miller, J. Phys. Chem. A **105**, 2942 (2001).

[17] E. J. Heller, J. Chem. Phys. **62**, 1544 (1975).

[18] E. J. Heller, Acc. Chem. Res. **14**, 368 (1981).

[19] W. H. Miller, Proc. Natl. Acad. Sci. USA **102**, 6660 (2005).

[20] S. Habershon, D. E. Manolopoulos, T. E. Markland, and T. F. Miller III, Annu. Rev. Phys. Chem. **64**, 387 (2013).

[21] O. Marsalek and T. E. Markland, J. Chem. Phys. **144**, 054112 (2016).

[22] M. Rossi, M. Ceriotti, and D. E. Manolopoulos, J. Chem. Phys. **140**, 234116 (2014).

[23] I. R. Craig and D. E. Manolopoulos, J. Chem. Phys. **121**, 3368 (2004).

[24] B. J. Braams and D. E. Manolopoulos, J. Chem. Phys. **125**, 124105 (2006).

[25] D. J. Tannor, *Introduction to quantum mechanics* (University Science Books, 2007).

[26] K. G. Kay, Annu. Rev. Phys. Chem. **56**, 255 (2005).

[27] K. G. Kay, J. Chem. Phys. **100**, 4377 (1994).

[28] K. G. Kay, J. Chem. Phys. **101**, 2250 (1994).

[29] K. G. Kay, J. Chem. Phys. **100**, 4432 (1994).

[30] E. Pollak, in *Quantum Dynamics of Complex Molecular Systems*, edited by D. A. Micha and I. Burghardt (Springer Berlin Heidelberg, Berlin, Heidelberg, 2007) pp. 259–271.

[31] J. Tatchen and E. Pollak, J. Chem. Phys. **130**, 041103 (2009).

[32] E. J. Heller, J. Chem. Phys. **94**, 2723 (1991).

[33] S. Bonella, D. Montemayor, and D. F. Coker, Proc. Natl. Ac. Sci. **102**, 6715 (2005).

[34] M. Wehrle, M. Sulc, and J. Vanicek, J. Chem. Phys. **140**, 244114 (2014).

[35] X. Sun and W. H. Miller, J. Chem. Phys. **110**, 6635 (1999).

[36] J. Shao and N. Makri, J. Phys. Chem. A **103**, 7753 (1999).

[37] S. V. Antipov, Z. Ye, and N. Ananth, J. Chem. Phys. **142**, 184102 (2015).

[38] M. S. Church, S. V. Antipov, and N. Ananth, J. Chem. Phys. **146**, 234104 (2017).

[39] A. Patoz, T. Begušić, and J. Vaníček, J. Phys. Chem. Lett. **9**, 2367 (2018).

[40] N. Ananth, C. Venkataraman, and W. H. Miller, J. Chem. Phys. **127**, 084114 (2007).

[41] M. K. Lee, P. Huo, and D. F. Coker, Annu. Rev. Phys. Chem. **67**, 639 (2016).

[42] S. Bonella and D. Coker, J. Chem. Phys. **114**, 7778 (2001).

[43] S. Bonella and D. F. Coker, J. Chem. Phys. **118**, 4370 (2003).

[44] P. Huo and D. F. Coker, Mol. Phys. **110**, 1035 (2012).

[45] C. Margulis, D. Horner, S. Bonella, and D. Coker, J. Phys. Chem. A **103**, 9552 (1999).

[46] J. H. Van Vleck, Proc. Natl. Acad. Sci. **14**, 178 (1928).

[47] W. H. Miller, J. Chem. Phys. **53**, 3578 (1970).

[48] W. H. Miller and T. F. George, J. Chem. Phys. **56**, 5637 (1972).

[49] E. J. Heller, J. Chem. Phys. **75**, 2923 (1981).

[50] N. De Leon and E. J. Heller, J. Chem. Phys. **78**, 4005 (1983).

[51] M. F. Herman and E. Kluk, Chem. Phys. **91**, 27 (1984).

[52] F. Grossmann and A. L. Xavier, Phys. Lett. A **243**, 243 (1998).

[53] W. H. Miller, Mol. Phys. **100**, 397 (2002).

[54] K. G. Kay, Chem. Phys. **322**, 3 (2006).

[55] H. Wang, D. E. Manolopoulos, and W. H. Miller, J. Chem. Phys. **115**, 6317 (2001).

[56] J. M. Bowman, A. Wierzbicki, and J. Zuniga, Chem. Phys. Lett. **150**, 269 (1988).

[57] B. J. Braams and J. M. Bowman, Int. Rev. Phys. Chem. **28**, 577 (2009).

[58] S. Carter, H. M. Shnider, and J. M. Bowman, J. Chem. Phys. **110**, 8417 (1999).

[59] R. Conte, C. Qu, and J. M. Bowman, J. Chem. Theory Comp. **11**, 1631 (2015).

[60] Y. Wang and J. M. Bowman, Chem. Phys. Lett. **491**, 1 (2010).

[61] B. Mennucci and J. Tomasi, J. Chem. Phys. **106**, 5151 (1997).

[62] J. Tomasi, B. Mennucci, and R. Cammi, Chem. Rev. **105**, 2999 (2005).

[63] B. Mennucci, Wiley Interdisciplinary Reviews: Computational Molecular Science **2**, 386 (2012).

[64] A. L. Kaledin and W. H. Miller, J. Chem. Phys. **118**, 7174 (2003).

[65] A. L. Kaledin and W. H. Miller, J. Chem. Phys. **119**, 3078 (2003).

[66] M. Ceotto, S. Valleau, G. F. Tantardini, and A. Aspuru-Guzik, J. Chem. Phys. **134**, 234103 (2011).

[67] M. Ceotto, S. Atahan, G. F. Tantardini, and A. Aspuru-Guzik, J. Chem. Phys. **130**, 234113 (2009).

[68] M. Ceotto, S. Atahan, S. Shim, G. F. Tantardini, and A. Aspuru-Guzik, Phys. Chem. Chem. Phys. **11**, 3861 (2009).

[69] C. Mak and D. Chandler, Phys. Rev. A **41**, 5709 (1990).

[70] B. J. Berne and D. Thirumalai, Annu. Rev. Phys. Chem. **37**, 401 (1986).

[71] M. Ceotto, G. Di Liberto, and R. Conte, Phys. Rev. Lett. **119**, 010401 (2017).

[72] G. Di Liberto and M. Ceotto, J. Chem. Phys. **145**, 144107 (2016).

[73] D. Tamascelli, F. S. Dambrosio, R. Conte, and M. Ceotto, J. Chem. Phys. **140**, 174109 (2014).

[74] B. B. Harland and P.-N. Roy, J. Chem. Phys. **118**, 4791 (2003).

[75] M. Ceotto, G. F. Tantardini, and A. Aspuru-Guzik, J. Chem. Phys. **135**, 214108 (2011).

[76] F. Gabas, R. Conte, and M. Ceotto, J. Chem. Theory Comput. **13**, 2378 (2017).

[77] M. Ceotto, Y. Zhuang, and W. L. Hase, J. Chem. Phys. **138**, 054116 (2013).

[78] R. Gelabert, X. Giménez, M. Thoss, H. Wang, and W. H. Miller, J. Phys. Chem. A **104**, 10321 (2000).

[79] J. Tatchen, E. Pollak, G. Tao, and W. H. Miller, J. Chem. Phys. **134**, 134104 (2011).

[80] V. Guallar, V. S. Batista, and W. H. Miller, J. Chem. Phys. **110**, 9922 (1999).

[81] V. Guallar, V. S. Batista, and W. H. Miller, J. Chem. Phys. **113**, 9510 (2000).

[82] D. E. Manolopoulos and S. K. Gray, J. Chem. Phys. **102**, 9214 (1995).

[83] M. L. Brewer, J. Chem. Phys. **111**, 6168 (1999).

[84] A. Chedin, J. Mol. Spectrosc. **76**, 430 (1979).

[85] J. VaÌzquez, M. E. Harding, J. F. Stanton, and J. Gauss, J. Chem. Theo. Comput. **7**, 1428 (2011).

[86] J. Martin, T. J. Lee, and P. Taylor, J. mol. spectr. **160**, 105 (1993).

[87] S. Carter, N. Pinnavaia, and N. C. Handy, Chem. phys. lett. **240**, 400 (1995).

[88] T. J. Lee, J. M. Martin, and P. R. Taylor, J. Chem Phys. **102**, 254 (1995).

[89] K. Hinsen and G. R. Kneller, Mol. Simul. **23**, 275 (2000).

[90] H. Partridge and D. W. Schwenke, J. Chem. Phys. **106**, 4618 (1997).

[91] Y. Wang and J. M. Bowman, J. Chem. Phys. **134**, 154510 (2011).

[92] Y. Wang, B. C. Shepler, B. J. Braams, and J. M. Bowman, J. Chem. Phys. **131**, 054511 (2009).

[93] Y. Wang, X. Huang, B. C. Shepler, B. J. Braams, and J. M. Bowman, J. Chem. Phys. **134**, 094509 (2011).

[94] Y. Wang and J. M. Bowman, J. Chem. Phys. **136**, 144113 (2012).

[95] Y. Wang, S. Carter, B. J. Braams, and J. M. Bowman, J. Chem. Phys. **128**, 071101 (2008).

[96] H. Partridge and D. W. Schwenke, J. Chem. Phys. **106**, 4618 (1997).

[97] N. C. Handy, P. E. Maslen, R. D. Amos, J. S. Andrews, C. W. Murray, and G. J. Laming, Chem. Phys. Lett. **197**, 506 (1992).

[98] D. Holec, M. A. Hartmann, F. D. Fischer, F. G. Rammerstorfer, P. H. Mayrhofer, and O. Paris, Phys. Rev. B **81**, 235403 (2010).

[99] Y. Wang and J. M. Bowman, Phys. Chem. Chem. Phys. **18**, 24057 (2016).

[100] Y. Wang and J. M. Bowman, J. Phys. Chem. Lett. **4**, 1104 (2013).

[101] X. Huang, B. J. Braams, J. M. Bowman, R. E. Kelly, J. Tennyson, G. C. Groenenboom, and A. van der Avoird, J. Chem. Phys. **128**, 034312 (2008).

[102] X. Huang, B. J. Braams, and J. M. Bowman, J. Chem. Phys. **122**, 044308 (2005).

[103] O. Vendrell, F. Gatti, and H.-D. Meyer, J. Chem. Phys. **127**, 184303 (2007).

[104] O. Vendrell and H.-D. Meyer, Phys. Chem. Chem. Phys. **10**, 4692 (2008).

[105] O. Vendrell, F. Gatti, D. Lauvergnat, and H.-D. Meyer, J. Chem. Phys. **127**, 184302 (2007).

[106] O. Vendrell, F. Gatti, and H.-D. Meyer, Angew. Chem. **46**, 6918 (2007).

[107] O. Vendrell, M. Brill, F. Gatti, D. Lauvergnat, and H.-D. Meyer, J. Chem. Phys. **130**, 234305 (2009).

[108] O. Vendrell, F. Gatti, and H.-D. Meyer, J. Chem. Phys. **131**, 034308 (2009).

[109] O. Vendrell, F. Gatti, and H.-D. Meyer, Angew. Chem. **48**, 352 (2009).

[110] A. B. McCoy, X. Huang, S. Carter, M. Y. Landeweer, and J. M. Bowman, J. Chem. Phys. **122**, 061101 (2005).

[111] N. I. Hammer, E. G. Diken, J. R. Roscioli, M. A. Johnson, E. M. Myshakin, K. D. Jordan, A. B. McCoy, X. Huang, J. M. Bowman, and S. Carter, J. Chem. Phys. **122**, 244301 (2005).

[112] Y. Wu and G. A. Voth, Biophys. J. **85**, 864 (2003).

[113] O. F. Mohammed, D. Pines, J. Dreyer, E. Pines, and E. T. Nibbering, Science **310**, 83 (2005).

[114] D. Riccardi, P. Koenig, X. Prat-Resina, H. Yu, M. Elstner, T. Frauenheim, and Q. Cui, J. Am. Chem. Soc. **128**, 16302 (2006).

[115] C. T. Wolke, J. A. Fournier, L. C. Dzugan, M. R. Fagiani, T. T. Odbadrakh, H. Knorke, K. D. Jordan, A. B. McCoy, K. R. Asmis, and M. A. Johnson, Science **354**, 1131 (2016).

[116] A. M. Smondyrev and G. A. Voth, Biophys. J. **82**, 1460 (2002).

[117] M. K. Petersen, F. Wang, N. P. Blake, H. Metiu, and G. A. Voth, J. Phys. Chem. B **109**, 3727 (2005).

[118] D. Marx, ChemPhysChem **7**, 1848 (2006).

[119] M. W. Feyereisen, D. Feller, and D. A. Dixon, J. Phys. Chem. **100**, 2993 (1996).

[120] P. H. Poole, F. Sciortino, T. Grande, H. E. Stanley, and C. A. Angell, Phys. Rev. Lett. **73**, 1632 (1994).

[121] K. Liu, M. Brown, C. Carter, R. Saykally, *et al.*, Nature **381**, 501 (1996).

[122] S. S. Xantheas, Chem. Phys. **258**, 225 (2000).

[123] K. Liu, J. Cruzan, and R. Saykally, Science **271**, 929 (1996).

[124] K. Pfeilsticker, A. Lotter, C. Peters, and H. Bösch, Science **300**, 2078 (2003).

[125] E. Vöhringer-Martinez, B. Hansmann, H. Hernandez, J. Francisco, J. Troe, and B. Abel, Science **315**, 497 (2007).

[126] C. Qu, R. Conte, P. L. Houston, and J. M. Bowman, Phys. Chem. Chem. Phys. **17**, 8172 (2015).

[127] J. S. Mancini and J. M. Bowman, J. Chem. Phys. **138**, 121102 (2013).

[128] J. S. Mancini and J. M. Bowman, J. Phys. Chem. Lett. **5**, 2247 (2014).

[129] A. K. Samanta, Y. Wang, J. S. Mancini, J. M. Bowman, and H. Reisler, Chem. Rev. **116**, 4913 (2016).

[130] E. Kamarchik, D. Toffoli, O. Christiansen, and J. M. Bowman, Spectrochimica Acta Part A: Molecular and Biomolecular Spectroscopy **119**, 59 (2014).

[131] E. Kamarchik, Y. Wang, and J. M. Bowman, J. Chem. Phys. **134**, 114311 (2011).

[132] E. Kamarchik and J. M. Bowman, J. Phys. Chem. A **114**, 12945 (2010).

[133] Y. Wang, J. M. Bowman, and E. Kamarchik, J. Chem. Phys. **144**, 114311 (2016).

[134] X. Huang, S. Habershon, and J. M. Bowman, Chem. Phys. Lett. **450**, 253 (2008).

[135] M. Kaledin, A. L. Kaledin, J. M. Bowman, J. Ding, and K. D. Jordan, J. Phys. Chem. A **113**, 7671 (2009).

[136] M. Baer, D. Marx, and G. Mathias, Angew. Chem. **49**, 7346 (2010).

[137] F. Agostini, R. Vuilleumier, and G. Ciccotti, J. Chem. Phys. **134**, 084302 (2011).

[138] M. Tuckerman, K. Laasonen, M. Sprik, and M. Parrinello, J. Chem. Phys. **103**, 150 (1995).

[139] J. M. Headrick, J. C. Bopp, and M. A. Johnson, J. Chem. Phys. **121**, 11523 (2004).

[140] T. D. Fridgen, T. B. McMahon, L. MacAleese, J. Lemaire, and P. Maitre, J. Phys. Chem. A **108**, 9008 (2004).

[141] M. Miyazaki, A. Fujii, T. Ebata, and N. Mikami, Science **304**, 1134 (2004).

[142] N. Singh, M. Park, S. K. Min, S. B. Suh, and K. S. Kim, Angew. Chem. **118**, 3879 (2006).

[143] G. Douberly, R. Walters, J. Cui, K. D. Jordan, and M. Duncan, J. Phys. Chem. A **114**, 4570 (2010).

[144] J. Paul, R. Provencal, C. Chapo, K. Roth, R. Casaes, and R. Saykally, J. Phys. Chem. A **103**, 2972 (1999).

[145] Y. Bouteiller and J. Perchard, Chem. Phys. **305**, 1 (2004).

[146] R. Schwan, M. Kaufmann, D. Leicht, G. Schwaab, and M. Havenith, Phys. Chem. Chem. Phys. **18**, 24063 (2016).

[147] S. Hirabayashi and K. M. Yamada, J. Chem. Phys. **122**, 244501 (2005).

[148] J. Paul, C. Collier, R. Saykally, J. Scherer, and A. O'keefe, J. Phys. Chem. A **101**, 5211 (1997).

[149] U. Buck, I. Ettischer, M. Melzer, V. Buch, and J. Sadlej, Phys. Rev. Lett. **80**, 2578 (1998).

[150] P. Lakshminarayanan, E. Suresh, and P. Ghosh, J. Am. Chem. Soc. **127**, 13132 (2005).

[151] F. Huisken, M. Kaloudis, and A. Kulcke, J. Chem. Phys. **104**, 17 (1996).

[152] C. Steinbach, P. Andersson, M. Melzer, J. Kazimirski, U. Buck, and V. Buch, Phy. Chem. Chem. Phys. **6**, 3320 (2004).

[153] Z. Huang and R. Miller, J. Chem. Phys. **91**, 6613 (1989).

[154] U. Buck and F. Huisken, Chem. Rev. **100**, 3863 (2000).

[155] M. N. Slipchenko, K. E. Kuyanov, B. G. Sartakov, and A. F. Vilesov, J. Chem. Phys. **124**, 241101 (2006).

[156] J. Paul, R. Provencal, C. Chapo, A. Petterson, and R. Saykally, J. Chem. Phys. **109**, 10201 (1998).

[157] S. S. Xantheas and T. H. Dunning Jr, J. Chem. Phys. **99**, 8774 (1993).

[158] S. Yoo, E. Apra, X. C. Zeng, and S. S. Xantheas, J. Phys. Chem. Lett. **1**, 3122 (2010).

[159] S. Bulusu, S. Yoo, E. Apra, S. Xantheas, and X. C. Zeng, J. Phys. Chem. A **110**, 11781 (2006).

[160] S. S. Xantheas and T. H. Dunning Jr, J. Chem. Phys. **98**, 8037 (1993).

[161] S. Maheshwary, N. Patel, N. Sathyamurthy, A. D. Kulkarni, and S. R. Gadre, J. Phys. Chem. A **105**, 10525 (2001).

[162] D. J. Wales and M. P. Hodges, Chem. Phys. Lett. **286**, 65 (1998).

[163] S. S. Xantheas, C. J. Burnham, and R. J. Harrison, J. Chem. Phys. **116**, 1493 (2002).

[164] S. S. Xantheas, J. Chem. Phys. **102**, 4505 (1995).

[165] Y. Wang, V. Babin, J. M. Bowman, and F. Paesani, J. Am. Chem. Soc. **134**, 11116 (2012).

[166] J. M. Bowman, B. Braams, S. Carter, C. Chen, G. Czakó, B. Fu, X. Huang, E. Kamarchik, A. Sharma, B. Shepler, *et al.*, J. Phys. Chem. Lett. **1**, 1866 (2010).

[167] V. Babin and F. Paesani, Chem. Phys. Lett. **580**, 1 (2013).

[168] H. Liu, Y. Wang, and J. M. Bowman, J. Phys. Chem. Lett. **3**, 3671 (2012).

[169] H. Liu, Y. Wang, and J. M. Bowman, J. Chem. Phys. **142**, 194502 (2015).

[170] J. O. Richardson, C. Pérez, S. Lobsiger, A. A. Reid, B. Temelso, G. C. Shields, Z. Kisiel, D. J. Wales, B. H. Pate, and S. C. Althorpe, Science **351**, 1310 (2016).

[171] G. R. Medders and F. Paesani, J. Chem. Theo. Comp. **9**, 4844 (2013).

[172] L. C. Ch'ng, A. K. Samanta, G. Czakó, J. M. Bowman, and H. Reisler, J. Am. Chem. Soc. **134**, 15430 (2012).

[173] C. J. Burnham, J. Li, S. S. Xantheas, and M. Leslie, J. Chem. Phys. **110**, 4566 (1999).

[174] A. Shank, Y. Wang, A. Kaledin, B. J. Braams, and J. M. Bowman, J. Chem. Phys. **130**, 144314 (2009).

[175] C. J. Burnham and S. S. Xantheas, J. Chem. Phys. **116**, 1500 (2002).

[176] C. J. Burnham and S. S. Xantheas, J. Chem. Phys. **116**, 5115 (2002).

[177] G. S. Fanourgakis and S. S. Xantheas, J. Phys. Chem. A **110**, 4100 (2006).

[178] G. S. Fanourgakis and S. S. Xantheas, J. Chem. Phys. **128**, 074506 (2008).

[179] S. S. Xantheas, J. Chem. Phys. **100**, 7523 (1994).

[180] J. K. Gregory and D. C. Clary, J. Chem. Phys. **103**, 8924 (1995).

[181] G. Di Liberto, R. Conte, and M. Ceotto, J. Chem. Phys. **148**, 014307 (2018).

[182] H.-B. Oh, C. Lin, H. Y. Hwang, H. Zhai, K. Breuker, V. Zabrouskov, B. K. Carpenter, and F. W. McLafferty, J. Am. Chem. Soc. **127**, 4076 (2005).

[183] R. Wu and T. B. McMahon, J. Am. Chem. Soc. **129**, 4864 (2007).

[184] M. Valiev, E. Bylaska, N. Govind, K. Kowalski, T. Straatsma, H. V. Dam, D. Wang, J. Nieplocha, E. Apra, T. Windus, and W. de Jong, Comput. Phys. Commun. **181**, 1477 (2010).

[185] A. D. Becke, J. Chem. Phys. **98**, 5648 (1993).

[186] F. Gabas, G. Di Liberto, R. Conte, and M. Ceotto, Chem. Sci. (2018).

[187] N. Makri and W. H. Miller, Chem. Phys. Lett. **139**, 10 (1987).

[188] V. Filinov, Nuclear Physics B **271**, 717 (1986).

Chapter 12

Acknowledgments

And now the most complicated section to me, I think I'm not enough able to properly say thank you to the people that helped me along this trip, but I'll try even if probably each statement should require a superlative to give an idea of my gratitude.

First of all I would like to acknowledge my supervisor Michele Ceotto and this is the third time! Thanks for the help along the last six years. Then many thanks also to Dr. Leonardo Lo Presti and Prof. Luigi Falciola for many suggestions and very useful discussions. I owe also a lot with all the past and present members of Michele's research group for all the good time spent together. Thanks to Agnes, Huaquin, Chiara, Fabio, Marco Micciarelli, Marco Cazzaniga, Jaime and Max. A special mention goes to Gianluca Bertaina and Riccardo Conte for all of their scientific and personal suggestions, and for sharing with me so much of their knowledge and experience. I really and strongly feel in debt with them. But these years would not have been the same without my friends! Life is starting to go through different directions for everyone, but love keeps us even more in touch. This university has given me the opportunity to meet three amazing people Arianna, Giovanni and Francesco.

Along these three years my life is utterly changed and the doctoral path did not coincide only to my scientific growth, but mainly to my personal maturation. I started the PhD as a guy and now I trying to build up my own family. All of this is due to Valentina, the love of my life. She would deserve at least an entire book of acknowledgments and I'm

really not able to fully describe and show her my gratitude for making everyday amazing, and for all the support she gave me along these years, in the good but mainly in the bad moments. I also owe a lot to my parents who have first supported and encouraged me since I was a little child, and to all of my family including Valentina's one who have embraced me as a son.

Finally, despite my undisputed inability to share my feeling I hope to return them all the good that I received, and once again I just want to say *Thank you all*.